DESIGN OF AIRPORT SURFACE MOVEMENT

USING SINGLE-FREQUENCY GPS

A DISSERTATION

SUBMITTED TO THE DEPARTMENT OF AERONAUTICS AND ASTRONAUTICS

AND THE COMMITTEE ON GRADUATE STUDIES

OF STANFORD UNIVERSITY

IN PARTIAL FULFILLMENT OF THE REQUIREMENTS

FOR THE DEGREE OF

DOCTOR OF PHILOSOPHY

Young Shin Park
August 2016

# ABSTRACT

Ground Based Augmentation Systems (GBAS), such as the U.S. Local Area Augmentation System (LAAS), augment satellite navigation systems by providing differential corrections and integrity information to aviation users within several tens of kilometers of GBAS-equipped airports. GBAS can be used for both precision approach and Differentially Corrected Positioning Service (DCPS) applications. DCPS is broadly composed of (but is not limited to) three operations. The first operation is terminal-area navigation for aircraft in the area from the precision approach region to 45 kilometers away from the GBAS Ground Facility. The second operation is en route navigation for aircraft passing over the airport that can receive and make use of the GBAS VHS Data Broadcast receiver (VDB). The third operation is airport surface movement for aircraft on airport taxiways (and thus quite close to the GBAS Ground Facility centroid). This last operation is the subject of this research.

One of the residual errors that can build up for the user of a differential GPS system like GBAS is ionospheric spatial decorrelation error. This error is caused by the fact that two GPS signals are passing through different regions of the atmosphere, and the resulting ionospheric delays cannot be completely canceled out even after applying differential corrections. Under severe ionospheric storm conditions, these errors can grow large enough

to pose a threat to user integrity. In addition, since an aircraft undergoing airport surface movement is on the ground, it suffers from higher multipath errors than while in flight, as additional signal reflections come from the ground, other aircraft or vehicles, and nearby buildings.

In order to cover higher multipath errors in the surface movement and represent anomalous ionospheric errors, Jahn's Multipath Model for Urban and Suburban Environments [Jahn, 1996] and the CAT-I Conterminous United States (CONUS) Anomalous Ionospheric Threat Model [Pullen, 2009], respectively, are used for horizontal position errors. Because, for certain scenarios, GBAS Ground Facility geometry screening and new values of multipath errors for the suburban-optimistic environment are not sufficient by themselves, the proposed additional airborne geometry screening is performed to meet the requirements and lower the acceptable error to a beneficial level while maintaining useful availability.

The results show the sensitivity of availability to the multipath model and the ionospheric threat impact model for several Maximum Acceptable Error (MAE) levels. The multipath models considered are no multipath, suburban-conservative, urban-optimistic, and urban-conservative multipath models. The 0-satellite (no ionosphere), 1-satellite, and 2-satellites impact models of ionospheric threat are studied. In conclusion, the proposed approach to GBAS airport surface movement is feasible for surveillance applications, which are used to detect and display the position of aircraft in the terminal area, with an error bound of 20 meters. Guidance applications, which are used to guide aircraft from runway to the gate or vice versa, with an error bound of 10 meters are also feasible if multipath models less extreme than urban-conservative are used.

# ACKNOWLEDGMENTS

Professor Per Enge has been the world's best advisor to me. I would like to thank him for providing the best environment for the research. He guided me in the right direction throughout my Ph.D. course while still allowing me the freedom to explore. He made sure that I saw the forest of the research, rather than just the trees. He has been supportive, kind, and patient in turning a first-year Ph.D. candidate into an actual Ph.D. I learned many nice things from him.

I would also like to thank Professor J. David Powell for being a member of my Reading Committee of this dissertation. His review was very helpful and he encouraged me with warm words and beautiful vision. I also extend my gratitude to the other members of my Ph.D. Oral Exam Committee, Professor Stephen Rock and Professor Donald Cox, for their insightful commentary.

I would like to thank Dr. Sam Pullen for mentoring me during my Ph.D. research. He is a true intellectual and shared his knowledge with me. He has always been there when I needed his help. He is kind, caring, and understanding. He is very special to me and my work and I think no mentors like him exist in the world.

and the Life to me. He has been my shepherd through the journey of my Ph.D. Thank you, my Lord.

# TABLE OF CONTENTS

# LIST OF TABLES

# LIST OF FIGURES

# Chapter 1

# INTRODUCTION

In January 2013, London's Heathrow Airport canceled 260 flights (or 20 percent of its usual schedule) because of snow and low visibility. Fox News reported that there were more than three days of flight disruptions at Heathrow, one of Europe's busiest airports, which saw long lines and stranded passengers camped out on its terminal floors as shown in Figure 1.1. Fox also reported similar but more severe scenes back in December 2010, when the airport was virtually shut down by snow for several days [AP, 2013][BBC, 2013][Griffiths, 2013].

Why do significant flight disruptions at an airport occur in low visibility such as foggy or snowy weather? It is because airplane operations at the airport rely on good visibility. An airplane needs to be self-located with the help of a system that reports its location to the pilot. The support system includes the airport traffic control tower, signs, lights, and markings, which are all dependent on visibility. The control tower manages traffic at the airport by directing aircraft on the ground and through controlled airspace. The controllers should be able to see all the airplanes taxiing on the ground, landing, and taking off. The pilot taxis and avoids other traffic visually. Therefore, in weather with low visibility as

shown in Figure 1.1 and Figure 1.2, flights can be canceled, diverted, or delayed, resulting in inconvenience for airport users.
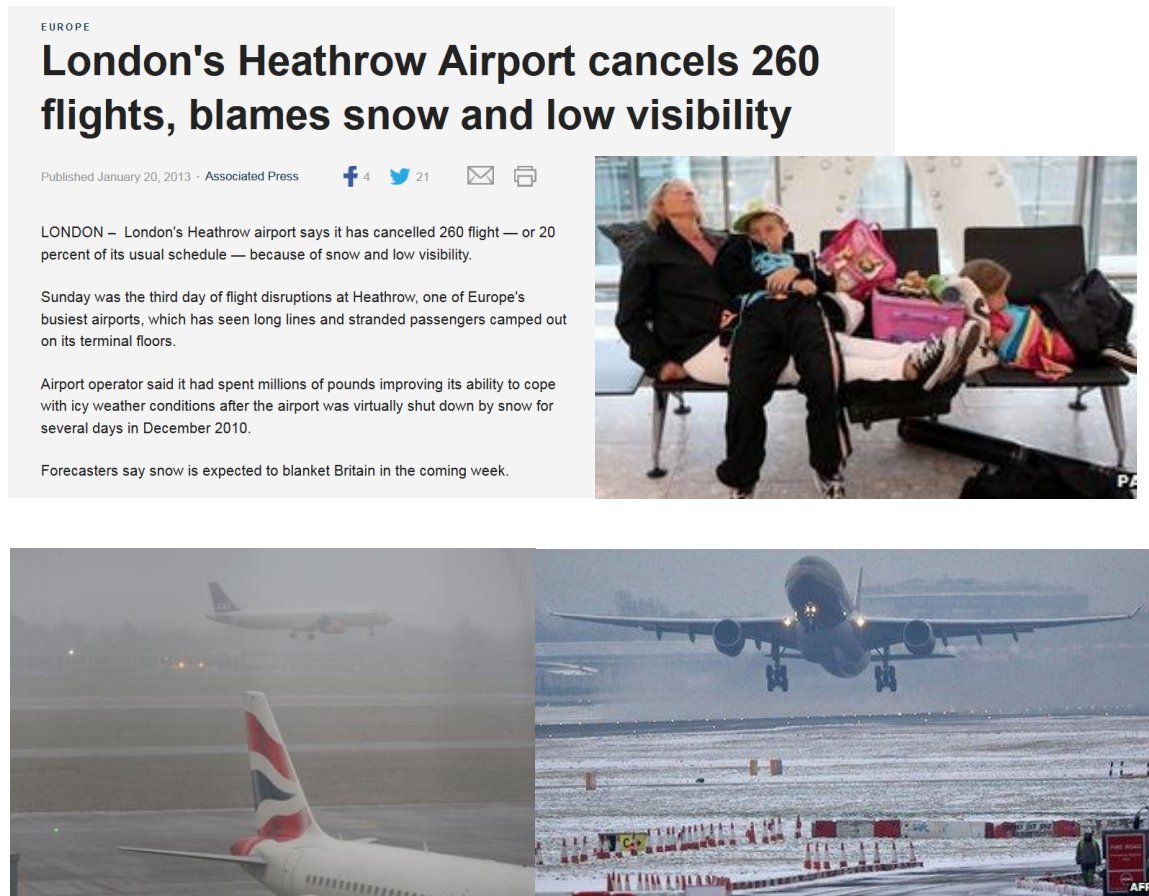


Figure 1.1. News about flight disruptions at London's Heathrow Airport in January 2013 [AP, 2013][BBC, 2013][Griffiths, 2013].
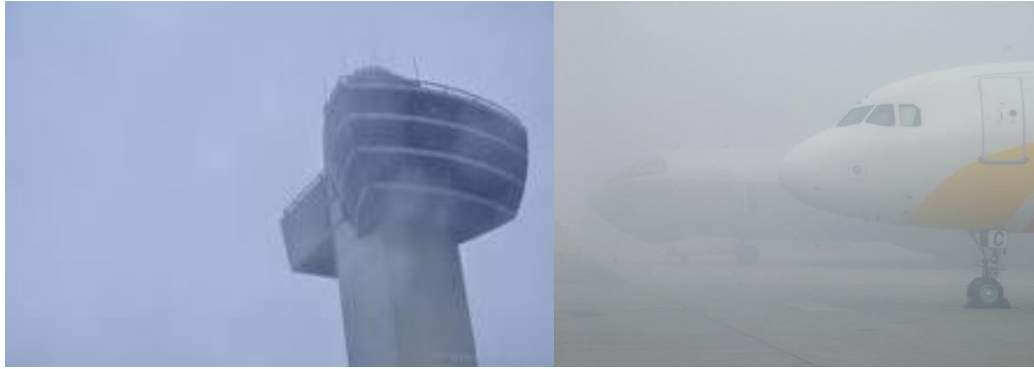
Figure 1.2. Examples of low visibility at the airport: Airport control tower (left) and airplanes (right) in foggy weather.

It is desirable that the accurate and secure location of an airplane at the airport be available in all weather conditions. In 2013, the Federal Aviation Administration (FAA) presented its plan to establish the Enhanced Low Visibility Operations (ELVO) program aiming at "Gate to Gate in Zero-Zero visibility" by 2025. This plan shows a desire for successful airplane operation from the moment when passengers board until the plane arrives at its destination in the case of no visibility at both the departing and arriving airports. This research develops algorithms to meet the integrity and availability requirements for aircraft movement on the surface of the airport using single-frequency differential GPS (satellite-based positioning systems).

The Global Positioning System (GPS) was introduced to airborne applications to improve accuracy, integrity, and availability of aircraft location information. This airborne application is supported by the Ground Based Augmented System (GBAS) that provides corrections to mitigate common GPS measurement errors between GBAS ground facilities and aircraft. Applications of GBAS consist of precision approach and the Differentially Corrected Positioning System (DCPS). Most aircraft operations at the airport belong to DCPS except for precision approach. Surface movement, such as taxiing on the ground, is also included in DCPS. The next sections briefly introduce GPS, GBAS, DCPS and surface

movement, and explain what the problems of operating surface movement within GBAS and how this dissertation contributes to resolve the problems.

# 1.1 GLOBAL POSITIONING SYSTEM

## 1.1.1 GPS OVERVIEW

The Global Positioning System (GPS) is the first fully functional Global Navigation Satellite System (GNSS). It was originally developed by the United States Department of Defense for military applications in the 1970s. The federal government made the system available for civilian use in 1983, and GPS has served over one billion users since. It not only provides three-dimensional location information for navigation applications, but also precise timing for communications and commerce [Misra, 2006].

GPS comprises a constellation of 31 MEO satellites at an altitude of 20183 km [Misra, 2006]. The satellites orbit in six planes at approximately $55^o$ inclination with respect to the equator and are separated by $60^o$ of right ascension. The orbits are arranged so that at least six satellites are within line of sight from almost everywhere on Earth's surface, and at least four satellites are visible at least $15^o$ above the horizon [Gao, 2008]. Figure 1.3 shows the orbital planes and the constellation.

When GPS is used for air navigation, it is typically not used by itself because of its measurement errors. The basic GPS measurements consist of biased and noisy estimates of ranges to the satellites. The principal source of bias is the unknown receiver clock offset relative to GPS time. The remaining errors are errors in modeling the satellite clocks and ephemeris, errors in modeling ionospheric and tropospheric delays, and errors in measuring the code and carrier phase due to multipath and receiver noise [Misra, 2006], as illustrated in Figure 1.4.

Figure 1.3. The orbital planes and constellation of GPS satellites [Defense Industry Daily, 2005].
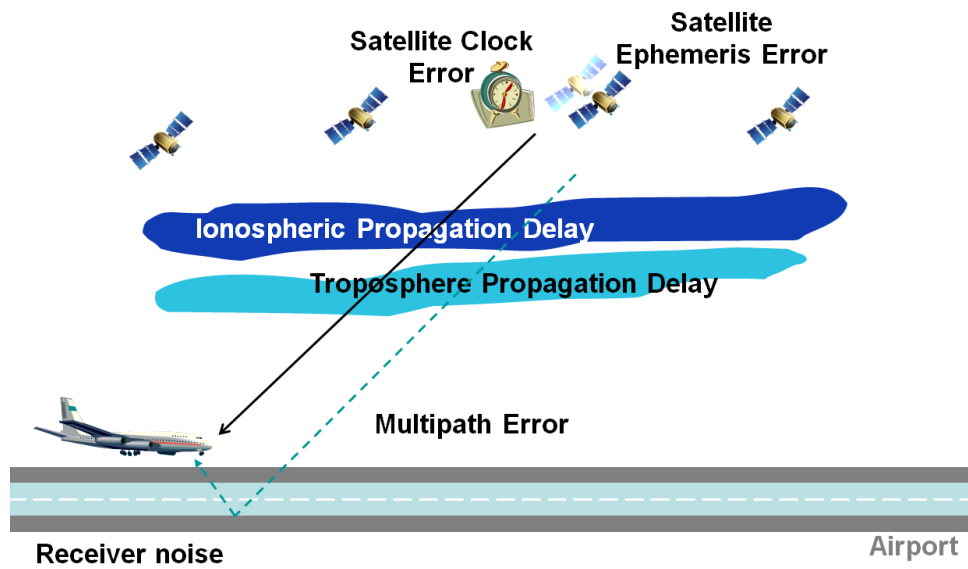


Figure 1.4. GPS measurement error sources.

If position is to be determined in real time using a single GPS receiver, the only option is to use code-based pseudoranges, perhaps smoothed by carrier phase. To further reduce the measurement errors requires a change in the mode of GPS usage from single-receiver autonomous positioning to differential GPS (DGPS) [Misra, 2006].

## 1.1.2 DIFFERENTIAL GPS

The basic idea behind DGPS is to take advantage of the fact that the errors associated with satellite clock, ephemeris, and atmospheric propagation are similar for users separated by tens or even hundreds of kilometers, and these errors vary slowly with time. In other words, these errors exhibit a high degree of spatial and temporal correlation. The closer the two users are to each other, and the closer the measurement epochs, the more similar are the errors listed above. These errors become decorrelated with increasing distance between the users and increasing time difference between their measurement epochs [Misra, 2006].

If the position of a GPS receiver is known, the combined effect of these errors can be estimated for each satellite. If these error estimates can be made available to the GPS users in the area, each user can apply them to his measurements to mitigate the errors and improve the quality of his position estimates. This is the basic idea behind DGPS. For navigation, such corrections have to be made available in real time using a radio link. In practice, a user would receive and apply the corrections with some delay, called latency. The closer a user is to the reference station, the shorter the latency and the higher the benefit from the differential corrections [Misra, 2006]. One of the systems to which DGPS is applied is the Ground Based Augmented System (GBAS), which we briefly discuss next and which we examine in more detail in Chapter 2.

# 1.2 GROUND BASED AUGMENTATION SYSTEM

## 1.2.1 GBAS OVERVIEW

A Ground Based Augmentation System (GBAS, the official international term for this type of navigation system), such as the Local Area Augmentation System (LAAS, which has traditionally referred to the U.S. version of GBAS), is a ground-based augmentation to GPS that focuses its service on the airport area (approximately a 20-30 mile radius) for precision approach, departure procedures, and terminal area operations. Current GBAS systems only monitor and augment the GPS L1 C/A-code signals [FAA, 2015].

Figure 1.5 illustrates how GBAS works. GBAS is comprised of a ground facility and avionics. The GBAS Ground Facility includes four or more reference receivers, GBAS ground processors, and a VHF data broadcast (VDB) transmitter. This ground facility is complemented by GBAS avionics installed on the aircraft. Signals from GPS satellites are received by the GBAS GPS reference receivers at known locations within a GBAS-equipped airport. The GPS reference receivers and GBAS Ground Processors work together to measure errors in pseudorange measurements from each visible GPS satellite. The GBAS ground processors produce a GBAS correction message based on the differences between actual (measured) and theoretically-calculated ranges to each satellite. Included in this message are suitable integrity parameters and approach path information. This GBAS correction message is then sent to a VDB transmitter. The VDB broadcasts the GBAS signal throughout the GBAS coverage area to avionics in GBAS-equipped aircraft. The signal coverage is designed to support the aircraft's transition from en route airspace into and throughout the terminal area airspace through precision approach and landing. The GBAS equipment in the aircraft uses the corrections provided for range and range rate to guide the aircraft safely to the runway and (potentially) to the gate.
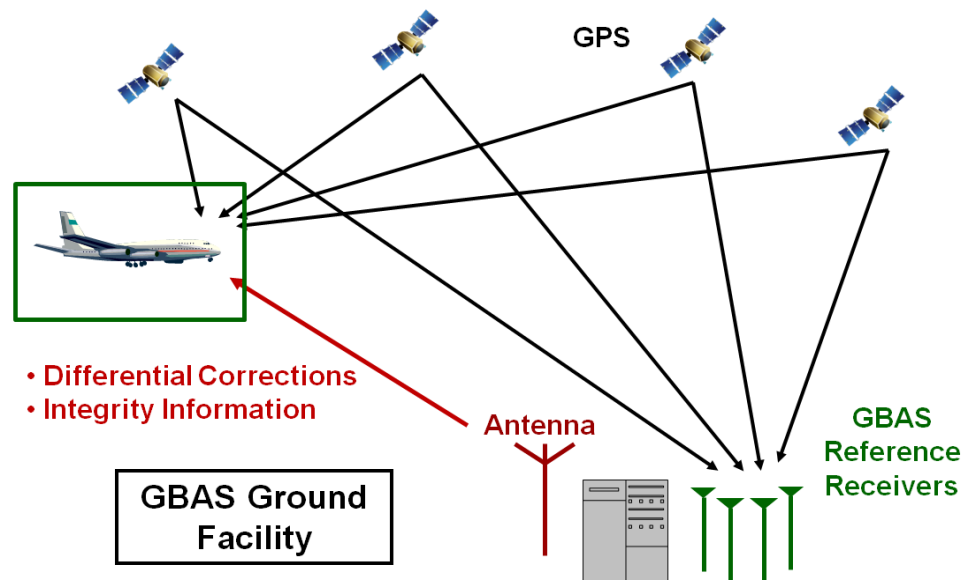
Figure 1.5. Ground Based Augmentation Systems (GBAS).

Existing GBAS installations provide Instrument Landing System (ILS)-look-alike guidance as low as 200 feet above touchdown. GBAS will eventually support landings all the way to the runway surface. The goal of GBAS implementation is to provide an alternative to the ILS supporting the full range of approach and landing operations [FAA, 2015].

As explained earlier, GBAS provides its service in the airport area for precision approach, departure procedures, and terminal area operations. As illustrated in Figure 1.6, CAT-I (required  Decision Height (DH) of 200 feet and Runway Visual Range of 550 meters, see Section 2.1) precision approach availability is typically evaluated at 6 kilometers away from the centroid of the GBAS Ground Facility reference receivers, which represents the maximum separation of the CAT-I DH for most airports [Lee, Sep 2006]. Ten nautical miles (18.5 kilometers) farther out along this approach direction marks the boundary of the Precision Approach Region (PAR). Operations outside of precision approach, meaning those that use Cartesian Position, Velocity, and Time (PVT) outputs instead of the ILS-

lookalike vertical and lateral deviations, are referred to as the Differentially Corrected Positioning Service (DCPS). Precision approach and DCPS are briefly described in the next two subsections, respectively.
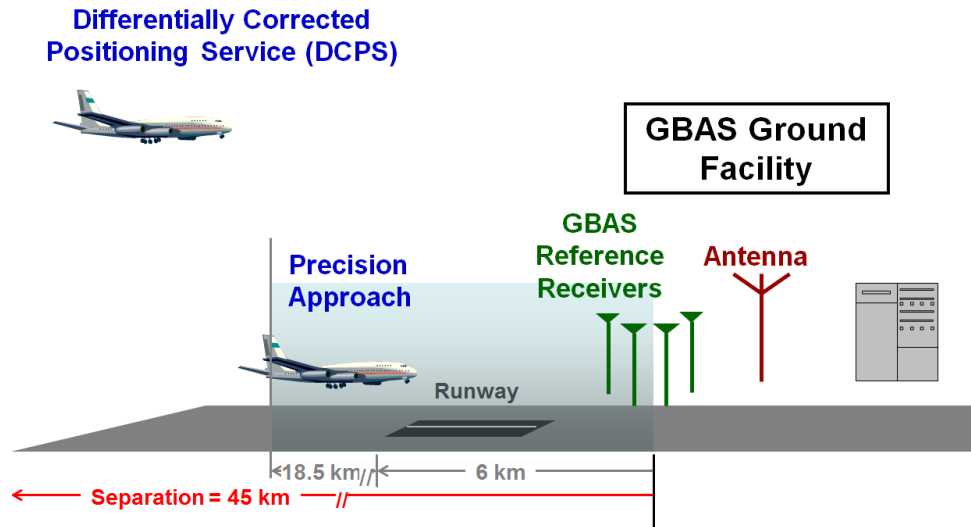


Figure 1.6. GBAS support services.

## 1.2.2 PRECISION APPROACH

The primary service that the Ground Based Augmentation System (GBAS) provides is precision approach. Precision approach is an approach where the means for measuring deviation from the desired vertical profile are provided. In other words, a precision approach is a system for approach and landing using precision lateral and vertical guidance with minima as determined by the category of operation. GBAS provides ILS-lookalike vertical and lateral deviations whose errors meet the requirements of the specified minima. Figure 1.7 illustrates an approach and landing with lateral and vertical alert limits for different approach minima. The category of operation (Category (CAT) I, II, and III) and its requirements (accuracy, availability, integrity, and continuity) for precision approach are explained in detail in Section 2.1.
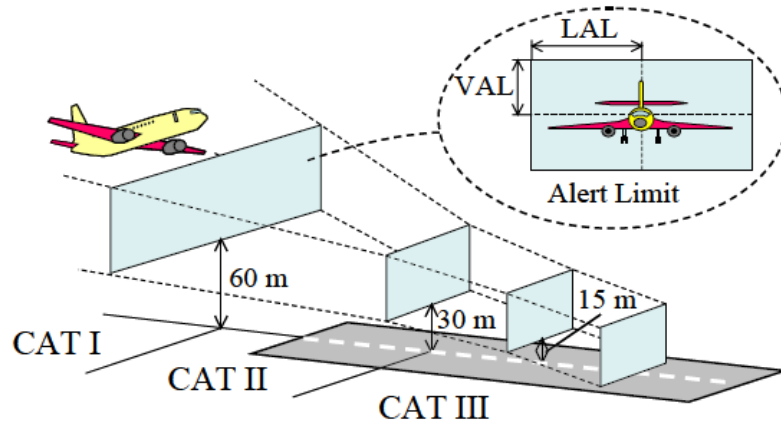
Figure 1.7. Approach and landing with alert limits [Konno, 2007].

Research and development has been actively conducted on GBAS precision approach by the FAA and many others. GBAS yields the extremely high accuracy, availability, and integrity necessary for Category I and eventually Category II and III precision approaches. GBAS demonstrated accuracy is better than one meter (95%) in both the horizontal and vertical axes in nominal conditions. A Category I (CAT I) GBAS system is available and in use in the National Airspace System [FAA, 2015]. Several national and international airports have approved GBAS stations or are expected to receive operational approval soon. Figure 1.8 shows the status of GBAS sites. More information about the current status of GBAS precision approach is available at [FAA, 2015] and [FlyGLS, 2016].

Figure 1.8. GBAS sites. Blue: Prototype/Research (with dot: actively transmitting); Yellow: S-CAT (with dot: charts published); Green: Operational (with dot: charts published); Purple: Planned installations [FlyGLS, 2016].

## 1.2.3 DIFFERENTIALLY CORRECTED POSITIONING SYSTEM

The Ground Based Augmentation System (GBAS) is primarily focused on supporting precision approach but can also be used for a variety of other applications that are collectively known as the Differentially Corrected Positioning Service (DCPS). DCPS is broadly composed of (but is not limited to) three operations. The first operation is terminal-area navigation for aircraft that uses the PVT outputs instead of the ILS-lookalike deviations. This operation includes initial approach, intermediate approach, non-precision approach, missed approach, approach to adjacent airports, and departure, as shown in

Figure 1.9. Initial approach provides a method for aligning the aircraft with the intermediate or final approach and to permit descent during the alignment. Intermediate approach positions the aircraft for the final descent to the airport. Non-precision approach is approach without electronic vertical guidance down to a decision altitude. [Wikipedia, 2016] The second operation is en route navigation for aircraft passing over the airport that can receive and make use of the GBAS VHF data broadcast (VDB). The third operation is airport surface movement for aircraft on airport taxiways (i.e., quite close to the GBAS Ground Facility centroid). Note that the VDB is required to provide coverage out to 45 kilometers assuming a 3-degree glideslope for precision approaches. At higher altitudes, aircraft will receive the VDB at significantly further distances.



Figure 1.9. Terminal area operations included in DCPS.

# 1.3 PROBLEM STATEMENT

The goal of this work is to identify the changes needed to GBAS so that it can simultaneously support airport surface movement by the aircraft. As mentioned earlier, current Ground Based Augmentation System (GBAS) only monitors and augments the GPS L1 C/A broadcast [FAA, 2015]. Using single-frequency GPS, the largest and most

important GBAS residual error sources are anomalous ionosphere and multipath, as shown in Figure 1.10. These are technical challenges of this research. The multipath of concern here is additional multipath on the airport surface that does not occur during flight. Anomalous ionosphere is applied to all the operations of the Differentially Corrected Positioning Service (DCPS), and (excessive) multipath is applied to airport surface movement in addition to anomalous ionosphere. Ionospheric anomalies are the most constraining threat to all services of GBAS. The impact of anomalous ionosphere on GBAS and its mitigation is explained in Chapter 3. CAT-I precision approach is approved under anomalous ionospheric conditions for at least a 6-kilometer separation between GBAS Ground Facility centroid and approach threshold.
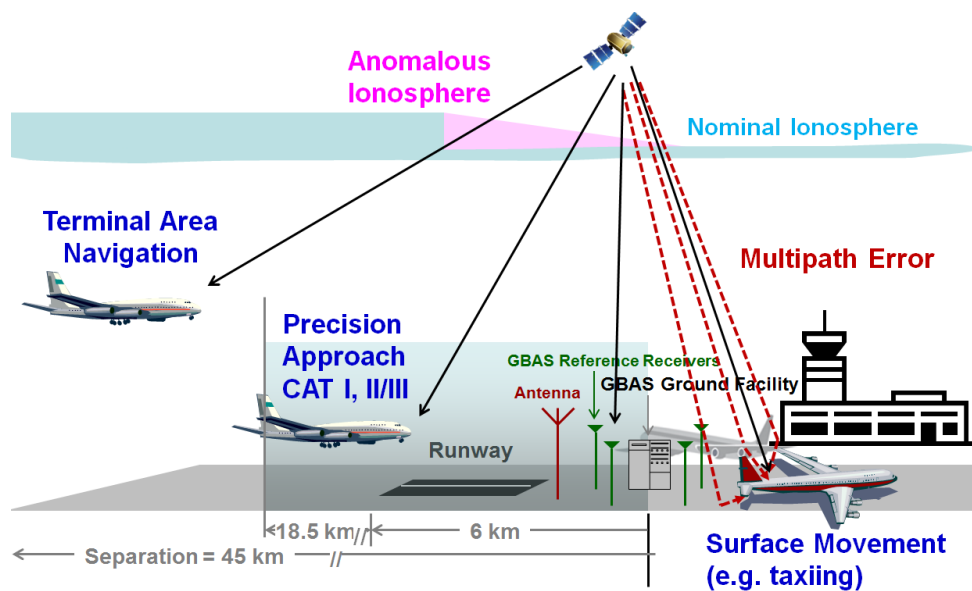


Figure 1.10. GBAS residual error sources.

GBAS Ground Facilities that support DCPS are required to meet the integrity requirements of all other operations that could use the GBAS VDB. The current GBAS requirements for DCPS integrity are that position errors should be bounded by the corresponding protection levels to the $10^{-7}$-per-hour probability level, regardless of the size of the error [FAA, 2002]

[RCTA, 2004]. Section 2.3.2 explains the concept of protection levels. This requirement is hard to achieve under severe conditions such as anomalous ionosphere which have been observed over Conterminous United States (CONUS) since 2000 [Ene, 2005] [Luo, 2005] (Section 3.1). GBAS surface movement is currently defined as one of the operations supported by DCPS. When DCPS is not enabled due to the stringent GBAS integrity requirements, GBAS surface movement cannot be enabled either.

Appendix A and Appendix B analyze DCPS integrity and show that the existing DCPS integrity requirements cannot be met by CAT I GBAS. They conclude that some future applications of GBAS that planned to use DCPS, such as airport surface movement, cannot be supported by DCPS with the CAT-I GBAS architecture. They suggest that airport surface movement should be defined as separate applications of GBAS in the same manner as precision approach.

# 1.4 RELATED RESEARCH

Unlike GBAS precision approach, research on GBAS surface movement has not been actively conducted. We are pioneers in analyzing surface movement integrity and designing surface movement applications of GBAS. The related work introduced in this section is the work of others which was adopted in this dissertation as a tool rather than previous work that is directly related to the object of this research.

The first work adopted in this research is the CAT-I anomalous ionospheric threat model by Sam Pullen *et al.* [Sam Pullen, 2009]. It is used to derive the maximum possible error under ionospheric anomalies. It has been developed based on the analysis of ionosphere data in the Conterminous U.S. (CONUS) during the anomalies in 2000 and 2003 as discovered by Datta-Barua *et al*. [Datta-Barua, 2002] and Ene *et al*. [Ene, 2005] to model anomalous ionosphere behavior quantitatively. More information about this threat model can be found in Chapter 2.

The second work brought to this dissertation is ground geometry screening for Category-I precision approach by Lee *et al.* [Lee, 2006]. It is employed to mitigate the anomalous ionospheric threat by discarding unsafe subset geometries of GPS satellites. A version of this algorithm is applied to all Category I GBAS systems approved by the FAA for use in CONUS. The algorithm is further explained in Chapter 2.

The third work adopted here is Jahn's Multipath Model by Jahn *et al.* [Jahn, 1996]. It is utilized to obtain estimates of multipath error on the airport surface. Additional GNSS multipath models relevant to airport surface movement include Brenner *et al.*, RTCA [RTCA, 1998], and Chen [Chen, 2010]. Brenner *et al.* describe the techniques used to characterize the multipath environment, the multipath models developed based on collected data and results from the Special Category I system installations and prototype GBAS test sites in [Brenner, 1998]. Chen *et al*. propose a hybrid deterministic statistical prediction simulator adapted to airport navigation based on the deterministic simulator via Monte-Carlo simulations in [Chen, 2010]. Montloin *et al*. to model the multipath ranging errors due to sources of multipath affecting GNSS pseudorange measurements during taxi and parking operations focusing on GPS L1 C/A pseudorange error models in [Montloin, 2012]. Jahn's model is used in this research because it is the simplest and complete. It is fully described in Chapter 5.

## 1.5 CONTRIBUTIONS

The main contribution of this work is to demonstrate the feasibility of the Ground Based Augmentation System (GBAS) for airport surface movement by analyzing its integrity and availability. This dissertation identifies the changes that are required and recommends specific sets of alternatives in order to enable GBAS airport surface movement and to provide sufficient integrity and availability in the presence of surface multipath in addition to anomalous ionosphere.

***Analyzed the sensitivity of airport surface movement integrity to severe ionospheric and ground multipath conditions***

When it comes to airport surface movement, multipath should be considered as a significant error source to GBAS in addition to anomalous ionosphere. As a new GBAS application, this dissertation analyzes airport surface movement integrity and quantifies its sensitivity to both ionospheric anomalies and multipath.

***Demonstrated the feasibility of GBAS for airport surface movement as a function of threat model and Maximum Acceptable Error (MAE)***

This dissertation demonstrates the feasibility of GBAS for airport surface movement as a function of threat model and Maximum Acceptable Error (MAE), the upper limit of aircraft position error. Here, the threat model includes the ground multipath model and ionospheric threat impact model, while MAE includes potential values of 10, 20, and 30 meters. Feasibility is demonstrated in terms of availability and the required aircraft geometry screening limits at the aircraft.

***Adapted GBAS integrity requirements to the new application of airport surface movement***

The Differentially Corrected Positioning System (DCPS), as it stands, cannot be enabled because it does not meet the current integrity requirements under ionospheric anomalies for all relevant operations. Hence, this dissertation proposes to make airport surface movement a new separate application of GBAS (and thus not included in DCPS) and adapts GBAS precision approach integrity requirements to the new application.

# 1.6 DISSERTATION OUTLINE

Following this introduction, Chapter 2 and Chapter 3 describe existing work related to and adapted in this research. Chapter 4 and Chapter 5 are the two main parts focusing on surface movement. The contents of these two chapters include the key contributions made in this research. The last chapter summarizes the results of this research and leverages this research to future GBAS. The following is a brief description of each chapter.

Chapter 2 provides a more detailed description of GBAS that is relevant to this research. It first introduces GBAS requirements. Then, it describes the GBAS accuracy model, including how the GBAS ground facility processes code and carrier-phase measurements and generates pseudorange corrections. Lastly, it explains the basic integrity methodology.

Chapter 3 describes the impact that extreme ionospheric spatial gradients occurring during severe ionospheric storms have on GBAS and how the U.S. GBAS mitigates the integrity risk due to these events. It identifies the largest ionospheric spatial gradients discovered within Conterminous United States (CONUS) since 2000. Then, it briefly describes the data analysis method used to examine past GPS data for large gradients and explains the simplified ionospheric anomaly "threat model" for GBAS use in CONUS generated from this data analysis. Lastly, it describes a method for limiting these worst case errors to acceptable levels via real-time broadcast integrity parameter inflation, which is implemented in the GBAS Ground Facility. This method and the ionospheric threat model are used for the error simulations in this research.

Chapter 4 shows that airport surface movement can be supported by GBAS with the design of a Horizontal Protection Level (HPL) with increased standard deviation of multipath errors or standard deviation of airborne receiver noise in airborne equipment to bound the higher multipath errors expected in the airport surface environment (as opposed to aircraft in flight). It concludes that two or more times of the standard deviation of airborne receiver noise allows us to meet the current integrity requirements and achieve the Maximum Acceptable Error (MAE) of 10 meters with more than 99% availability.

Note that the conclusion made in Chapter 4 is derived under the assumption of no nominal error contribution to Horizontal Position Error (HPE) other than worst-case ionospheric errors. However, in the surface-movement environment, airborne multipath may be a significant fraction of HPE. Limited data for airport surface movement exists at present, so examining multipath models for ground and obstruction-influenced specular reflection is the first step in exploring this further and is the subject of Chapter 5. Because, for certain

scenarios, GBAS ground facility geometry screening and a new value of the standard deviation of multipath errors using Jahn's Multipath Model for optimistic suburban environment are not sufficient by itself, the results in this dissertation include additional aircraft geometry screening to meet the requirements and lower the Maximum Acceptable Error (MAE). Since it is not clear what level of MAE corresponds to a given airport-surface operation, our goal is to minimize the achievable MAE (and thus Horizontal Alert Limit, or HAL) while maintaining useful availability.

Chapter 6 summarizes the dissertation and suggests several technical topics that are appropriate for future work.

Appendix A analyzes DCPS integrity and shows that the existing DCPS integrity requirements cannot be met by CAT I GBAS without changes to both the definition of DCPS integrity and the airborne receiver requirements under anomalous ionospheric threats.

Appendix B identifies the changes that are required to enable DCPS under ionospheric anomalies and recommends specific sets of alternatives for DCPS. It examines various combinations of additional aircraft geometry screening and integrity monitoring. One of its conclusions is that some future applications of GBAS that planned to use DCPS, such as airport surface movement, cannot be supported by DCPS with the CAT-I GBAS architecture. It suggests one important further change to the GBAS avionics requirements. Position/Velocity/Timing (PVT) applications that cannot be supported by DCPS, such as airport surface movement, should be defined as separate applications of GBAS in the same manner as precision approach.

Appendix C shows surface movement availability and sensitivity for the parameter combinations of various geometry types, inflation factors of the error standard deviation, GBAS Ground Facility-to-user separations, and geometry screening limits.

# Chapter 2

# GBAS FUNDAMENTALS

This chapter introduces the technical information about GBAS that is fundamental to understanding this research. Most paragraphs in this chapter are based on Chapter 2 of [Konno, 2007], and they are indented and in smaller font. Although the subject of this dissertation is DCPS and airport surface movement, this chapter introduces the technical fundamentals of precision approach because GBAS has been focused on precision approach. It is also necessary to understand precision approach because this research adopted ground system geometry screening for Category I precision approach to simulate the integrity and availability of surface movement.

First, this chapter describes GBAS requirements, which are the baseline of the analysis performed in this research. For GBAS, there exist well-studied system requirements which are documented in the GBAS Minimum Aviation System Performance Standards (MASPS) [RTCA, 2004]. Based on the MASPS, Section 2.1 gives an overview of the system requirements. Second, Section 2.2 derives an accuracy model that reflects expected performance under normal conditions, which is the first step for a study of safety issues. It includes how a GBAS ground facility processes carrier smoothing and provides

pseudorange corrections under normal conditions. Third, Section 2.3 introduces the basic integrity methodology for GBAS. The most important concept described in this section is the Protection Level (PL), which is a rare-event error bound that is calculated by user aircraft in real-time.

# 2.1 SYSTEM REQUIREMENTS

As shown in Figure 2.1, precision approaches and landings are classified into three categories based both on the altitude to which navigation systems provide guidance, known as the Decision Height (DH), and on the required horizontal visibility on the runway, called Runway Visual Range (RVR). The following details the specification of each category [RTCA, 2004].

*Category I (CAT I)*: Precision approaches with a DH higher than 60 meters and with an RVR of more than 550 meters.

*Category II (CAT II)*: Precision approaches with a DH between 30 meters and 60 meters and with an RVR of more than 350 meters.

*Category III (CAT III)*: While CAT III navigation systems are basically designed for automatic landing, there are three sub-classes based on the quality of ground equipment and the degree of fault tolerance of onboard guidance system via redundant avionics.

*CAT IIIa*: Precision approaches with a DH lower than 30 meters (or no DH) and with an RVR of more than 200 meters.

*CAT IIIb*: Precision approaches with a DH lower than 15 meters (or no DH) and with an RVR between 200 meters and 50 meters. CAT IIIb navigation systems can support automatic landing and rollout (down the runway).

*CAT IIIc*: Precision approaches with no DH and an RVR less than 50 meters. CAT IIIc navigation systems can support automatic landing, rollout.

Categories of approach/landing operation are classified by the International Civil Aviation Organization (ICAO) as shown in Figure 2.1. The CAT-I requirement is a Decision Height (DH) of 200 feet (60 meters) and a Runway Visual Range of 550 meters.
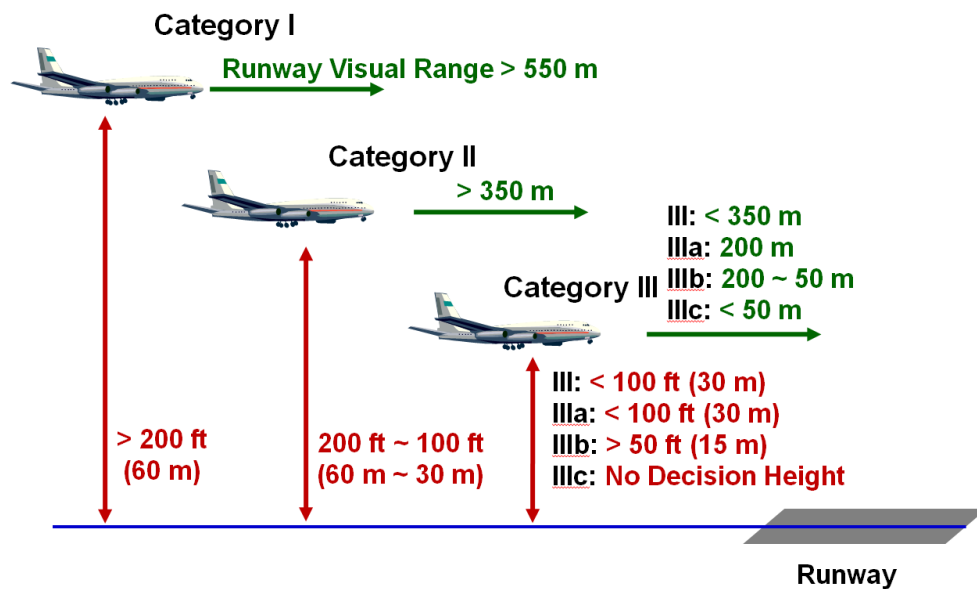


Figure 2.1. Categories of precision approach and landing classifies by ICAO.

GBAS includes the ICAO SARPs Annex 10 option for DCPS that provides a differentially-corrected position, velocity, and time (PVT) output intended to support terminal area operations. Therefore, one classification of GBAS is whether or not DCPS is currently supported by the ground subsystem. This classification, as indicated by the Reference Station Data Selector, is transmitted to the airborne subsystem via the VDB [RTCA, 2004].

GBAS ground stations, which are to be sited at each airport with GBAS service, are designed to support one or more of these categories. For each category, the

system is required to provide navigation to guide the aircraft into a specific "safe zone" that is determined such that, if the navigation system error (NSE) for a given GBAS user (i.e., the difference between reported position and true position) goes outside this area, it could result in a hazardous condition. This safe zone is called the Alert Limit (AL) and is expressed by two parameters in two orthogonal dimensions: the Lateral Alert Limit (LAL), and the Vertical Alert Limit (VAL). Figure 1.7 illustrates a landing with the alert limits shown. For safe landings, GBAS has to provide navigation whose NSE is within the AL; moreover, if a positioning error should exceed the AL due to a failure or anomaly, the system has to warn the pilot (or autopilot) within a specific time (known as the time-to-alert). To design a system that accomplishes the needed performance, there are four fundamental parameters for which specific requirements are allocated [Enge, 1999] [Pervan, 1996].

GBAS is one of the aircraft navigation systems in which GPS is used. Requirements for civil aviation operations that will be supported by GBAS have been derived from the requirements that apply to traditional navigation aids, such as ICAO Annex 10 for the Instrument Landing System (ILS) [ICAO, 2006] [RTCA, 2008]. The four key parameters upon which requirements are placed can be defined as follows [Enge, 1999] [Pullen, 2002]:

*Accuracy*: Measure of navigation output deviation from truth under nominal fault-free conditions. It is usually expressed in terms of $1\sigma$ or 95% (approximately $2\sigma$) error limits.

*Integrity*: Ability of a system to provide timely warnings when the system should not be used for navigation. *Integrity Risk* is the probability of an undetected hazardous navigation system anomaly.

*Continuity*: Likelihood that the navigation signal-in space supports accuracy and integrity requirements for the duration of intended operation. *Continuity Risk* is the

probability of a detected but unscheduled navigation interruption after initiation of operation.

*Availability*: Fraction of time the navigation system is usable as determined by compliance with accuracy, integrity, and continuity requirements.

Table 2.1 shows the requirements for accuracy, integrity, and continuity for each category specified in [RTCA, 2004]. Here, the requirements for integrity and continuity are specified in terms of a probability to be evaluated over the most critical period in an operation for each category (note that this interval may differ between the integrity and continuity requirements). For CAT IIIb, the critical period for the lateral requirement is longer than that for the vertical requirement because CAT IIIb GBAS supports operations beyond touchdown (extending through rollout) that require only lateral guidance. The GBAS Positioning Service Performance is not specified at the system level (e.g., operation specific alert limits) [RTCA, 2004]. For availability, the MASPS [RTCA, 2004] loosely specifies that "the service availability requirement shall be between 0.99 and 0.99999 for all categories" because the expected availability depends upon the operational needs of each airport.

GBAS DCPS integrity risk is defined as the probability that the non-aircraft elements provide information which results in an out of tolerance horizontal relative position error without annunciation for a period longer than the maximum time-to-alert. The information gives results when processed by a fault-free airborne subsystem using any GBAS data that could be used by the aircraft. An out of tolerance horizontal relative position error is defined as an error that exceeds the horizontal protection level. DCPS integrity risk is based on terminal area operations requirements. For ground subsystems that provide DCPS, the GBAS DCPS integrity risk shall not exceed $1 \times 10^{-7}$ per hour. This probability is independent of ranging signal geometry. The ground subsystem maximum time-to-alert shall be less than or equal to 3 seconds [RTCA, 2004].

Table 2.1. GBAS requirements

| Typical operations | Accuracy (95%) | | Integrity | | | | Continuity |
| --- | --- | --- | --- | --- | --- | --- | --- |
| | Lateral | Vertical | Integrity Probability | Time to Alert | LAL | VAL | Continuity Probability |
| Initial approach, intermediate approach, non-precision approach, departure | 220 m | N/A | $1 \times 10^{-7}$ / h (also for surface movement) | 3 sec | N/A | N/A | $1 \times 10^{-4}$ / h to $1 \times 10^{-8}$ / h |
| Non precision approach with vertical guidance NPV I | 16 m | 20 m | $1\text{-}2 \times 10^{-7}$ / approach in any 150 sec | 10 sec | 40 m | 50 m | $1\text{-}8 \times 10^{-6}$ in any 15 sec |
| Non Precision approach with vertical guidance NPV II | 16.0 m | 8.0 m | $1\text{-}2 \times 10^{-7}$ / approach in any 150 sec | 6 sec | 40 m | 20 m | $1\text{-}8 \times 10^{-6}$ in any 15 sec |
| CAT I | 16.0 m | 6.0 m to 4.9 m | $1\text{-}2 \times 10^{-7}$ / approach in any 150 sec | 6 sec | 40 m | 10 m | $1\text{-}8 \times 10^{-6}$ in any 15 sec |
| CAT II/ CAT IIIa | 5.0 m | 2.9 m | $1\text{-}1 \times 10^{-9}$ / approach in any 15 sec vert, 30 sec lat | 2 sec | 17 m | 10 m | $1\text{-}4 \times 10^{-6}$ in any 15 sec |
| CAT IIIb | 5.0 m | 2.9 m | $1\text{-}1 \times 10^{-9}$ / approach in any 15 sec vert, 30 sec lat | 2 sec | 17 m | 10 m | $1\text{-}2 \times 10^{-6}$ in any 15 sec vertical, 30 sec lateral |

Availability probability for all typical operations: 0.99 to 0.99999.

This research focuses on airport surface movement which is currently one of DCPS services. As shown in Table 2.1 above, airport surface movement must satisfy the very

stringent integrity risk requirement of $10^{-7}$ per hour, which literally means that "we can accept only one undetected hazardous navigation fault in 10 million hours of operations." This stringent requirement of "one in 10 million" motivates the need to mitigate risks that are extremely rare but can result in hazardous errors if unmitigated. Ionospheric anomalies and ground multipath are considered to be just such risks.

# 2.2 ACCURACY

Before starting a discussion of integrity, it is first necessary to understand accuracy under nominal conditions. For that, this section begins by modeling GPS range measurements subjected to various error sources and then moves on to introducing the error-reduction methods employed in GBAS. Finally, this section derives statistical parameters representing the GBAS positioning accuracy that results from the error-reduced range measurements. These parameters play an important role in the GBAS integrity methodology discussed in the next section.

## 2.2.1 GPS RANGE MEASUREMENTS

GBAS positioning errors originate from GPS range errors. Hence, the discussion of accuracy should start by understanding GPS range measurements. The currently available civil signal—the L1 signal—consists of three components [Misra, 2006].

**RF carrier:** A Radio Frequency (RF) sinusoidal signal with the frequency of 1575.42 MHz. Its wavelength is approximately 19 cm.

**Ranging code:** A unique sequence of zeros and ones that is assigned to each satellite. In particular, the civil ranging code for the L1 signal is called the C/A code. Each C/A code consists of 1023 bits, or chips, and is repeated each millisecond. Accordingly, the duration of each chip is about 1 μs; thus, its wavelength is about 300 meters, and the chipping rate is 1.023 MHz. Each code is selected based on its auto-correlation and cross-correlation properties to allow all satellites to transmit on RF carriers having the same frequency without

significantly interfering with each other. In other words, GPS receivers can distinguish each satellite by taking the correlation between the incoming signal and a receiver-generated replica of the ranging code for each satellite and checking if there is a conspicuous peak in the correlation function.

*Navigation data:* A binary-coded message consisting of data concerning the satellite health states, ephemeris (orbit parameters), clock bias parameters, and an almanac (reduced-precision ephemeris data on all satellites in the constellation). The navigation data is generated in the GPS Ground Segment and is uplinked to GPS satellites. Satellites then transmit this data at 50 bps, which is equivalent to a bit period of 20 milliseconds.

Each satellite generates its unique ranging code and combines it with its navigation data using modulo-2 addition. The combined binary signal is then modulated upon the RF carrier with Binary Phase Shift Keying (BPSK): a bit of zero leaves the RF carrier unchanged, and a bit of one shifts the phase of the carrier by 180 degrees. Figure 2.2 is a schematic of this procedure. For details of the signal structure and of the signal generation methods, the interested reader is referred to [Spilker, 1996a] [Spilker, 1996b] [Misra, 2006)].

By processing the incoming signals, GPS receivers output two types of range measurements. One is the *code-phase measurement*, and the other is the *carrier-phase measurement*. The code-phase measurement is computed from the travel time of the ranging signals. For a given satellite, the GPS receiver generates a replica of the ranging code and searches for the correlation peak between the replica and the incoming signal by shifting the replica backward and forward in time. The time offset that maximizes the correlation corresponds to the best estimate of the travel time, although it remains corrupted by the receiver's own clock error. The code-phase measurement is determined by multiplying the travel time by the speed of light in vacuum.
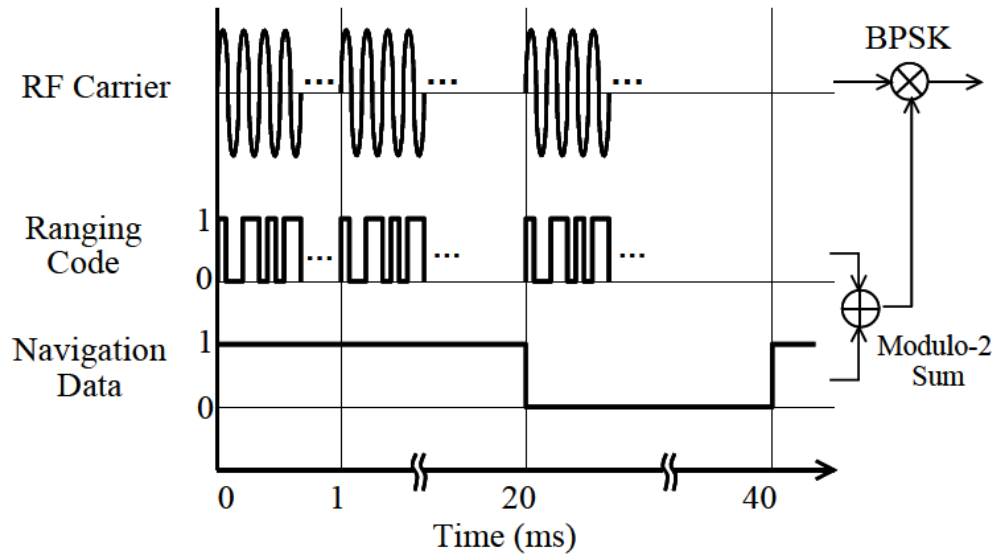
Figure 2.2. Schematic of L1 signal generation ([Konno, 2007] modified from [Misra, 2006, Figure 2.3]).

In contrast, the carrier-phase measurement is computed from the difference between the phase of the receiver-generated carrier signal and the phase of the incoming signal. Because the phase difference is observed to within a cycle of the RF carrier, the receiver measures only a fraction of a cycle. Hence, the distance between the satellite and the receiver is the measured fraction plus an unknown number of whole cycles that is referred to as the *integer ambiguity*. One needs to somehow determine this ambiguity to take full advantage of the carrier-phase measurement.

As discussed in Chapter 1, GPS range measurements are subject to various errors. Accounting for these errors, the code-measurements and carrier-phase measurements between a receiver, $j$, and a satellite, $i$, are modeled as follows.

$$\rho_j^i = r_j^i + cb_j - cB^i + E_j^i + T_j^i + I_j^i + MP_j^i + v_j^i \qquad (2\text{-}1)$$

$$\phi_j^i = r_j^i + cb_j - cB^i + E_j^i + T_j^i - I_j^i + mp_j^i + \eta_j^i + N_j^i \qquad (2\text{-}2)$$

where $\rho$ is the measured code-phase measurement, $\phi$ is the measured carrier-phase measurement, $r$ is the true distance between the satellite and the receiver antenna, $cb$ is the error due to the receiver clock offset from GPS time, $cB$ is the error due to the satellite clock offset from GPS time, $E$ is the component of the ephemeris prediction error along the line of sight between the satellite and the receiver antenna, $T$ is the tropospheric error induced by the lower atmosphere, $I$ is the ionospheric error induced by the upper atmosphere, $MP$ and $mp$ are multipath errors on code-phase measurements and carrier-phase measurements, respectively, $v$ and $\eta$ are the thermal noise errors in the receiver on code-phase measurements and carrier-phase measurements, respectively, and $N$ is the integer ambiguity multiplied by the carrier wavelength. Note that all terms are expressed in the length domain (in meters) after a proper transformation into units of length if necessary.

Table 2.2 presents a summary of typical errors on code-phase measurements and carrier-phase measurements. Among these errors, multipath, thermal noise, and ionospheric error are particularly interesting, because these errors do not have the same values between code-phase measurements and carrier-phase measurements, while the other errors are the same. Moreover, ionospheric error is one of the main focus of this research. Hence, it is worthwhile to discuss these errors in more detail.

Table 2.2. A summary of the errors in GPS measurements [Misra, 2006]

| Source | Potential error size |
|---|---|
| Satellite clock model | Clock modeling error, $cB$: 2 m (rms) |
| Satellite ephemeris prediction | Component of the ephemeris prediction error along the line of sight, $E$: 2 m (rms) |
| Ionospheric delay | Effect upon the code and the carrier is equal and opposite: The code is delayed while the carrier is advanced by the same amount.<br><br>Delay, $I$, in zenith direction ≈ 2-10 m, depending upon user latitude, time of the day, and solar activity<br><br>Delay for a satellite at elevation angle $el$ = zenith delay × obliquity factor ($el$)<br><br>Obliquity factor: 1 at zenith; 1.8 at 30° elevation angle; and 3 at 5° |
| Tropospheric delay | Code and the carrier are both delayed by the same amount.<br><br>Delay, $T$, in zenith direction at sea level ≈ 2.3-2.5 m; lower at higher altitudes<br><br>Delay for satellite at elevation angle $el$ = zenith delay × obliquity factor ($el$)<br><br>Obliquity factor: 1 at zenith; 2 at 30° elevation angle; 4 at 15°; and 10 at 5° |
| Multipath | In a 'clean' environment:<br>Code, $MP$: 0.5-1 m<br>Carrier phase, $mp$: 0.5-1 cm |
| Receiver noise | Code, $v$: 0.25-0.5 m (rms)<br>Carrier phase, $\eta$: 1-2 mm (rms) |

*Multipath and Receiver Noise*

Although multipath and receiver noise affect both code and carrier phase measurements, the errors on carrier phase measurements are significantly smaller than those on code. Typical multipath plus receiver noise errors for carrier phase measurements are about 1 cm in a clean environment with no obstructions or strong reflections, while those for code measurements are about 1 meter (see Table 2.2). The magnitude of these errors mainly depends on the wavelength of the signal used for the measurement. In general, the longer the wavelength, the larger the multipath and thermal noise errors are. Considering that the wavelength of the L1 carrier—the primary signal for the carrier-phase measurement—is about 19 cm, and that the wavelength of the C/A ranging code—a primary signal for the code-phase measurement—is about 300 meters, the significant difference in magnitude of these errors is understandable. In-depth discussions of these errors are found in [Misra, 2006].

*Ionosphere Error*

Equations (2-1) and (2-2) show that ionosphere errors on code- and carrier-phase measurements are the same in magnitude but opposite in sign. This comes from the following physics. The ionosphere is a frequency dispersive medium; that is, the refractive index is a function of the operating frequency [Klobuchar, 1996] [Misra, 2006]. The major effects of the ionosphere upon GPS range are (1) group delay of the signal modulation, or absolute range error; and (2) carrier-phase advance as compared with the hypothetical carrier-phase that would be measured in the absence of the ionosphere, or relative range error. The ionosphere error on code-phase measurements corresponds to the group delay, while the ionosphere error on carrier-phase measurements corresponds to the phase advance. To evaluate the group delay (denoted by $I_\rho$) and the phase advance (denoted by $I_\phi$), mathematical models based on the first-order approximation of the ionosphere refractive index for radio waves are widely used in the GPS community. The following equations define these models.

$$I_\rho = \frac{40.3 \cdot TEC}{f^2} \qquad (2\text{-}3)$$

$$I_\phi = -\frac{40.3 \cdot TEC}{f^2} \qquad (2\text{-}4)$$

where *f* is the carrier frequency, *TEC* (*Total Electron Content*) is the integrated number of electrons in a tube of 1 m$^2$ cross section extending from the receiver to the satellite, and "delay" is given as a positive value ("advance" has a negative value). Interestingly, as shown in (2-3) and (2-4), the magnitudes of the group delay and of the phase advance are the same (see [Klobuchar, 1996] [Misra, 2006] for a detailed explanation of why this is the case). Hence, in Equations (2-1) and (2-2), the ionosphere term (*I*) actually means the following.

$$I = I_\rho = -I_\phi = \frac{40.3 \cdot TEC}{f^2} \qquad (2\text{-}5)$$

For ionosphere error, another issue that should be noted here is the simplified geometrical model that is often used. As described above, the magnitude of ionosphere error is proportional to the total number of electrons existing along the signal path. Because the signal path length through the ionosphere is longer for a lower-elevation signal, the ionosphere error is generally larger for low-elevation satellites. In the simplified model, the ionosphere is considered to be a "thin shell" of infinitesimal thickness surrounding Earth. Based on this simplification of reality, the elevation-dependent ionosphere error (*I(El)*) is converted into an equivalent vertical ionosphere error ($I_v$) at the point of intersection of the line of sight with the thin shell (this point is called the *ionosphere pierce point*, or IPP). The conversion is done by the following equations.

$$I_v(h_I) = Oq(h_I, El) \cdot I(El) \qquad (2\text{-}6)$$

$$Oq(h_I, El) = \sqrt{1 - \left(\frac{R_e \cos(El)}{R_e + h_I}\right)^2} \qquad (2\text{-}7)$$

where $Oq(h_I, El)$ is called the *obliquity factor*, $h_I$ is the assumed height of the ionosphere shell (usually taken to be in the range of $350 - 450$ km), $R_e$ is the approximate radius of Earth's ellipsoid (taken to be 6378.1363 km), and $El$ is the elevation angle. Figure 2.3 illustrates this thin shell model.
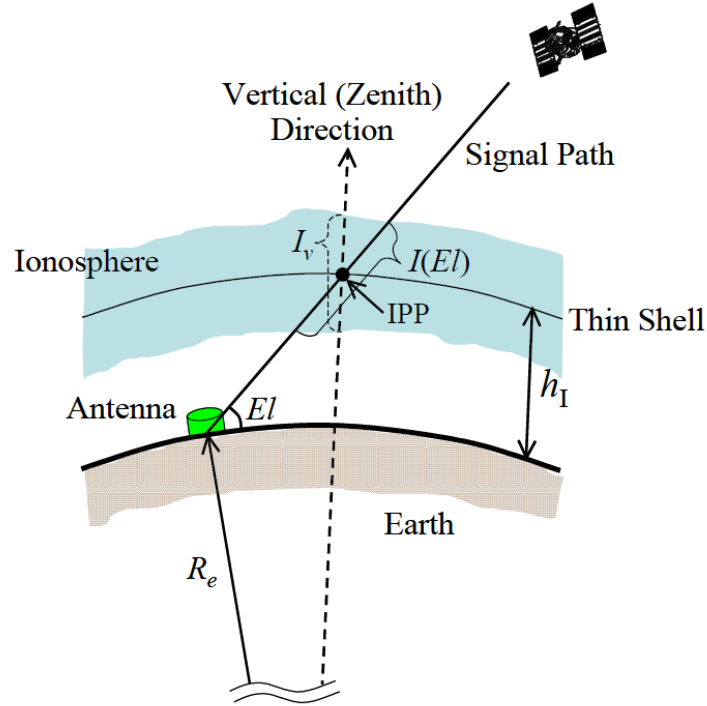


Figure 2.3. Thin-shell model and geometric conversion from slant ionosphere error to vertical ionosphere error [Konno, 2007].

In fact, this research rarely uses the thin-shell model or the vertical ionosphere error ($I_v$). However, this model is traditionally used for various purposes, and the residual ionosphere error in the conventional GBAS accuracy model is expressed in terms of vertical error and the obliquity factor for an individual satellite, as discussed in the next section. In addition, this dissertation uses the concept of the ionosphere pierce point when modeling the movement of the ranging signal path through the ionosphere.

This section has described the signal structure and the measurement models for the L1 signal. Before moving forward to the accuracy improvement methods, here is a recapitulation of the key points about GPS range measurements.

- The GPS range signal consists of the RF carrier, ranging codes, and navigation data.

- There are two types of range measurements: code-phase measurements and carrier-phase measurements.

- Multipath and thermal noise errors on code-phase measurements are significantly larger than they are on carrier-phase measurements.

- Ionosphere errors on code- and carrier-phase measurements are the same in magnitude but opposite in sign.

- Ionosphere errors on the range measurement can be approximately converted into an equivalent vertical ionosphere error using the thin shell model and corresponding obliquity factor. In this thin-shell-model concept, the point at which the line of sight intersects with the thin shell is called the *ionosphere pierce point* or IPP.

## 2.2.2 ACCURACY IMPROVEMENT: CARRIER SMOOTHING AND PSEUDO-RANGE CORRECTIONS

Code-phase measurements are the primary range measurements used in GBAS. As shown in Figure 1.4, these measurements are subject to various errors. To reduce these errors, GBAS employs two classical methods: carrier smoothing and pseudo-range correction using DGPS. Carrier smoothing affects spatially-uncorrelated errors, namely multipath and thermal noise, while pseudo-range correction reduces spatially-correlated errors, namely satellite clock biases, ephemeris errors, ionosphere errors, and troposphere errors. Figure 2.4 shows a block diagram of this error-reduction process. First, both the ground station and the user aircraft execute

carrier smoothing to reduce multipath and thermal-noise errors on their own measurements. The ground station then produces differential corrections for every satellite in view and broadcasts the corrections for satellites which pass all integrity tests. The user applies the corrections as shown in Figure 2.4, which has the effect of "calibrating the spatially-correlated errors" and estimates its position from the improved range estimates. Note that the ground station generally has two or more reference receivers located close to each other and generates a differential correction by averaging the corrections from all receivers tracking each satellite. Also note that, despite the proximity between the ground station and the user (less than 45 km), the satellites in view of the user are not always the same as those in view of the ground station. In such cases, the satellites common to both user and ground station are applied to user position estimation.

It provides the primary means for the ground to warn users of hazards by excluding satellites affected by hazards from the corrections.
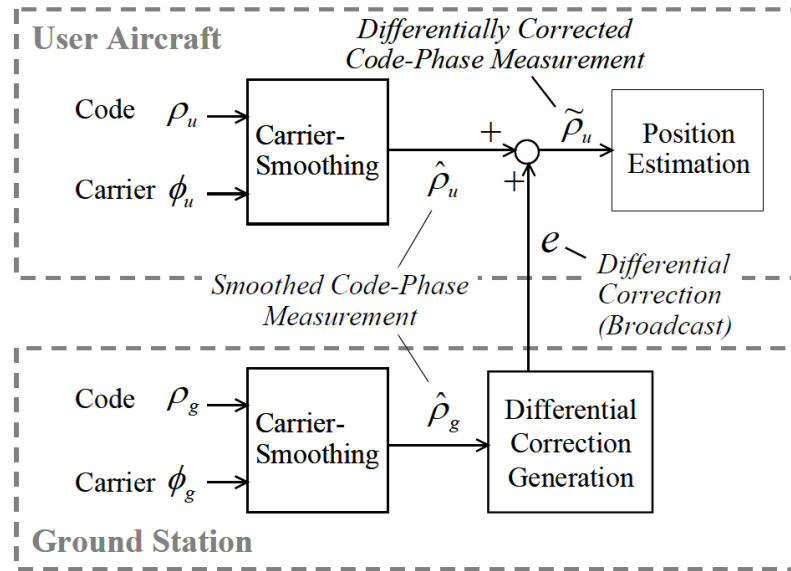


Figure 2.4. Block diagram of error reduction process in GBAS [Konno, 2007].

The remainder of this section gives a detailed introduction to carrier smoothing and pseudo-range corrections using DGPS.

### *Carrier Smoothing*

The concept of carrier smoothing dates back to the early 1980s [McGraw, 2000]. Its primary goal is to suppress multipath and thermal-noise errors on code-phase measurements by using carrier-phase measurements. To explain the mechanism of carrier smoothing, simplified models for code- and carrier-phase measurements are used.

$$\rho_j^i = R_j^i + I_j^i + \varepsilon_j^i \tag{2-8}$$

$$\phi_j^i = R_j^i - I_j^i + N_j^i \tag{2-9}$$

$$R_j^i = r_j^i + cb_j - CB^i + E_j^i + T_j^i \tag{2-10}$$

Here, $R$ includes all terms that are common between code- and carrier-phase measurements, and $\varepsilon$ is a noise term in which the multipath and the thermal noise, MP and $\nu$ in Equation (2-1), are aggregated. The multipath and the thermal noise on the carrier-phase measurements, mp and $\eta$ in Equation (2-2), are neglected due to their being very small compared to those on the code-phase measurements.

Thermal-noise errors generally exhibit weak temporal correlations. The idea of carrier smoothing is to "average out" these errors by using much less noisy carrier-phase measurements as aiding information. To this end, this method uses the complementary filter illustrated in Figure 2.5. First, the code- and carrier-phase measurements are differenced to form the Code-Minus-Carrier (CMC) parameter, $\chi$.

$$\chi = \rho - \phi = 2I - N + \varepsilon \tag{2-11}$$

The CMC parameter is then fed into a low-pass filter. Importantly, the CMC parameter does not contain the quantity of interest for the position estimation, namely, the range to the satellite. Hence, the low-pass filter operates only on the "out-of-interest" quantities (such as multipath and thermal-noise errors) without affecting the range to the satellite.

The low-pass filter is implemented as follows.

$$\hat{\chi}[t + \Delta T] = \frac{\tau - \Delta T}{\tau} \hat{\chi}[t] + \frac{\Delta T}{\tau} \chi[t + \Delta T] \qquad (2\text{-}12)$$
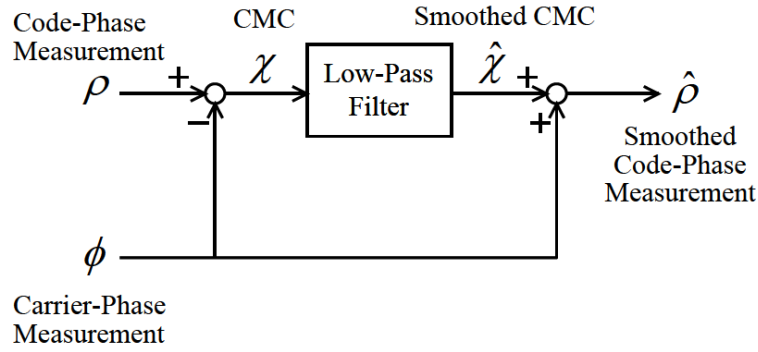


Figure 2.5. Filter structure of carrier-smoothing [Konno, 2007].

where $\hat{\chi}$ is the smoothed CMC, $\tau$ is the smoothing time constant and is conventionally set to 100 seconds in GBAS, and $\Delta T$ is the measurement update period, which is conventionally set to 0.5 seconds in GBAS. This low-pass filter can be approximated by a continuous-time filter expressed as follows in the Laplace domain.

$$\hat{\chi}(s) = F(s)\chi(s) \qquad (2\text{-}13)$$

$$F(s) = \frac{1}{\tau s + 1} \qquad (2\text{-}14)$$

The derivation of this continuous-time model is shown in Appendix A of [Konno, 2007]. This approximation is appropriate whenever the smoothing time constant ($\tau$) is significantly longer than the measurement update period ($\Delta T$).

Finally, the smoothed CMC ($\hat{\chi}$) is combined with the carrier-phase measurement to restore the range to the satellite and to cancel out the integer ambiguity ($N$). The smoothed code-phase measurement ($\hat{\rho}$) is given in the Laplace-domain as

$$\hat{\rho}(t) = R(s) + (2F(s) - 1)I(s) + F(s)\varepsilon(s) \qquad (2\text{-}15)$$

and is given in the time domain as

$$\hat{\rho}(t) = R(t) + \hat{I}(t) + \hat{\varepsilon}(t) \qquad (2\text{-}16)$$

where

$$\hat{I}(t) = \mathcal{L}^{-1}\{(2F(s) - 1)I(s)\} \qquad (2\text{-}17)$$

$$\hat{\varepsilon}(t) = \mathcal{L}^{-1}\{F(s)\varepsilon(s)\} \qquad (2\text{-}18)$$

As Equation (2-15) shows, this carrier-smoothing filter attenuates multipath and thermal noise ($\varepsilon$) without affecting the range to the satellite. However, at the same time, the filter also influences the ionosphere error ($I$). Filtering the ionosphere error is not problematic in nominal ionosphere conditions (because the impact of this error remains negligible), but it introduces a nuisance effect under anomalous ionosphere conditions. This nuisance effect is discussed in detail in Chapter 4 in [Konno, 2007], but here a discussion of pseudorange corrections using DGPS is continued assuming that everything is normal.

*Pseudorange Corrections*

After executing carrier smoothing, the ground station produces differential corrections for each satellite in view. First, the ground station computes the geometric range to the satellite, $i$, from the reference receiver, $g$:

$$r_g^i = \|\mathbf{x}^i - \mathbf{x}_g\| \tag{2-19}$$

where $\mathbf{x}^i$ is the satellite position obtained from the navigation message, and $\mathbf{x}_g$ is the precisely-surveyed position of the reference antenna. The differential correction for the satellite ($e^i{}_g$) is computed as:

$$e^i = r_g^i - \hat{\rho}_g^i = -cb_g + cB^i - E_g^i - T_g^i - \hat{I}_g^i - \hat{\varepsilon}_g^i \tag{2-20}$$

where $\hat{\rho}_g^i$ is the code-phase measurement adjusted by carrier smoothing. As mentioned above, the ground station consists of two or more reference receivers located near each other, each of which computes its own differential corrections. The corrections uplinked to the user are created by averaging the corrections from all receivers tracking each satellite.

The user aircraft applies the received corrections to its own smoothed code-phase measurements. The differentially corrected code-phase measurement, $\tilde{\rho}_u^i$, is given as follows.

$$\tilde{\rho}_u^i = \hat{\rho}_u^i + e^i$$

$$= r_u^i + cb_u - cb_g + \left(E_u^i - E_g^i\right) + \left(T_u^i - T_g^i\right) + \left(\hat{I}_u^i - \hat{I}_g^i\right) + \hat{\varepsilon}_u^i - \hat{\varepsilon}_g^i \tag{2-21}$$

Here, the second line of this equation is a precise model. However, because the difference in ephemeris error between the ground station and the user, $\left(E_u^i - E_g^i\right)$ is negligible within the GBAS service range (45 km) absent faulty ephemeris data (which should be detected before corrections are broadcast), this term is generally ignored. Accordingly, the practical model is given as:

$$\tilde{\rho}_u^i = r_u^i + cb_{ug} + T_{ug}^i + \hat{I}_{ug}^i + \hat{\varepsilon}_u^i - \hat{\varepsilon}_g^i \tag{2-22}$$

where the double-subscript notation denotes the difference between the ground station ($g$) and the user ($u$), i.e., $(\cdot)_{ug} = (\cdot)_u - (\cdot)_g$.

The user aircraft applies this differentially corrected code-phase measurement to its position estimation. Within this measurement, the receiver clock offset ($cb_{ug}$) isestimated along with position in three dimensions. Hence, the measurement errors that affect position estimation are the residual troposphere error ($T_{ug}$), the residual ionosphere error ($\hat{I}_g^u$), the smoothed multipath and thermal-noise error at the user ($\hat{\varepsilon}_u$), and the smoothed multipath and thermal-noise error at the ground station ($\hat{\varepsilon}_g$). The next section introduces statistical expressions for these errors and models the resulting positioning accuracy.

## 2.2.3 MODEL OF POSITIONING ERROR

It is necessary to understand the process of position estimation in order to move forward to positioning accuracy because the errors on range measurements are projected into the position domain through this process. Receiver position and clock bias are estimated based on a linearized GPS measurement model. Let the true position (**x**) and the true clock bias (*cb*) be represented as follows:

$$\mathbf{x} = \mathbf{x}_0 + \delta\mathbf{x} \tag{2-23}$$

$$cb = cb_0 + \delta cb \tag{2-24}$$

where $\mathbf{x}_0$ and $cb_0$ are the initial estimates for the position and the clock bias, and $\delta\mathbf{x}$ and $\delta cb$ are the unknown corrections to be applied to these initial estimates. In GBAS, the position vector is defined in the coordination system shown in Figure 2.6, where the x-axis is along-track positive forward in the local-level tangent plane, the y-axis is cross-track positive left in the plane, and the z-axis is positive up and orthogonal to the plane. When there are *N* satellites in view, the GPS measurement model is given as:

$$\hat{\boldsymbol{\rho}} - \boldsymbol{\rho}_0 = \delta\boldsymbol{\rho} = \mathbf{G}\begin{bmatrix} \delta\mathbf{x} \\ \delta cb \end{bmatrix} + \boldsymbol{\xi} \tag{2-25}$$

where $\delta\boldsymbol{\rho}$ is an *N*-dimensional vector containing the differentially-corrected code-phase measurements ($\hat{\boldsymbol{\rho}}$) minus expected ranges ($\boldsymbol{\rho}_0$) that are computed based on the satellite positions (given by the ephemeris navigation data) and the estimated user position, and $\boldsymbol{\xi}$ is an *N*-dimensional vector containing the residual errors of the differentially-corrected code-phase measurements. **G** is the *user-to-satellite geometry matrix* consisting of *N* rows, each of which is written in terms of the azimuth angle (*Az*) and the elevation angle (*El*) for the given satellite. Defining the azimuth angle as counterclockwise about the z-axis from the positive x-axis, and defining the positive elevation angle as upward from the x-y plane, the $i^{\text{th}}$ row of **G** is given as:

$$\mathbf{G}_i = [-\cos(El_i)\cos(Az_i) \quad -\cos(El_i)\sin(Az_i) \quad -\sin(El_i) \quad 1] \qquad (2\text{-}26)$$
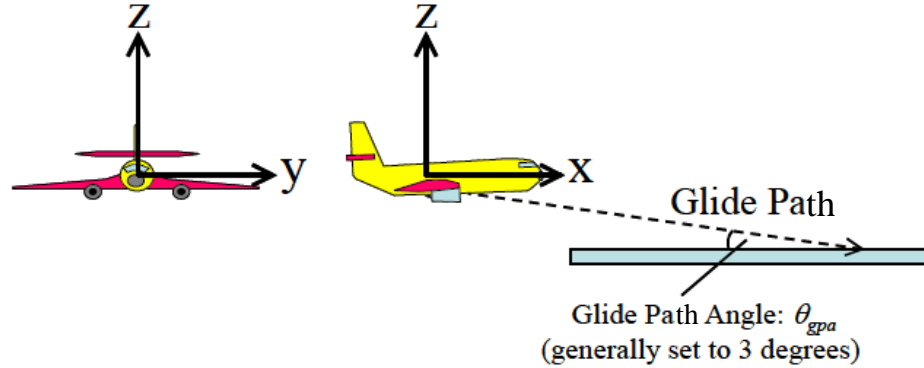


Figure 2.6. Coordinate system for GBAS position estimation [Konno, 2007].

In position estimation, $\delta\mathbf{x}$ and $\delta cb$ in Equation (2-25) are first solved by the weighted least-squares method, then the initial position and clock bias estimates are improved by substituting these solutions into Equations (2-23) and (2-24). This process is iterated until the change in the estimates $\delta\mathbf{x}$ and $\delta cb$ is sufficiently small. The weighted least-squares solution is given by:

$$\begin{bmatrix} \delta \mathbf{x} \\ \delta cb \end{bmatrix} = (\mathbf{G}^T \mathbf{W} \mathbf{G})^{-1} \mathbf{G}^T \mathbf{W} \delta \boldsymbol{\rho} = \mathbf{S} \delta \boldsymbol{\rho} \qquad (2\text{-}27)$$

$$\text{where } \mathbf{S} = (\mathbf{G}^T \mathbf{W} \mathbf{G})^{-1} \mathbf{G}^T \mathbf{W} \qquad (2\text{-}28)$$

The matrix **S** projects the range-domain information into the position domain and is called the *weighted least-squares projection matrix*. **W** is a covariance matrix of the measurements that accounts for unequal measurement quality, and its inverse is given as follows:

$$\mathbf{W}^{-1} = \begin{bmatrix} \sigma_{rm,1}^2 & 0 & \cdots & 0 \\ 0 & \sigma_{rm,2}^2 & \cdots & 0 \\ \vdots & \vdots & \ddots & 0 \\ 0 & 0 & 0 & \sigma_{rm,N}^2 \end{bmatrix} \qquad (2\text{-}29)$$

where $\sigma_{rm}$ represents the standard deviation, or *sigma*, of the differentially-corrected range measurement. Here, it is usually assumed that the measurement errors are distributed based on zero-mean Gaussians, and that these errors are uncorrelated between different satellites [Misra, 2006]. Based both on this assumption and on the linear projection from the range domain to the position domain given in Equation (2-27), the position error can be modeled as a zero-mean Gaussian distribution whose standard deviation is computed as follows:

$$\sigma_{vertial} = \sqrt{\sum_{i=1}^{N} S_{vert,i}^2 \, \sigma_{rm,i}^2} \qquad (2\text{-}30)$$

$$\sigma_{lateral} = \sqrt{\sum_{i=1}^{N} S_{2,i}^2 \sigma_{rm,i}^2} \qquad (2\text{-}31)$$

where $\sigma_{vertical}$ is the sigma of the vertical positioning error; $\sigma_{lateral}$ is the sigma of the lateral positioning error; $S_{2,i}$ is the (2, $i$) component of the projection matrix **S**, namely the projection onto the lateral component for the $i$th satellite; and $S_{vert,i}$ is the projection onto the vertical component for the $i$th satellite, which is given as:

$$S_{vert,i} = S_{3,i} + S_{1,i} \tan(\theta_{gpa}) \approx S_{3,1} \qquad (2\text{-}32)$$

where $\theta_{gpa}$ is the glide path angle for the final approach and is usually 3 degrees. In Equation (2-32), the term "$S_{1,I}\tan(\theta_{gpa})$" accounts for the effect of uncertainty in the along-track position on the vertical positioning error. This research ignores this term both because $S_{1,i}$ is generally smaller than $S_{3,i}$ and because $\tan(\theta_{gpa})$, corresponding to the glide path angle of 3 degrees, is only about 0.05.

Due to the zero-mean Gaussian assumption, positioning accuracy can be fully evaluated by computing the standard deviations $\sigma_{vertical}$ and $\sigma_{lateral}$ from Equations (2-30) and (2-31). To compute these sigmas, the standard deviation of each measurement ($\sigma_{rm}$) must be evaluated first. As discussed in the previous section, the uncorrelated error sources affecting the differentially corrected range measurements are airborne and ground receiver noise, airbone and ground multipath, residual ionosphere error, and residual troposphere error. Hence, $\sigma_{rm}$ for a specific satellite $i$ is given as follows:

$$\sigma_{rm,i}^2 = \sigma_{pr\_air,i}^2 + \sigma_{pr\_gnd,i}^2 + \sigma_{iono,i}^2 + \sigma_{tropo,i}^2 \qquad (2\text{-}33)$$

where $\sigma_{pr\_air}$, $\sigma_{pr\_gnd}$, $\sigma_{iono}$, and $\sigma_{tropo}$ represent the standard deviations for the contributing errors listed above, respectively. These "primitive" sigmas are important because $\sigma_{rm}$—a value computed from these sigmas—is used not only for evaluating positioning accuracy ($\sigma_{vertical}$ and $\sigma_{lateral}$) but for estimating position itself through the weighting matrix, **W**. In GBAS operations, the ground station has responsibility to provide users necessary information for computing $\sigma_{pr\_gnd}$, $\sigma_{iono}$, and $\sigma_{tropo}$. The remainder of this section introduces means to compute these "primitive" sigmas—methods that are widely used within the civil aviation community.

### *Model of Airborne Receiver Noise: $\sigma_{pr\_air}$*

Residual airborne receiver noise after carrier smoothing consists of residual multipath and thermal noise. McGraw *et al*. [McGraw, 2000] investigated empirical GPS range measurements taken by typical airborne receivers with a

carrier smoothing in typical airborne environments and developed standard models called *Airborne Accuracy Designators* (AADs) that express $\sigma_{pr\_air}$ (meters) as a function of the satellite elevation angle. They proposed two types of designators according to the available receiver technologies in the year 2000: AAD-A that reflects the performance of "standard" receiver technologies with *wide-correlator sampling*, and AAD-B that reflects performance of "advanced" receiver technologies with *narrow-correlator sampling*. The following equations give these models:

$$\sigma_{pr\_air}(El) = \sqrt{\sigma_{multipath}^2(El) + \sigma_n^2(El)} \qquad (2\text{-}34)$$

$$\sigma_{multipath}(El) = 0.13 + 0.53e^{-El/10} \qquad (2\text{-}35)$$

$$\sigma_n(El) = a_0 + a_1 e^{-El/\theta_c} \qquad (2\text{-}36)$$

where $\sigma_{multipath}$ represents the residual multipath, $\sigma_n$ represents the residual thermal noise, *El* represents the elevation angle given in degrees. Note that each designator has its own values for the parameters $a_0$, $a_1$, and $\theta_c$ as shown in Table 2.3. Figure 2.7 shows these models.

Table 2.3. Airborne accuracy designator parameters

| Airborne Accuracy Designator | $a_0$ (meters) | $a_1$ (meters) | $\theta_c$ (degrees) |
|---|---|---|---|
| AAD-A | 0.15 | 0.43 | 6.9 |
| AAD-B | 0.11 | 0.13 | 4.0 |
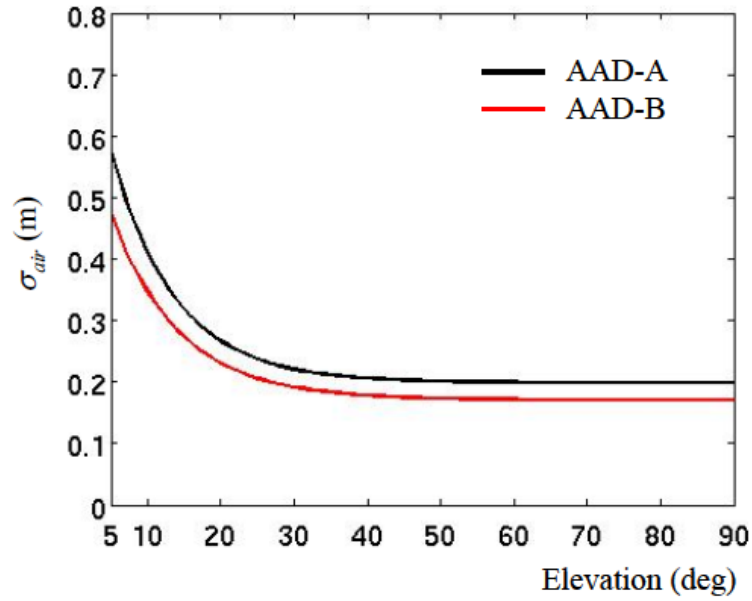
Figure 2.7. Airborne accuracy designators.

These designators are now internationally authorized [ICAO, 2006], and the MASPS [RTCA, 2004] recommends that airborne users accomplish the receiver noise level no larger than at least one of these two designators. In practice, because these designators were developed based on empirical data collected on typical Boeing aircraft models (including all models from the 737 through the 777), and because these designators include some amount of margin on the empirical data, accomplishing the noise level of either of these designators is not troublesome [Murphy, 2005]. In GBAS operations, the user aircraft evaluates $\sigma_{pr\_air}$ for each satellite using the designator that the aircraft applies and uses these sigmas to construct the weighting matrix (**W**) and to evaluate the positioning accuracies ($\sigma_{vertical}$ and $\sigma_{lateral}$).

### Model of Ground Receiver Noise: $\sigma_{pr\_gnd}$

McGraw *et al.* also developed models for ground receiver noise, investigating empirical GPS measurements taken by typical ground receivers in typical ground

station environments [McGraw, 2000]. These models are called *Ground Accuracy Designators* (GADs) and define the $\sigma_{pr\_gnd}$ (meters) as a function of elevation angle. They proposed three types of designators (GAD-A, GAD-B, and GAD-C) based on the available receiver and antenna technologies. GAD-A represents a level of performance achievable with early and low-cost GBAS installations using a standard correlator receiver and a single-aperture antenna. GAD-C was defined to characterize the performance realizable with a narrow correlator receiver and a multipath limiting antenna (MLA). GAD-C performance is expected to be able to support GBAS CAT II/III precision approaches. GAD-B represents an intermediate level of performance between GAD-A and GAD-C. The performance of GAD-B is attainable with advanced receiver technologies similar to GAD-C but with a single-aperture antenna instead of an MLA. The following equation gives these designators.

$$For\ GAD-A\ and-B\colon \sigma_{pr_{gnd}}(El) = \left\{ \frac{1}{\sqrt{M}}\left(a_0 + a_1 e^{-El/\theta_c}\right) \right.$$

$$For\ GAD-D\colon \sigma_{pr_{gnd}}(El) = \begin{cases} \frac{1}{\sqrt{M}}\left(a_0 + a_1 e^{-El/\theta_c}\right), & El \geq 35° \\ \frac{\sigma_{MAX}}{\sqrt{M}}, & El < 35° \end{cases} \tag{2-37}$$

Where *M* indicates the number of reference receivers used in the ground station, *El* is the satellite elevation angle in degrees, and each designator has its own parameters $a_0$, $a_1$, $\theta_c$, and $\sigma_{MAX}$ as shown in Table 2.4. Figure 2.8 shows these designators for M = 1.

Table 2.4. Ground Accuracy Designator parameters

| Ground Accuracy Designator | $a_0$ (meters) | $a_1$ (meters) | $\theta_c$ (degrees) | $\sigma_{MAX}$ (meters) |
|---|---|---|---|---|
| GAD-A | 0.50 | 1.65 | 14.3 | - |
| GAD-B | 0.16 | 1.07 | 15.5 | - |
| GAD-C | 0.15 | 0.84 | 15.5 | 0.24 |
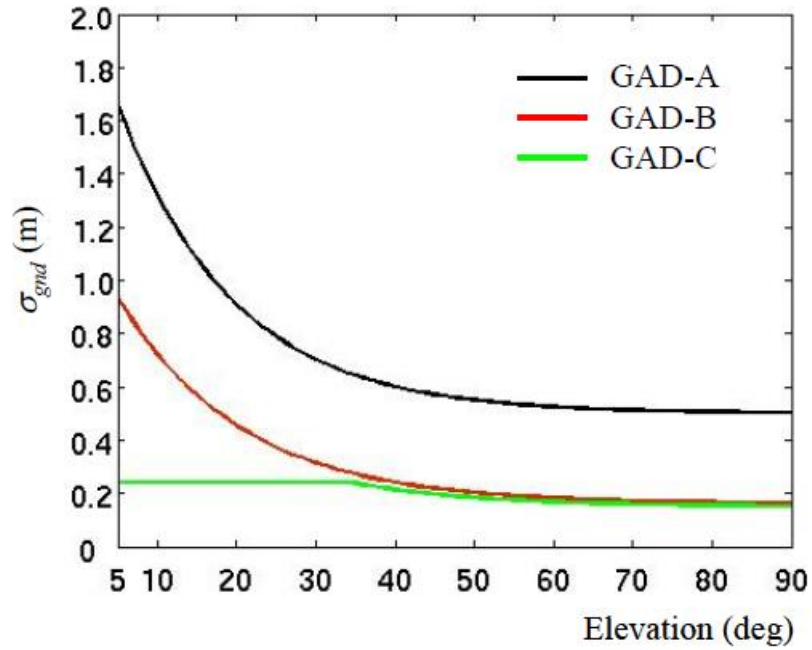


Figure 2.8. Ground accuracy designator ($M = 1$).

In a manner similar to the aircraft, each GBAS ground station must demonstrate that it meets a 95% receiver accuracy level that is consistent with at least one of these GAD curves. In addition, there is an important requirement for the ground station. In GBAS operation, the ground station is required to provide values of

$\sigma_{pr\_gnd}$ for each approved measurement that are used for ensuring integrity in the airborne system (the details of airborne integrity verification are described in the next section). Gaussian models for 95% accuracy are not generally applicable to $10^{-9}$-level integrity analyses because these models do not necessarily bound measurement errors corresponding to such small probabilities [Rife, 2004]. Therefore, although each ground station has to achieve a level of accuracy whose one-sigma error is no larger than one of the GAD models, the broadcast $\sigma_{pr\_gnd}$, which must bound errors at probabilities of $10^{-7}$ or lower, is not necessarily covered by the GAD models. Ground stations may need to broadcast values of $\sigma_{pr\_gnd}$ that exceed their GAD models based on the environments of their receiver and antenna sites.

### *Model of Residual Ionosphere Error: $\sigma_{iono}$*

Residual ionosphere errors depend on the distance between the user and the ground station. The closer the user comes to the ground station, the smaller the residual error is. The standard deviation of residual ionosphere errors, $\sigma_{iono}$ (meters), is modeled as follows [RTCA, 2008]:

$$\sigma_{iono} = \sigma_{vig} \cdot \left(d_{gu} + 2\tau v_{air}\right) \cdot Oq(h_I, El) \tag{2-38}$$

where $\sigma_{vig}$ is the standard deviation of the nominal ionosphere spatial gradient (m/km) in the vertical (zenith) domain (the subscript "*vig*" stands for *vertical ionosphere gradient*), $d_{gu}$ is the distance in kilometers between the ground station and the user, $\tau$ is the time constant of the carrier-smoothing filter and is conventionally set to 100 sec in GBAS, $v_{air}$ is the horizontal speed of the aircraft (m/s), $Oq$ is the obliquity factor (unitless) given by Equation (2-7), and $h_I$ (the thin-shell height) is set to 350 km [RTCA, 2008]. The term "$2\tau v_{air}$" in Equation (2-38) represents the additional error due to ionosphere divergence that occurs when the user aircraft traverses the ionosphere gradient over one smoothing time constant ($\tau$).

In GBAS operation, the ground station broadcasts a bounding (conservative) value of $\sigma_{vig}$ to users, which compute $\sigma_{iono}$ using the received $\sigma_{vig}$ and their own speed and position. It is suggested that the appropriate value of $\sigma_{vig}$ for Conterminous United States (CONUS) is 0.004 m/km [Klobuchar, 1996] [Lee, 2007].

*Model of Residual Troposphere Error: $\sigma_{tropo}$*

Residual troposphere errors depend on the prevailing atmosphere conditions around the ground station and on the altitude of the approaching user. The lower the user altitude is, the smaller the residual error. The standard deviation of the residual troposphere errors, $\sigma_{tropo}$ (meters), is modeled as follows [RTCA, 2008]:

$$\sigma_{tropo} = \sigma_N h_0 \frac{10^{-6}}{\sqrt{0.002 + \sin^2(El)}} \left( 1 - e^{\frac{-\Delta h}{h_0}} \right) \qquad (2\text{-}39)$$

where $\sigma_N$ is the uncertainty of the refractivity index (unitless), $h_0$ is the troposphere scale height in meters, and $\Delta h$ is the aircraft altitude in meters. Physical explanations about $\sigma_N$ and $h_0$ are found in [Misra, 2006] [McGraw, 2000], but an important point is that these parameters depend on the meteorological condition at each site and that the ground station has the responsibility to broadcast the parameters ($\sigma_N$ and $h_0$) that are consistent with prevailing conditions at that site. In practice, the parameters may be set to constant values that cover the worst-case conditions determined in advance by a meteorological investigation of the site [McGraw, 2000].

This section has described how to evaluate the GBAS user position errors, $\sigma_{vertical}$ and $\sigma_{lateral}$. In fact, these sigmas are also used to compute *Protection Levels* (PLs) in both the vertical and lateral directions. The PL is a very important parameter for integrity that measures the reliability of the position estimation. The next section provides an overview of the GBAS integrity methodology, including the PL concept.

# 2.3 INTEGRITY METHODOLOGY

GBAS R&D efforts have developed methods to ensure integrity against various faulty situations. The concept of the *Protection Level* (PL)—a position-domain error bound computed by the user aircraft—takes a central role in these integrity methods. This section surveys the GBAS system architecture from the integrity perspective and provides a basic understanding of how PLs are used in GBAS.

## 2.3.1 SYSTEM ARCHITECTURE FROM INTEGRITY PERSPECTIVE

As discussed in Section 2.1, integrity is the ability of the system to warn the pilot within a specific time if the aircraft's position error exceeds a pre-specified *Alert Limit* (AL). Because the concept of integrity is most relevant in the user's position domain, and because only the user knows which satellites from the set approved by the ground station are being applied to position calculations, the user aircraft should make the final determination of position-domain integrity during the operation. To this end, the user computes a real-time position error bound called the Protection Level (PL) and evaluates whether the current positioning error is bounded within the AL or not. In order for users to properly determine this, the ground station has responsibility to provide information about the quality of the GPS ranging signals. To do this, the ground station executes several integrity monitoring algorithms that detect and exclude faulty signals. To make clear the basic roles of the PL and the integrity algorithms, this section introduces what risk sources are currently identified and specifies which risks are mitigated by the integrity algorithms prior to the broadcast of differential corrections and which risks are mitigated by the user calculation of PLs after differential corrections are received during a given time epoch.

Recall that the allowable integrity risk for CAT IIIb GBAS is $10^{-9}$ for any 15-second exposure time in the vertical dimension or any 30-second exposure time in the lateral dimension. Because GBAS will be exposed to more than one risk source that can induce a hazardous positioning error, this allowable risk must be

interpreted as the sum of tolerances for these potential risk sources. GBAS research and design efforts have identified these risk sources and have allotted the total allowable risk to these sources based on their relative importance and severity. Figure 2.9 shows this integrity allocation tree for CAT III precision approach [RTCA, 2004].
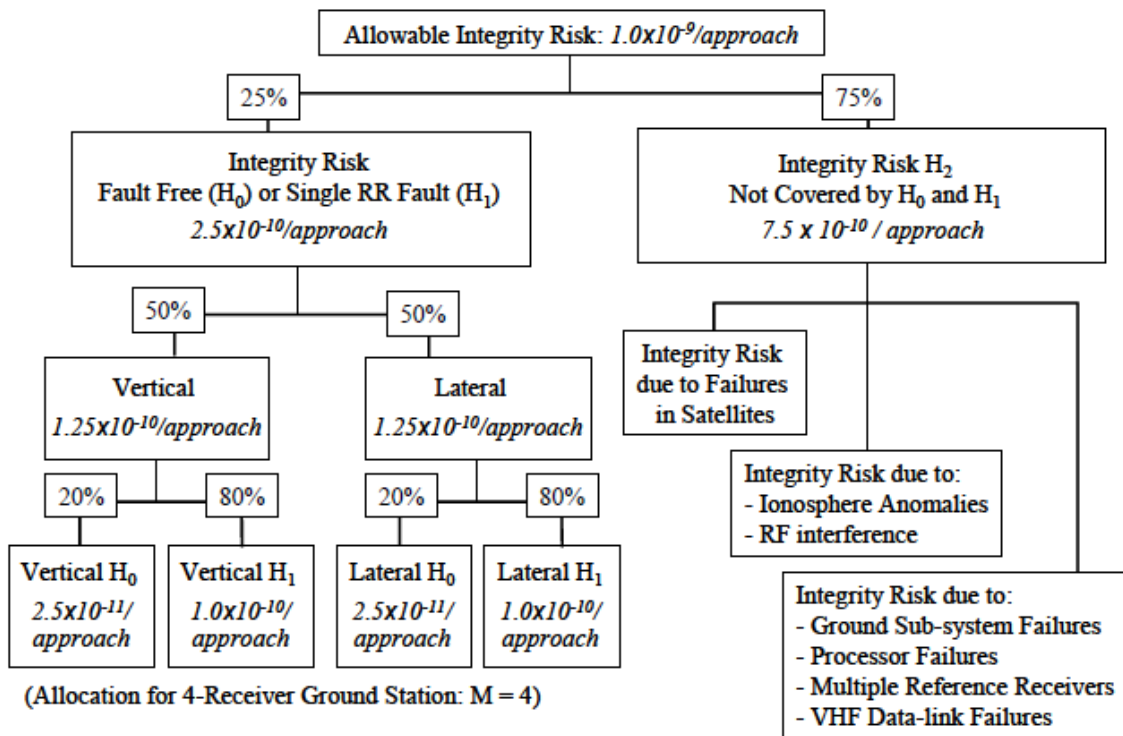


Figure 2.9. GBAS integrity allocation tree [RTCA, 2004].

As this figure shows, the risk sources are first divided into three categories: risk under fault-free conditions, which is called $H_0$ risk; risk under undetected single (not multiple) reference receiver failures, which is called $H_1$ risk; and all other risks not covered by the $H_0$ and $H_1$ risks, which are on the whole called $H_2$ risks and which include ionospheric anomalies. The fault-free condition ($H_0$) is considered because "fault-free" does not mean "error-free." Even under the fault-free condition, where the GPS satellites, the airborne and ground receivers, and the

medium that GPS signals travel through all behave normally, it is impossible to bound the positioning error within a finite value with absolute confidence. In other words, there always exists a tiny chance that a position error exceeds the AL.

A quarter of the total allowable risk is allocated to the $H_0$ and $H_1$ risks. This allocation is further divided in half such that 50% is given to the vertical dimension and 50% is given to the lateral dimension. Then, each remaining sub-allocation is equally divided among the $H_0$ and $H_1$ risks in accordance with the number of reference receivers. For example, if there are two reference receivers (receivers A and B), the risk is divided into three cases: the fault-free case, the failure of receiver A, and the failure of receiver B. The example shown in Figure 2.9 is for a typical four-receiver ground station ($M = 4$).

The remaining three quarters of the total allowable risk is allocated among all $H_2$ risk categories. However, unlike the $H_0$ and $H_1$ risks, there is no required method for further sub-allocations for each of the $H_2$ risks to be conducted—these sub-allocations are the responsibility of each GBAS ground system manufacturer.

DCPS integrity risk is based on terminal area operations requirements. For ground subsystems that provide DCPS, the GBAS DCPS integrity risk shall not exceed $1 \times 10^{-7}$ per hour. As with the precision approach service, DCPS integrity risk is allocated between ground sub-system integrity risk and protection level integrity risk, as shown in Figure 2.10. The DCPS integrity requirement has been allocated between the $H_0$ and $H_1$ hypotheses and all other failure conditions. This allocation methodology is similar to that used for the GBAS approach service, although the proportions allocated are different. For ground sub-systems that provide DCPS, the DCPS protection level integrity risk shall be less than $10^{-9}$ per hour. The integrity risk in all cases other than the fault-free case ($H_0$) or the single reference receiver failure case ($H_1$) shall not exceed $9.9 \times 10^{-8}$ per hour. The majority of the DCPS allocation ($0.99 \times 10^{-7}$ / hour) is given to the non $H_0$ and non $H_1$ risks. This is because analysis indicated that there was significant margin in the protection level allocations. The non-$H_0$/$H_1$ integrity risk must be further sub-allocated by the service

provider or manufacturer to failures in the ground sub-system and ranging sources, similar to the failure modes for precision approach [RTCA, 2004].
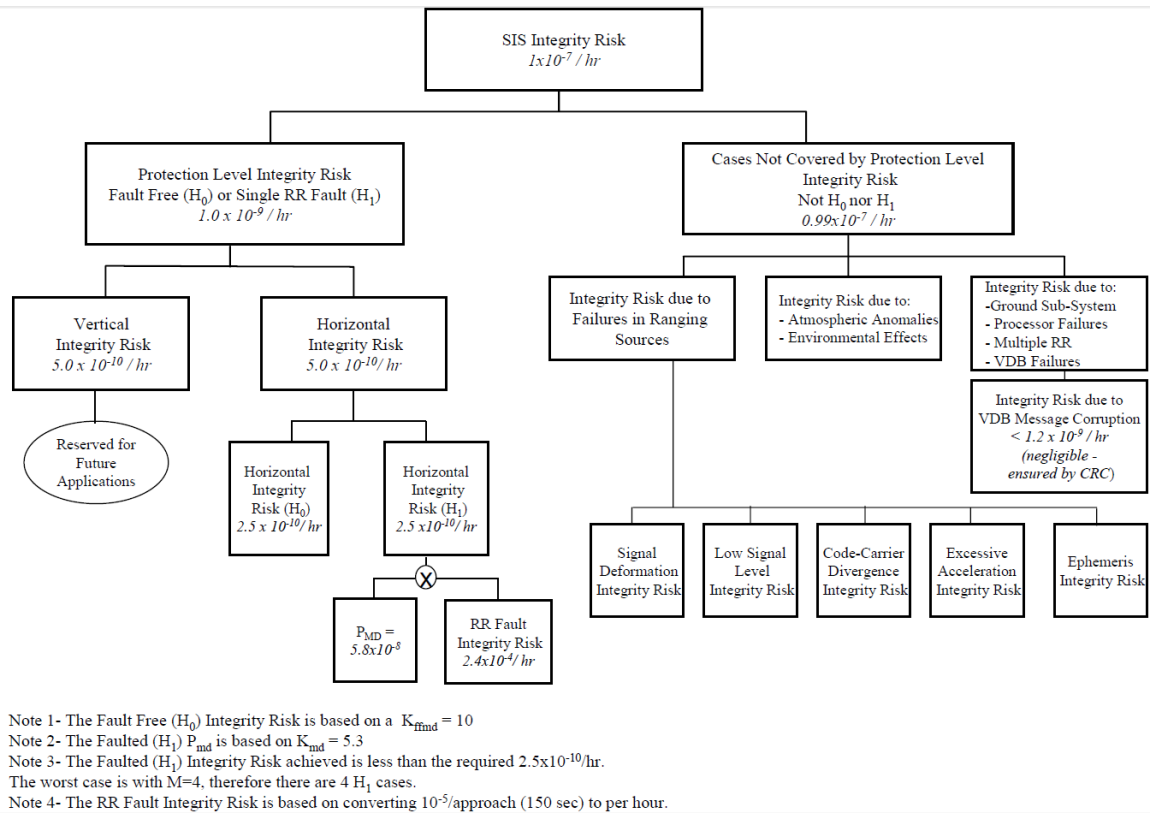


Figure 2.10. DCPS integrity risk [RTCA, 2004].

The integrity associated with $H_0$ and $H_1$ risks is ensured by user PL calculations, and the integrity associated with the $H_2$ risks is ensured by integrity monitoring methods implemented in the ground station (the only exception is the integrity risk due to large ephemeris errors, for which a PL variation called $PL_e$ has been introduced [Pullen, 2001] [Pervan, 2005]).

Figure 2.11 illustrates the GBAS system architecture from the integrity perspective. The main objective of the ground-based integrity methods is to detect satellites whose ranging signals are most probably affected by the risk sources classified in

the $H_2$ risks and to exclude these satellites from user position estimation. This exclusion is generally done by broadcasting differential corrections and integrity information associated only with the remaining satellites that have been verified to be fault-free.
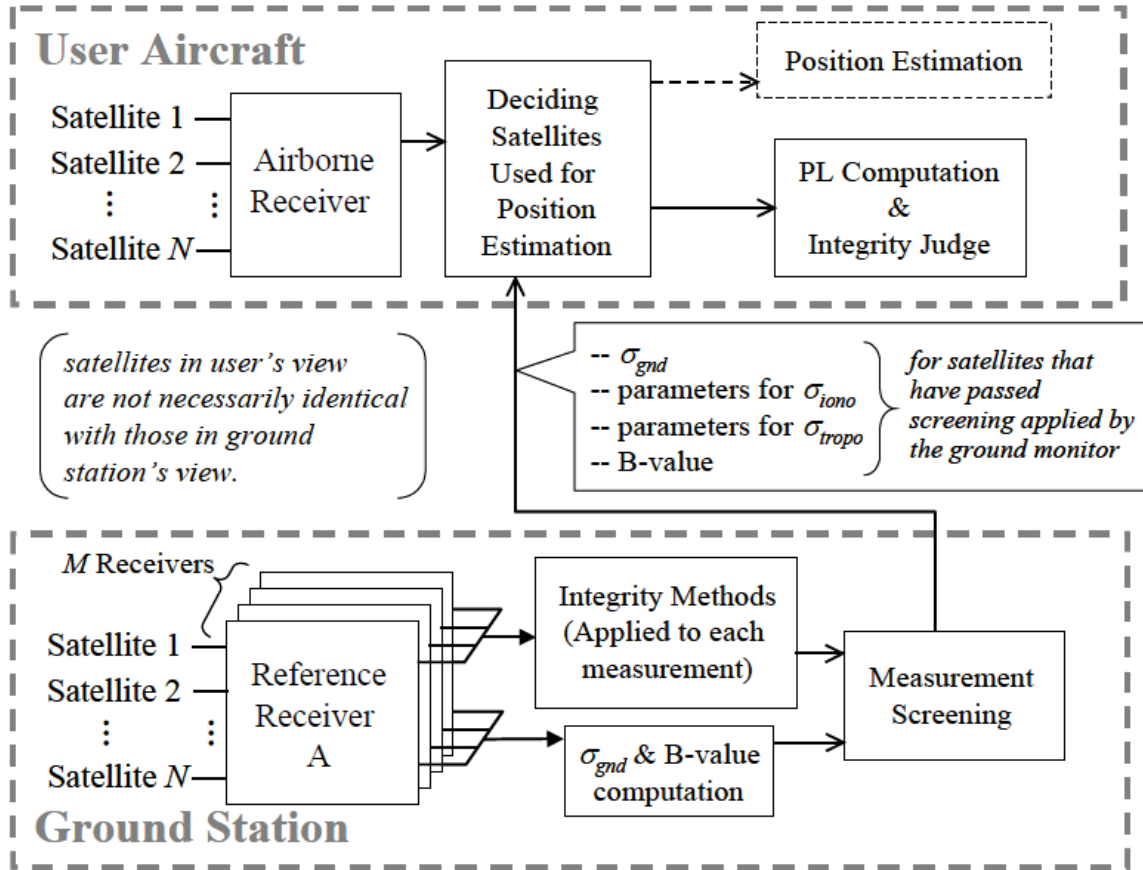


Figure 2.11. System architecture from integrity perspective [Konno, 2007].

The integrity information consists of $\sigma_{pr\_gnd}$ (or $\sigma_{gnd}$), parameters for $\sigma_{iono}$ (specifically $\sigma_{vig}$), parameters for $\sigma_{tropo}$ (specifically $\sigma_N$ and $h_0$), and *B-values*, all of which are used to evaluate the PL (B-values are described in the next subsection). Because the measurements that remain after ground screening can be considered to be either those under the fault-free condition ($H_0$) or those under the undetected single reference receiver failure condition ($H_1$), the error bound computed from

these measurements will represent what the PL should be. Keep in mind that if the ground-based methods fail to detect faulty measurements, the resulting PL may fail to bound the actual positioning error; consequently, the landing is possibly exposed to a dangerous situation. To ensure that the risk of a hazard is acceptably low, the prior probability of this condition times the probability of missed-detection of the relevant ground-based algorithms must be no greater than the integrity risk sub-allocation associated with this condition.

## 2.3.2 PROTECTION LEVEL CONCEPT

The Protection Level (PL) is in fact a generic name for two parameters in GBAS: the *Vertical Protection Level* (VPL) for the vertical dimension, and the *Lateral Protection Level* (VPL) for the horizontal dimension. System performance, such as availability, is typically dictated by the error bound in the vertical direction (namely the VPL) both because the *Vertical Alert Limit* (VAL) is tighter than the *Lateral Alert Limit* (LAL) (see Table 2.1. GBAS requirements) and because the geometric diversity of the GPS satellite constellation is the poorest in the vertical direction, typically causing larger vertical errors than horizontal errors when all else is equal. Therefore, the following discussion will consider the VPL only. The extension to the lateral direction (LPL) is straightforward and is nearly identical in form.

Let us think about the $H_0$ hypothesis. $VPL_{H0}$ is defined to satisfy the following equation:

$$\Pr\left(\text{vertical error} > \text{VPL}_{H_0} \mid H_0\right) \Pr(H_0) = \gamma_{H0-vertical} \qquad (2\text{-}40)$$

where $\Pr(H_0)$ is the *a priori* probability that the $H_0$ hypothesis is realized, and $\gamma_{H0-vertical}$ is the allowable integrity risk for vertical $H_0$ integrity. If $VPL_{H0}$ is less than VAL, the probability that a vertical error exceeds VAL given the $H_0$ condition is theoretically less than the tolerance ($\gamma_{H0-vertical}$). Conversely, if $VPL_{H0}$ is greater than VAL, it cannot be guaranteed that the probability of an error exceeding VAL

is less than this tolerance. Therefore, in order to assure integrity under fault-free conditions, the airborne subsystem computes $VPL_{H0}$ in real time and warns the pilot if $VPL_{H0}$ ever exceeds VAL. Figure 2.12 illustrates this concept.
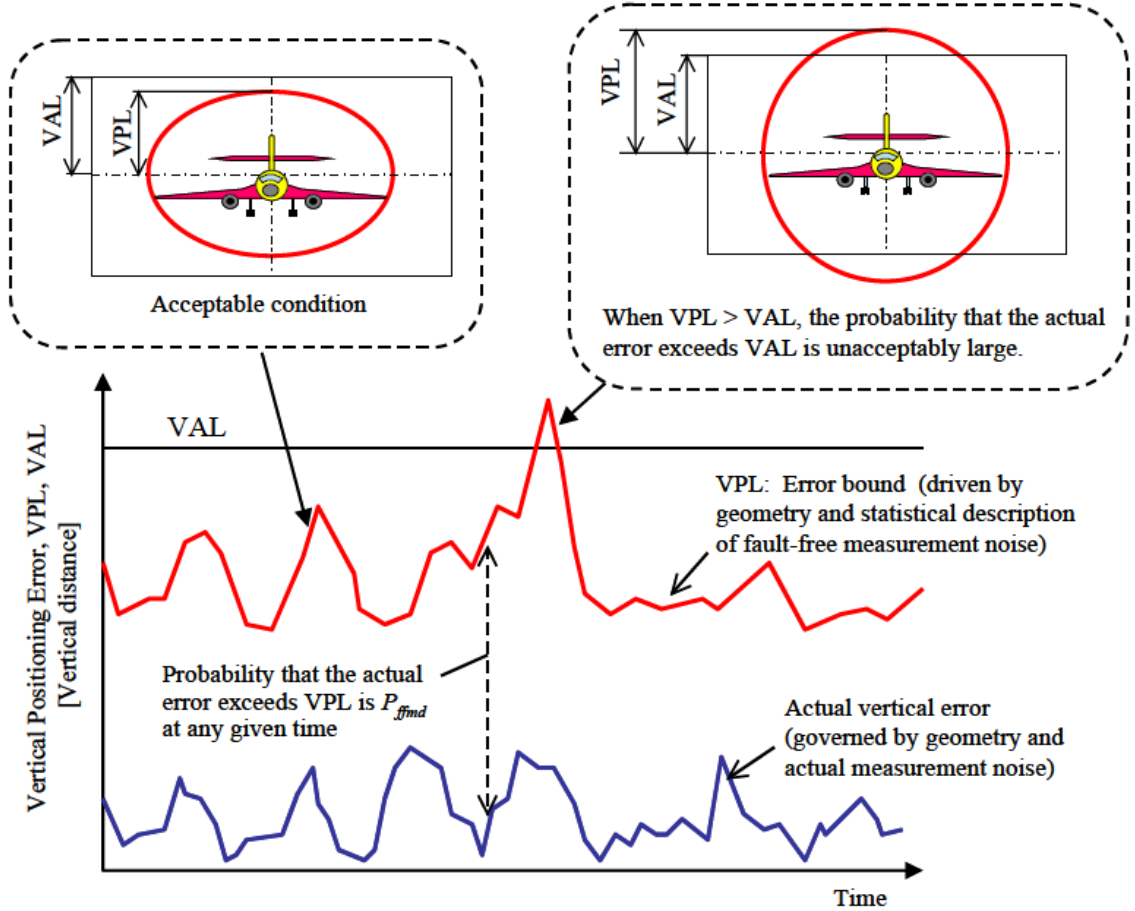


Figure 2.12. Integrity determination using protection level [Konno, 2007].

A closed-form equation to evaluate $VPL_{H0}$ is derived as follows. Manipulating Equation (2-40) yields the following equation:

$$\Pr\left(\text{vertical error} > VPL_{H_0} \mid H_0\right) = \frac{\gamma_{H0-vertical}}{\Pr(H_0)} = P_{ffmd} \qquad (2\text{-}41)$$

where $P_{ffmd}$ can be interpreted as the maximum allowable risk that the vertical error exceeds the $\text{VPL}_{H0}$ given the fault-free condition (the subscript "*ffmd*" stands for fault-free missed detection). As discussed in Section 2.2, under fault-free conditions, the distribution of vertical position errors is modeled as a zero-mean Gaussian with the standard deviation of $\sigma_{vertical}$ (see Equation (2-30)). Hence, the value of $\text{VPL}_{H0}$ can be determined by integrating this probability density up to $P_{ffmd}$.

$$\text{VPL}_{H0} = -Q^{-1}(P_{ffmd}/2) \cdot \sigma_{vertical} \tag{2-42}$$

Figure 2.13 schematically expresses the relationship between $\text{VPL}_{H0}$ and the position-error distribution. The bell-shape curve shows the zero-mean Gaussian error distribution. The Q-function in Equation (2-42) represents the cumulative probability in the negative-side tail of the Gaussian error distribution outside $\text{VPL}_{H0}$, which is the red-shaded area on the negative side of the plot.

As an example, let us derive the equation for $\text{VPL}_{H0}$ associated with a four-reference-receiver ground station. As shown in Figure 2.9, the tolerance for the vertical $H_0$ condition ($\gamma_{H0-vertical}$) is 2.5 x $10^{-11}$. The prior probability of the $H_0$ condition, $\text{Pr}(H_0)$, is generally (and conservatively) set to one because the system should work normally almost all the time. Accordingly, $\text{VPL}_{H0}$ for this configuration is given as follows.

$$\text{VPL}_{H0} = -Q^{-1}\left(\frac{P_{ffmd}}{2}\right) \cdot \sigma_{vertical} = -Q^{-1}\left(\frac{\gamma_{H0-vertical}}{2\text{Pr}(H_0)}\right) \cdot \sigma_{vertical}$$

$$= 6.673\sigma_{vertical} \tag{2-43}$$

Recall that the computation of $\sigma_{vertical}$ requires four "primitive" sigmas—$\sigma_{pr\_air}$, $\sigma_{pr\_gnd}$, $\sigma_{iono}$, and $\sigma_{tropo}$ (see Equations (2-30) and (2-33)). The user evaluates $\sigma_{pr\_air}$ by itself, and the necessary information to evaluate the other sigmas is provided by the ground station (see Figure 2.11). Therefore, the user can evaluate $\text{VPL}_{H0}$ in real time and thus assure themselves of sufficient integrity under fault-free conditions.
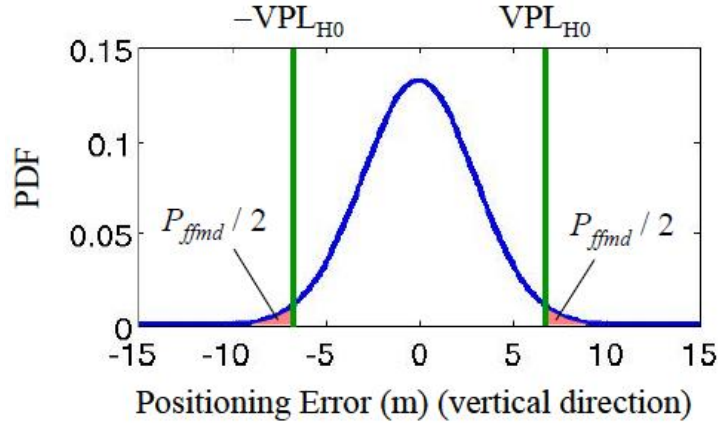
Figure 2.13. Position error distribution under fault-free conditions and VPL$_{H0}$ [Konno, 2007].

The VPL for the H$_1$ condition—undetected single reference receiver failure—can be derived based on the same framework as VPL$_{H0}$. An important difference between H$_0$ and H$_1$ conditions is the distribution of differential correction errors corresponding to each condition. The error distribution under the H$_0$ condition is a zero-mean Gaussian with a bounding standard deviation of $\sigma_{pr\_gnd}$. In contrast, the error distribution for the H$_1$ condition is modeled as a biased Gaussian whose bias is caused by an undetected reference-receiver malfunction. These biased-distributed differential corrections result in biased-distributed position errors; thus, the VPL$_{H1}$ equation must take these biases into account. Figure 2.14 shows this concept. The left-hand figure shows the distribution of the differential corrections for a particular satellite which has a bias due to a reference-receiver malfunction, and the right-hand figure shows the resulting position-error distribution. The ground station estimates the bias for each differential correction and provides these estimates to the user, which computes VPL$_{H1}$ using them. These bias estimates

provided by the ground are called *B-values*, and the $VPL_{H1}$ equation is given as follows:

$$VPL_{H1} = \max\{VPL_{H1,j}\} \text{ where } j \text{ represents a receiver } (j = 1, \ldots, M) \quad (2\text{-}44)$$

$$VPL_{H1,j} = K_{md}\sqrt{\sum_{i=1}^{N} S_{vert,i}^2 \sigma_{H1,i}^2} + \left|\sum_{i=1}^{N} S_{vert,1} B_{i,j}\right| \quad (2\text{-}45)$$

$$\sigma_{H1,i}^2 = \frac{M}{M-1}\sigma_{gnd,i}^2 + \sigma_{air,i}^2 + \sigma_{iono,i}^2 + \sigma_{tropo,i}^2 \quad (2\text{-}46)$$

For the four-reference-receiver ground station ($M = 4$), the inflation factor $K_{md}$ ("*md*" stands for missed-detection) is given as 3.7 (unitless). It is less than equivalent factor $K_{ffmd}$ for the H0 case in equation (2-43) to make the system safer with smaller VPL. Note that the ground station does not need to specify which receiver is faulted, as it automatically computes *B-values* for all reference receivers under the hypothesis that each one is failed (one at a time). The detailed logic behind Equations (2-44), (2-45), and (2-46) is found in [RTCA, 2004], and the method to compute *B-values* is described in Appendix B in [Konno, 2007]. As with $VPL_{H0}$, if $VPL_{H1}$ is less than VAL, user integrity associated with the $H_1$ hypothesis is guaranteed.

Between $VPL_{H0}$ and $VPL_{H1}$, the larger of $VPL_{H0}$ and $VPL_{H1}$ (and VPL_e) is compared to VAL for real-time integrity verification. When all reference receivers are nominally functioning, $VPL_{H0}$ tends to dominate over $VPL_{H1}$. In contrast, if a particular reference receiver fails, $VPL_{H1}$ tends to be larger than $VPL_{H0}$.

Range-to-Position Mapping
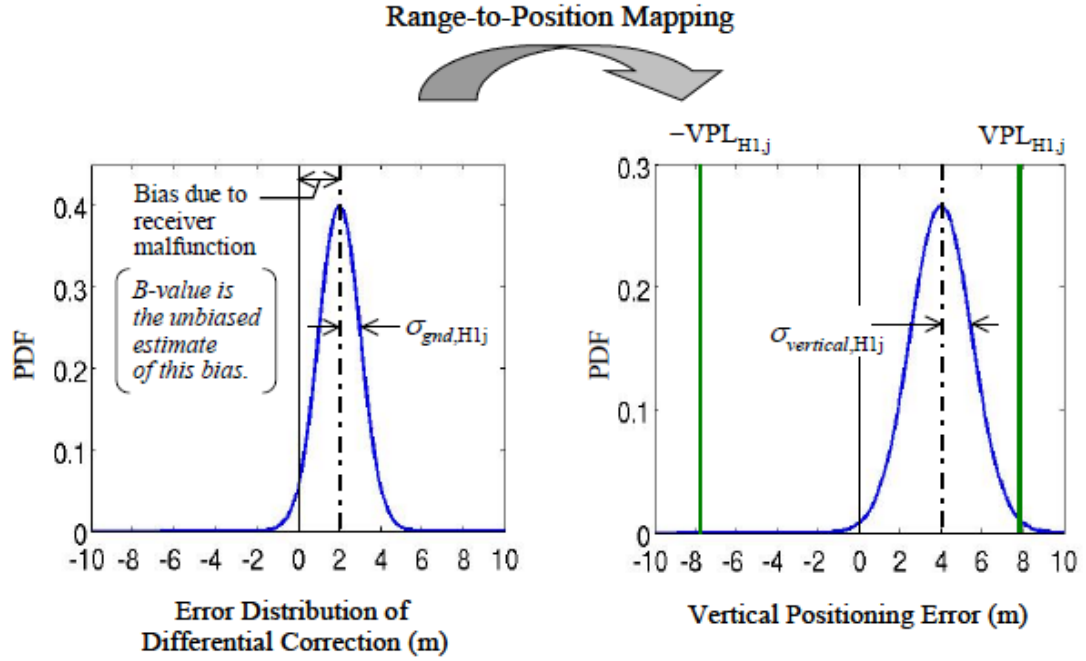


Figure 2.14. Biased-distribution due to single reference-receiver failure [Konno, 2007].

An approaching aircraft is required to compute vertical protection levels for ephemeris errors ($VPL_e$) if ephemeris error missed detection parameters are broadcast by the GBAS Ground Facility. $VPL_e$ values are computed for each satellite in a given geometry subset using the expression [Ramakrishnan, 2008]:

$$VPL_e[i] = |S_{vert,i}| x_{air} P[i] + \frac{K_{mde}}{K_{ffmd}} VPL_{H0} \qquad (2\text{-}47)$$

where

$S_{vert,i} \equiv$ elements of the weighted-least-squares propagation matrix $S$ corresponding to the vertical-axis components for satellite $i$;

$x_{air}$ : Separation between the GBAS Ground Facility and the current user aircraft location;

$K_{mde}$ : A broadcast multiplier derived from the probability of missed detection given that there is an ephemeris error on a GPS satellite;

$P[i]$ : Ephemeris Decorrelation Parameter broadcast for satellite $i$. This parameter gives users information regarding the Minimum Ephemeris Detectable Error (MEDE) that can be achieved by the ephemeris monitor. MEDE is the minimum satellite position error that can be detected by the monitor with a probability of missed detection consistent with the integrity risk allocated to ranging source (satellite) failures. Further details about the P-value and its significance can be found in [Pervan, 2005].

## 2.3.3 INTEGRITY METHODS FOR H$_2$ RISKS

Risk sources not covered by H$_0$ and H$_1$ conditions, namely H$_2$ risks, are generally taken care of by integrity monitoring algorithms implemented in the ground stations. GBAS research and design efforts have developed a number of ground-based integrity methods. Among them is the Signal Quality Monitor (SQM) that takes care of the GPS ranging signal anomaly known as "signal deformation" [Mitelman, 2004] [Phelts, 2000] [Pullen, Sep 2002] [Shively, 1999] [Zaugg, 2002] [Rife, 2006] [RTCA, 2004]. Signal deformation results from a failure of the signal-generating hardware onboard the GPS satellite and, if unmitigated, can induce unacceptably large measurement errors by significantly distorting the correlation function within the data tracking loop of the GPS receiver. To detect this anomalous signal behavior, SQM observes two types of metrics (*lambda test metric and rate test metric*) for each range measurement and compares them with a predetermined threshold derived based on a range-domain error bound called *Maximum-allowable ERror in Range* (MERR), which is somewhat analogous to the PL in the position domain [Mitelman, 2004] [Phelts, 2000], [Pullen, Sep 2002]. If an unacceptable deformation is detected in the signal from a particular satellite, the satellite is then flagged and its measurements are excluded from position estimation.

Data Quality Monitoring (DQM) methods and Measurement Quality Monitoring (MQM) methods are other examples. DQM methods verify the reliability of navigation data broadcast by GPS satellites [Pullen, 2001] [Pervan, 2005]. MQM methods detect sudden step errors and any other rapidly changing errors due to GPS clock anomalies and reference-receiver failures by verifying the consistency of both code and carrier measurements over the last few epochs [Xie, 2001]. Existing range-domain monitoring methods like those above completely mitigate almost all fault modes introduced in Section 2.3.1 (more specifically Figure 2.9). However, it is worth to emphasize again that no existing method can mitigate unacceptable errors induced by anomalous ionosphere behavior to the degree required for CAT IIIb GBAS.

# Chapter 3

# IMPACT AND MITIGATION OF ANOMALOUS IONOSPHERE ON GBAS

The ionosphere, extending from a height of about 50 kilometers to about 1300 kilometers above Earth, is a region of ionized gases (from electrons and ions). The ionization is caused by the Sun's radiation, and the state of the ionosphere is determined primarily by the intensity of solar activity. Solar flares and the resulting magnetic storms can create large and quickly varying electron densities, causing amplitude and phase scintillation, where the first causes signal fading and the second causes rapid phase fluctuations of GPS signals [Misra, 2006].

One of the residual errors that can build up for the user of a DGPS system like GBAS is the ionosphere spatial decorrelation error. This error is caused by the fact that two signals are passing through different regions of the atmosphere, and the resulting errors due ionospheric delays are not completely canceled out even after applying differential corrections. Such errors can grow during severe ionospheric storms and pose a threat to user integrity.

This chapter describes the procedure by which worst-case anomalous ionospheric spatial gradients are modeled, analyzed, and mitigated for GBAS including DCPS and airport surface movement.

# 3.1 SEVERE IONOSPHERE STORMS OBSERVED IN CONUS

Prior to 2002, it was believed that, during unusual ionospheric activity, ionospheric spatial gradients would not be more than 5-10 times greater than the value of 4 mm/km that was derived as a conservative one-sigma bound on nominal zenith ionospheric spatial gradients during "active" ionospheric conditions at solar maximum [Lee, 2007]. At the very worst, it was thought that known ionospheric anomalies, including ionospheric storms and the potential impacts of scintillation in equatorial and auroral regions, could not produce a spatial gradient larger than roughly 50-75 mm/km (e.g., see [Klobuchar, 1995]), which would not be a significant threat to GBAS users.

However, Datta-Barua *et al.* investigated ionosphere data of the northeastern quadrant of the United States on 6-7 April 2000 provided by the Wide Area Augmentation System (WAAS) and discovered an apparent ionosphere delay difference of 6 meters over a 19-kilometer separation, i.e., an ionospheric spatial gradient of about 320 mm/km, or almost 100 times larger than the nominal one-sigma, moving in a pattern similar to that of a

tropospheric weather front and with a varying propagation speed [Datta-Barua, 2002]. Gradients this large could not be bounded by any reasonable sigma value broadcast by a GBAS ground station, and they could generate vertical position errors significantly exceeding the 10-meter VAL, or safe error bound, for users flying GBAS-supported precision approaches to Category I weather minima [RTCA, 2004] [Pullen, 2009].

Several ionospheric storms of concern have occurred since the April 2000 storm that first alerted us to the potential hazard. Among them, the two largest ones were on October 29-30, 2003 and November 20, 2003. Figure 3.1 shows a snapshot of the ionosphere delay map over Conterminous United States (CONUS) on October 29, 2003 between 20:00 to 20:45 UT. The x-axis and y-axis represent longitude and latitude, respectively. The color scale indicates the magnitude of the vertical ionosphere delay [Luo, 2005]. Dark red represents about 20 meters of delay, and dark blue represents about 2 meters. As can be seen, there are some sharp transitions between the dark red and the blue, which indicates sharp spatial gradients in those areas. By comparing the subplots, it appears that the storm did not move much (relative to the continental scale shown) during the 45 minutes covered by these views. An ionosphere movie made to show that period with finer time resolution also indicates that the anomaly may have been "near stationary" at specific locations and times.
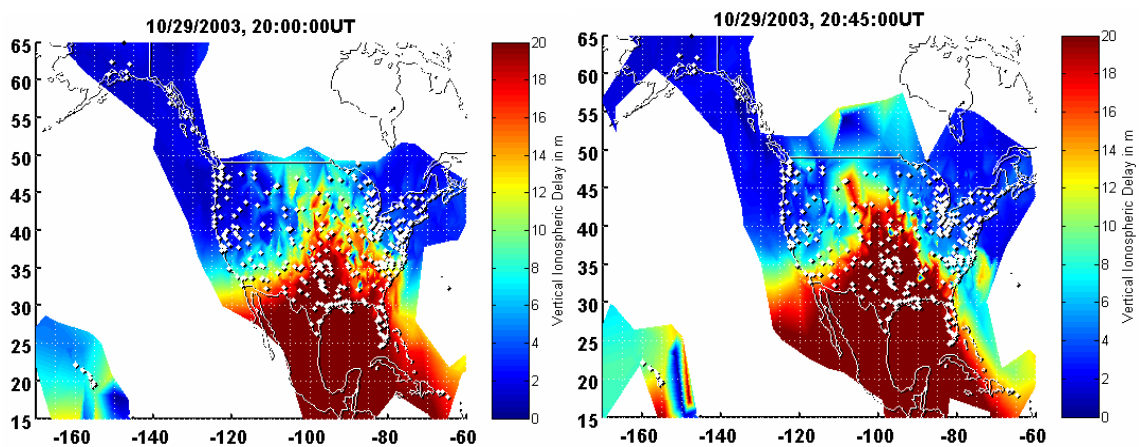


Figure 3.1. Ionosphere spatial anomalies observed during October 29, 2003 storm.

Figure 3.2 shows the November 20, 2003 storm in a similar fashion. This time, only the eastern half of the U.S. is shown. The large anomaly feature appears differently than what was seen previously (i.e., it has a distinctive "finger shape" in it), and it appears to move faster in general (roughly from East to West). However, additional sharp gradients between dark red and blue zones are observed [Luo, 2005].
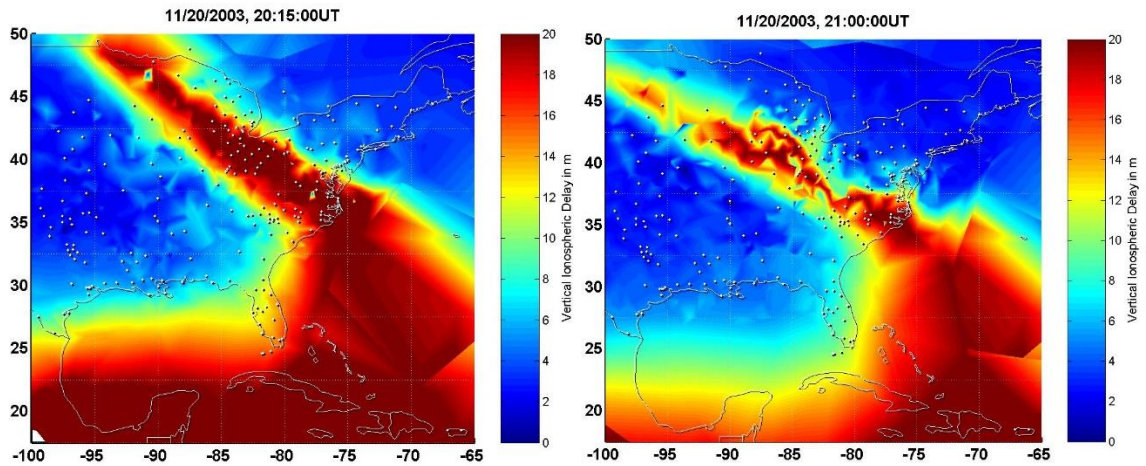


Figure 3.2. Ionosphere spatial anomalies observed during November 20, 2003 storm.

Figure 3.3 shows the slant ionospheric delay over time from this event as observed by seven receivers of Continuously Operating Reference Stations (CORS, a network of stations managed by the U.S. National Geodetic Survey to augment the local accuracy of GPS readings) tracking GPS SVN 38 in northern Ohio and southern Michigan, where the largest spatial gradients were observed [Ene, 2005]. The largest gradient corresponding to the sharp depletion among the seven stations shown in Figure 3.3 is about 330 mm/km, but another pair of CORS stations in northern Ohio (ZOB1 and GARF) observing GPS SVN 38 experienced a gradient of about 412 mm/km when the trailing edge passed.

The discovery of gradients of this magnitude during ionospheric storms (gradients far larger than ever seen from any other type of ionospheric behavior) was a major surprise to the GBAS and GBAS community and required the development of new mitigation

strategies. Such gradients could, under worst-case geometries between the GBAS Ground Facility, user aircraft, ionosphere gradient, and affected GPS satellites, create differential pseudorange errors as large as 8.5 meters without being observable to the monitoring algorithms in the GBAS Ground Facility (see Section 3.4). The hazard implied by this possibility to aircraft performing precision approaches to CAT I weather minima (with the 10-meter VAL mentioned earlier) was unacceptable without further mitigation within the GBAS Ground Facility [Pullen, 2009].
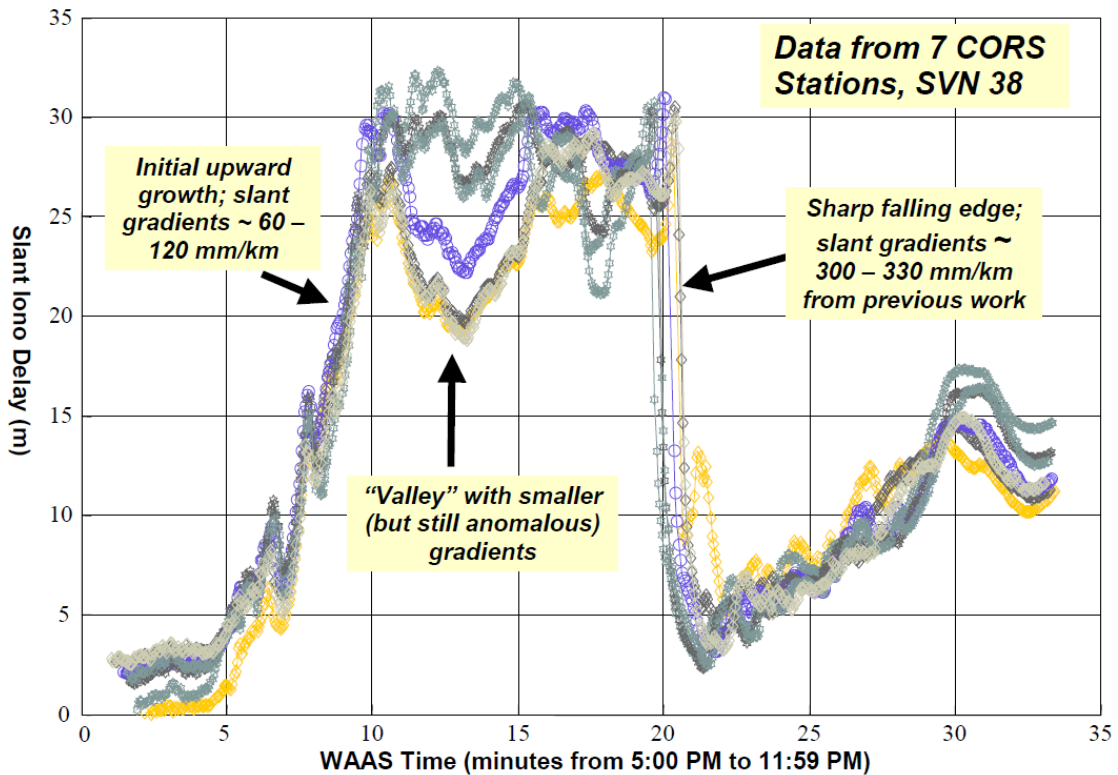


Figure 3.3. Ionosphere delays at seven CORS stations during 20 November 2003 ionospheric storm.

# 3.2 IONOSPHERIC STORM DATA ANALYSIS PROCEDURE

The largest gradients identified in Section 3.1 were the product of an exhaustive automated and manual analysis of all known ionospheric storm days in CONUS for which WAAS availability was affected (this would be due to the reaction of the WAAS ionospheric storm detector (see [Walter, 2000] [FAA, 2004])). The details of this method are described by Ene *et al.* [Ene, 2005]. The primary data source for this analysis is both raw and post-processed CORS reference station data from hundreds of stations throughout CONUS. Ionospheric spatial gradients are calculated automatically for all satellites tracked by ''clusters'' of CORS stations within close proximity (several tens of kilometers) of each other in regions known to be affected by ionospheric storms. All apparent gradients of large anomalous magnitude (e.g., above 200 mm/km), calculated by dividing the difference in slant ionospheric delay between two CORS stations by the distance between the two stations, are put through a series of automated screening algorithms. These algorithms attempt to eliminate the most common non-ionospheric causes of apparent large gradients, which are CORS receiver ''glitches'' and errors in the CORS data storage process [Ene, 2005]. The CORS network includes a variety of ''off-the-shelf'' dual-frequency receivers that are particularly vulnerable to codeless or semi-codeless tracking errors on L2 measurements during ionospheric anomalies, and these errors can make nominal or moderately anomalous gradients seem much larger than they really are. In fact, apparent ''gradients'' due to L2 cycle slips can be as large as several thousand mm/km, but practically all receiver-instigated events of this magnitude are removed by automated screening [Pullen, 2009].

While the automated screening algorithms described by Ene *et al*. [Ene, 2005] greatly reduce the set of large spatial gradient events that are output by the data analysis software, most of what remains is due to CORS receiver or data collection errors when manually

examined by researchers familiar with GPS receiver behavior. Therefore, all significant events output by the software were reviewed by a group of researchers who met regularly during the data analysis process to examine the software results and determine if a significant, verifiable ionosphere-created gradient was present. If so, the best manual estimate of the resulting gradient was computed and added to the list of ''valid'' anomalous ionosphere events. The key to the manual review process is a comparison between the apparent ionospheric gradient based on the post-processed dual-frequency measurements and those based on code-minus-carrier measurements from the raw, single-frequency (L1-only) CORS measurements for the same stations and satellites [Ene, 2005]. As noted above, most receiver ''glitches'' affect the semi-codeless L2 measurements, and while post-processing removes most of these errors, unusual measurement changes during ionospheric anomalies can introduce new errors. Large gradients reported by the data analysis software (based on post-processed L1–L2 ionospheric-delay estimates) were validated by comparison with gradient estimates computed from raw L1 code-minus-carrier measurements from the same CORS receivers [Pullen, 2009].

## 3.3 CONUS IONOSHERIC ANOMALY THREAT MODEL

On the basis of the largest validated ionospheric gradients reported in Section 3.2, Figure 3.4 and Figure 3.5 show the resulting ionospheric spatial-gradient threat model for CONUS [Ene, 2005] [Lee, 2006] [Ramakrishnan, 2008] [Pullen, 2009].

As described in [Luo, 2003], [Luo, Jan 2004], and [Luo, Sep 2004], ionosphere anomalies are modeled as linear wave fronts in order to study their impact on a GBAS user. Figure 3.4 illustrates this simplified model and an example of the ionosphere anomaly threat to GBAS. Four parameters are used to characterize the anomaly: gradient slope (in millimeters per kilometer), gradient width (in kilometers), front speed (in meters per

second), and maximum delay difference (in meters), which is simply the product of gradient slope and width. Upper bounds on each of these parameters have been determined based on the analysis of past storms described above. Note that the maximum delay difference is expressed as an upper bound in the model, as it constrains the slope and width values through their product (i.e., values of slope and width which are within their respective bounds but exceed the maximum-delay-difference bound when multiplied together are not a valid combination) [Ene, 2005] [Luo, 2005].
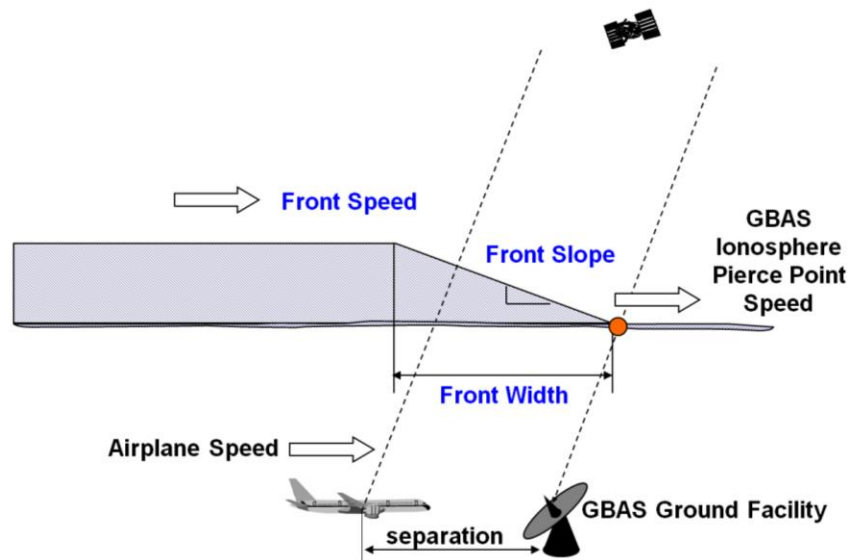


Figure 3.4. Simplified ionospheric wave front model: a wave front ramp defined by the "slope" and the "width" [Pullen, 2009].

As noted above, the parameters in the simplified model of ionosphere anomaly are estimated using data collected on ionospheric stormy days, and they can be summarized by an ionosphere anomaly "threat model." The current ionosphere anomaly threat model for CONUS (most recently revised in March 2007) is as shown in Figure 3.5, in which the maximum slant ionosphere gradient is 375 millimeters per kilometer for low elevation of satellite below 15 degrees and 425 millimeters per kilometer for high elevation above 65 degrees. In between, the maximum slant ionosphere gradient is a linear function of the

elevation angle of satellite (the bounds on speed, width, and maximum delay difference remain the same as the numbers given in [Lee, 2006]). The threat model is combined with GPS and airport geometry simulations to predict the maximum differential range and position errors that GBAS users might suffer. These are analyses of the particular satellite geometries for a given airport.
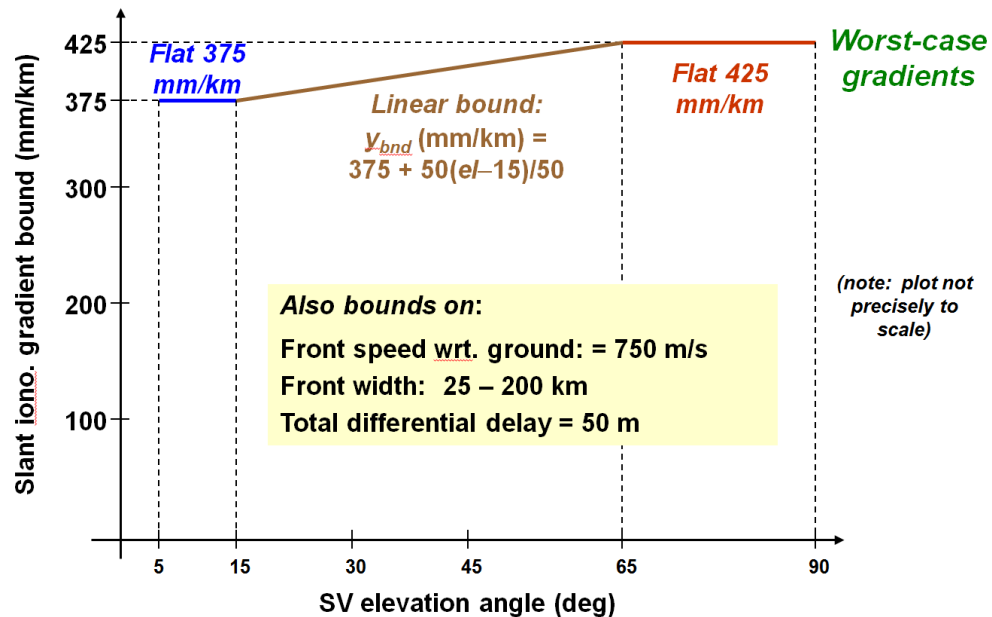


Figure 3.5. CAT-I anomalous ionospheric threat model based upon most severe anomalies observed in CONUS since 1999 [Pullen, 2009].

While the combination of worst-case events needed to generate errors of this magnitude would be extremely rare, given the fact that the ionosphere was known to be "stormy," this condition is deemed to be unsafe for CAT I precision approaches because the worst-case error magnitude exceeds an upper limit of 28.8 meters at the 200-foot DH for a CAT I approach (see [Shively, 2008] for the derivation of this limit). Given that the worst-case scenario is not guaranteed to be detected by a CAT I GBAS Ground Facility with the required missed detection probability ($P_{md}$), and knowing that CAT-I-equipped user aircraft are not required to monitor for abnormal ionospheric rates of change [RTCA,

2008], the only means to further mitigate this risk is in the position domain [Pullen, 2009], as described in the next section. Future systems can take advantage of the new signals at L5 and/or add ionospheric detection algorithms to the avionics [Konno, 2007].

# 3.4 MITIGATION VIA GROUND SYSTEM GEOMETRY SCREENING

GBAS Ground Facility real time geometry screening has been developed to mitigate ionosphere anomaly threat for GBAS CAT I precision approach. The algorithm in [Lee, 2006] inflates the sigma values ($\sigma_{vig}$ and $\sigma_{pr\_gnd}$) broadcast by the GBAS Ground Facility. This ensures that subset satellite geometries for which unacceptable errors can result are made unavailable to the user. These unsafe subsets are found by comparing the resulting Maximum Ionosphere-induced Error in Vertical (MIEV) with the maximum "safe" Navigation System Error (NSE) values derived from Obstacle Clearance Surface (OCS) applicable to CAT I precision approaches. This is where the limit of 28.8 meters mentioned above comes from. Another algorithm in [Ramakrishnan, 2008] implements GBAS Ground Facility real time geometry screening by inflating satellite-specific, targeted ephemeris decorrelation parameters (called "P-values") and $\sigma_{pr\_gnd}$ values. These algorithms are briefly illustrated in the flow chart in Figure 3.6. From the satellite almanac, airborne subset geometries are determined, and the worst-case ionosphere error over all subset geometries and anomalous ionospheric conditions is determined from the ionospheric anomaly threat model. Then, approach hazard assessment is applied and if unsafe subsets exist, the algorithm inflates the sigma and P-value parameters iteratively until all unsafe subsets are made unavailable (because their inflated VPLs exceed VAL). Finally, approved sigma values and P-values for broadcast by VDB are obtained. [Lee, 2006] and [Ramakrishnan, 2008] demonstrate that geometry screening in GBAS can fully mitigate the CONUS ionosphere spatial decorrelation threat model.

While sigma and/or P-value inflation is required to eliminate ''unsafe'' geometries, it has the unavoidable impact of making ''safe'' geometries unavailable as well. Furthermore, the inflation required to protect the most demanding approach (typically the one furthest from the GBAS Ground Facility) exceeds what is required for all other GBAS-supported approaches at that airport. As a result, the achievable CAT I system availability with geometry screening included is significantly lower than what it would be if geometry screening were not required. However, most major airport locations in CONUS will still achieve CAT I availabilities of 0.999 or better when all 24 GPS satellites in primary orbit slots are healthy [Pullen, 2009].
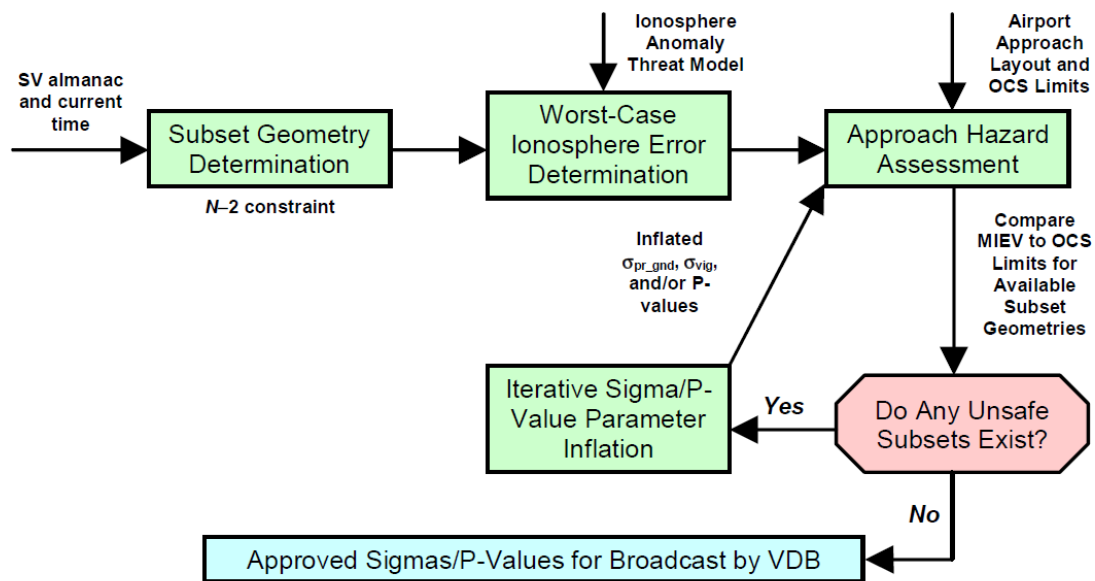


Figure 3.6. GBAS ground system geometry screening methodology flow diagram.

# Chapter 4

# ENABLING SURFACE MOVEMENT UNDER IONOSPHERIC ANOMALIES

The Ground Based Augmentation System (GBAS) can be used for both Category I (CAT I) precision approach and Differentially Corrected Positioning Service (DCPS) navigation applications. GBAS Ground Facilities that support DCPS are required to help meet the integrity requirements of terminal-area navigation and other operations that could use the GBAS VHF Data Broadcast in addition to precision approach. The current GBAS standards indicate that DCPS integrity risk shall not exceed $10^{-7}$ per hour [FAA, 2002] [RTCA, 2004]. This requirement is hard to achieve under severe conditions such as anomalous ionosphere, which has been observed over CONUS since 2000 (see Chapter 3).

The Position/Velocity/Timing (PVT) outputs should be "de-linked" from DCPS so that they can be used independently. PVT applications that cannot be supported by DCPS should be defined as separate applications of GBAS in the same manner as precision approach. Appendix A identifies the changes that are required and recommends specific sets of alternatives for DCPS. One of its conclusions is that some future applications of GBAS that planned to use DCPS, such as airport surface movement, cannot be supported by DCPS with the CAT-I GBAS architecture because DCPS cannot meet current integrity requirements. It suggests one important further change to the GBAS avionics requirements. The current LAAS Minimum Operational Performance Standards (MOPS) forbids use of the GBAS PVT outputs if DCPS is not enabled by the GBAS Ground Facility [RTCA, 2008]. As Appendix A points out, GBAS will not support all applications that can make use of the PVT outputs.

The original hypothesis was that, if airport surface movement is defined as a separate operation, it would be supported by the existing GBAS Ground Facility geometry screening that mitigates the anomalous ionospheric threat for CAT I precision approach. The primary adjustment needed would be to increase the aircraft $\sigma_{pr\_air}$ value if needed to bound the higher multipath errors expected in the airport surface environment (as opposed to an aircraft in flight). Confirming this hypothesis required a more-intensive study of the requirements on airport surface movement and is the subject of this chapter. Since GBAS Ground Facility geometry screening itself cannot support airport surface movement, the results in this chapter include additional aircraft geometry screening as proposed in Appendix A to lower the Maximum Acceptable Error (MAE). Since it is not clear what level of MAE is needed for a given airport-surface operation, our goal is to minimize the achievable MAE (and thus Horizontal Alert Limit, or HAL) while maintaining useful availability.

# 4.1 SURFACE MOVEMENT: DEFINITION AND REQUIREMENTS

Airport surface movement is aircraft movement on the airport ground, such as on taxiways. Typical surface movements are taxi and pullback, but it includes all movements of aircraft on the airport ground from the gate to the runway before takeoff, as shown in Figure 4.1, or from the runway to the gate after landing.

What are appropriate physical requirements specific to surface movement? When an airplane lands, we want to be able to provide surface movement guidance and surveillance all the way to the point of termination, the gate. Conversely, when an airplane pulls back from the gate, we want to be able to provide surface movement guidance and surveillance all the way to the runway. Aircraft need to turn during surface movement because taxiways are often curved, as shown in Figure 4.2. Operation in poor weather makes the requirements tighter. Airport surface movement can generally be classified by two types of applications, GBAS-guided application and surveillance application. A GBAS-guided application is used to guide aircraft from runway to the gate or vice versa. Surveillance application is used to detect and display the position of aircraft in the terminal area. When all these are considered, error bounds of 10 meters for guidance is recommended. A looser error bound of 20 meters for surveillance should be acceptable because this is the width of airport taxiways.

The results in Appendix B show that surface movement cannot meet the same requirements as those of DCPS supporting terminal area operations because the acceptable error of surface movement is much tighter than terminal area operations (See Section B.4.2). Surface movement thus needs to be defined as a separate operation of GBAS (meaning separate from DCPS) with its own requirements. These requirements can be used to

establish a separate operation with its own protection level. Parameter inflation can be targeted to this specific application.



Figure 4.1. Airport surface movements: from gate to runway [www.dailymail.co.uk].



Figure 4.2. Airplane traffic on taxiways [www.dreamtime.com].

# 4.2 SIMULATION PROCEDURE

## 4.2.1 SIMULATION OF HPE AND HPL FOR AIRPORT SURFACE MOVEMENT

In order to represent airport surface movement, the simulation procedure used to obtain Horizontal Position Errors (HPEs) and the corresponding Horizontal Protection Levels (HPLs) for DCPS is shown in Figure 4.3. One day of geometries with five-minute time updates and a five-degree visibility mask angle at Memphis International Airport (MEM) is used to generate all-in-view, all one-satellite-out ($N$–1), all two-satellite-out ($N$–2), etc., down to all four-satellite subset geometries. The variable $N$ represents the number of visible satellites in the geometry (which are all assumed to be approved for use by the GBAS Ground Facility). The maximum supported distance from GBAS Ground Facility to user, defined as $D_{max}$ and included in the information broadcast by the VDB [RTCA, 2008] [ICAO, 2006], is set by the service provider. A typical value for $D_{max}$ is 45 kilometers (the maximum coverage of the VDB at approach altitude), and GBAS Ground Facility-to-user separations of 0 to 6 kilometers are used for the simulation of airport surface movement. In this chapter, for airport surface movement, a speed of 10 m/s (about 19.4 knots, or 22.4 mph) is used because it is a typical aircraft velocity at a distance of 6 km from an airport, although the actual speed could be different according to the particular airport surface movement operation being conducted.

Generate all in view, all 1-SV out, all 2-SV out, …, down to all 4-SV subset geometries

- 1 day (24 hours)
- 5-minute updates
- 24-SV constellation (All SV's healthy)
- 11 major U.S. airports

**1-SV impact**

Loop through all independent individual satellites

$D = 0 \sim 6$ km
$V_{aircraft} = 10$ m/s

CONUS CAT-I Ionospheric Anomaly Threat Model [12]

Iono. Slope (mm/km)

425

375

*Plot not precisely to scale*

15    65

Elevation (degree)

Compute worst-case Horizontal Position Error (HPE)

$V_{aircraft} = 10$ m/s, **LGF real-time inflated $\sigma_{vig}$ or 6.4 mm/km**

Constant $\sigma_{pr\_air}$ Inflation: $1\,\sigma_{pr\_air} \sim 4\,\sigma_{pr\_air}$

Compute Corresponding Horizontal Protection Level (HPL)

Figure 4.3. Airport surface movement simulation procedure to generate worst-case errors under ionospheric anomalies.

### 4.2.1.1   Ionospheric Range Error

Worst-case GPS range errors from the anomalous ionospheric threat model for CONUS [Pullen, 2009] are applied to all individual satellites in all allowed subset geometries, one satellite at a time. Anomalous ionospheric range errors applied to individual satellites are basically proportional to the distance from GBAS Ground Facility to user with the addition of a bias due to an assumed aircraft velocity in the direction of the ground facility, but they might be reduced by GBAS Ground Facility Code-Carrier Divergence (CCD) monitoring, and then applied to an individual or any pair of satellites. Ionospheric range errors modeled

in equation (2-38) can be approximated by closed-form equations based upon the parameters from the ionospheric anomaly threat model for CONUS.

These expressions, whose key parameter is the ionosphere front velocity, are modified from [Ramakrishnan, 2008]. The GBAS Ground Facility uses a CCD monitor to detect anomalous ionospheric activity [Simili, 2006]. However, for this monitor to detect hazardous spatial gradients, the relative velocity ($\Delta v$ (km/s)) between two GBAS Ground Facility Ionosphere Pierce Point (IPP) velocities projected onto the direction of the ionosphere front velocity must be significantly non-zero. For smaller relative velocities, the CCD monitor does not alert, and the resulting undetected user errors can be large (albeit very rare).

The closed-form range error models used in this simulation can be summarized as follows [Murphy, 2010]:

*Slow Ionosphere Front Speed:*

$$\Delta v \ < \ \frac{0.0229 \ (\text{m/s})}{\min\left[\dfrac{50 \ (\text{m})}{W}, G\right]}, \quad \Delta v \ < \ 0.11 \ (\text{km/s})$$

(4-1)

There is no CCD detection in these cases. The error ($\varepsilon$ (m)) induced by the ionosphere is proportional to the separation between the GBAS Ground Facility and the approaching aircraft. This relationship is expressed as:

$$\varepsilon = \min\left[\frac{50 \ (\text{m})}{W}, G\right] \times \left(x + 2\tau v_{aircraft}\right)$$

(4-2)

where,

*W*:     Width of the ionosphere front (km);

G: Gradient or "slope" of the ionosphere front through which the IPP passes through (m/km);

τ: 100-second smoothing time of the Carrier-Smoothing filter used by GBAS (s);

$v_{aircraft}$: Velocity of the user aircraft during its final approach segment (assumed to be a constant 0.010 km/s in this and next chapter) (km/s);

x: Distance between the GBAS Ground Facility and the user (conservatively assumed to be 6 km in this chapter) (km).

**Moderate Ionosphere Front Speed:**

$$\frac{0.0229 \,(\text{m/s})}{\min\left[\dfrac{50\,(\text{m})}{W}, G\right]} < \Delta v < 0.11 \,(\text{km/s})$$

$$(4\text{-}3)$$

In these cases, the CCD monitor alerts for some conditions within this range of relative speeds. Consequently, the errors that users could suffer begin to decrease. Under the CONUS threat model, the maximum differential range error the user would suffer is no greater than 4 meters.

**Fast Ionosphere Front Speed:**

$$\Delta v > 0.11 \,(\text{km/s})$$

$$(4\text{-}4)$$

In these cases, The CCD monitor alerts with a very small missed-detection probability. Under the CONUS threat model, the maximum range error that users could potentially suffer is no greater than 2.5 meters.

The applied ionospheric range errors are all positive as expressed before and are actually the magnitude of actual errors. This is not a problem for zero-SV or one-SV impact model, but it may miss the worst-case error for the two-SV impact model. To take care of this, three possible combinations of range errors of satellites $k_1$ and $k_2$ are considered as below.

The factor 0.5 (instead of 1) is chosen to reduce the over-conservatism of maximum ionosphere induced horizontal error for the worst-case ionospheric front affecting two satellites because a single front must have the same "polarity," or direction of ionospheric delay change, for both satellites. In other words, it is to eliminate the two "positive/negative" cases in equation (6-6) and (6-7) but to include the "negative/negative" case along with the "positive/positive" case. The factor of 0.5 is also selected to bound the "two-front" event observed on November 20, 2003.

$$IEH_{k1,k2,1} = |S_{horizontal,k1}\ \varepsilon_{k1,positive} + S_{horizontal,k2}\ \varepsilon_{k2,positive}| \qquad (4\text{-}5)$$

$$IEH_{k1,k2,2} = |S_{horizontal,k1}\ \varepsilon_{k1,positive} + 0.5 S_{horizontal,k2}\ \varepsilon_{k2,negative}| \qquad (4\text{-}6)$$

$$IEH_{k1,k2,3} = |0.5 S_{horizontal,k1}\ \varepsilon_{k1,positive} + S_{horizontal,k2}\ \varepsilon_{k2,negative}| \qquad (4\text{-}7)$$

where $S_{horizontal}\ \varepsilon$ is root-sum-square (RSS) of $S_{horizontal,1}\ \varepsilon$ and $S_{horizontal,2}\ \varepsilon$. Here, $S_{horizontal,1}$ and $S_{horizontal,2}$ are the rows of the weighted-least-squares projection matrix corresponding to the horizontal position component [RTCA, 2008]. The largest of these three vertical errors is the worst-case Ionosphere-induced-Error-in-Horizontal (IEH).

### 4.2.1.2   HPL – Standard Deviation and Parameters

The nominal ionospheric gradient parameter, the standard deviation of the vertical ionosphere gradient or $\sigma_{vig}$, may vary due to the GBAS Ground Facility geometry screening needed to protect CAT-I precision approach, which is briefly described in the next section. Here, the nominal (uninflated) $\sigma_{vig}$ of 6.4 millimeters per kilometer, which includes a contribution to bound anomalous tropospheric error, is used to compute both HPE and the uninflated HPL, and a specific value of inflated $\sigma_{vig}$ for each epoch obtained by the real-time sigma-inflation algorithm used for precision approach is used to compute the HPL.

The standard deviation of the aircraft contribution to the total pseudorange error, $\sigma_{pr\_air}$, includes aircraft receiver noise and a standard allowance for airframe multipath. (Airport-surface multipath is considered in Chapter 5.) The performance of the airborne subsystem

is defined in terms of Airborne Accuracy Designators (AAD). Currently two AAD (A and B) are defined and empirical expressions described in Section 2.2.3 are used. In these simulations, the more conservative model (AAD A) is used for computing errors and uninflated HPL, while AAD B is used for computing inflated HPL at an aircraft. For both of them, the equation for Airframe Multipath Designator (AMD) A defined in [RTCA, 2004] is used for the aircraft $\sigma_{multipath}$ and it is shown in Equation (2-35) in Section 2.2.3. A broadcast multiplier (unitless) for computation of the ephemeris error position bound for the GBAS positioning service, $K_{md\_e\_POS\_hrz}$, of 5.085, and an ephemeris decorrelation parameter, or "P-value" ($P_k$), of 0.00018 meters per meter, are used [RTCA, 2008] [ICAO, 2006]. HPE comes from the simulation and the range error model given above, and HPL is computed as described in [RTCA, 2008] [ICAO, 2006] and shown below. The largest HPE and corresponding HPL are stored for each subset geometry generated by the satellite geometry simulation described above.

$$HPL = \max\{HPL_{H0}, HPL_{H1}, HPB_e\} \tag{4-8}$$

The horizontal position level under $H_0$ is

$$HPL_{H0} = 10 d_{major} \tag{4-9}$$

where

$$d_{major} = \sqrt{\frac{d_x^2 + d_y^2}{2} + \sqrt{\left(\frac{d_x^2 - d_y^2}{2}\right)^2 + d_{xy}^2}} \tag{4-10}$$

$d_x^2 = \sum_{i=1}^{N} S_{1,i}^2 \sigma_i^2$ = variance of model distribution that overbounds the true error distribution in the "1" axis

$d_y^2 = \sum_{i=1}^{N} S_{2,i}^2 \sigma_i^2$ = variance of model distribution that overbounds the true error distribution in the "2" axis

$d_{xy} = \sum_{i=1}^{N} S_{1,i} S_{2,i} \sigma_i^2 =$ covariance of the model distribution in the "1" and "2" axes

$\sigma_i \equiv$ weightings used in the least squares solution

$S_{0,0} \equiv$ elements of the weighted least squares projection matrix $\mathbf{S}$ used in the generation of the position for the PVT output

The protection levels under the $H_1$ hypothesis are

$$HPL_{H1} = max[HPL_{H1}[j]] \tag{4-11}$$

where $HPL_{H1}[j]$ for all j (1 to MAX{M[i]}) as follows,

$$HPL_{H1}[j] = |B_{j\_H}| + K_{md\_POS\_hrz} d_{major\_H1} \tag{4-12}$$

$$d_{major\_H1} = \sqrt{\frac{d\_H1_x^2 + d\_H1_y^2}{2} + \sqrt{\left(\frac{d\_H1_x^2 - d\_H1_y^2}{2}\right)^2 + d\_H1_{xy}^2}} \tag{4-13}$$

$d\_H1_x^2 = \sum_{i=1}^{N} s_{1,i}^2 \sigma_{i\_H1}^2 =$ variance of model distribution that overbounds the true error distribution in the "1" axis

$d\_H1_x^2 = \sum_{i=1}^{N} s_{1,i} s_{2,i} \sigma_{i\_H1}^2 =$ variance of model distribution that overbounds the true error distribution in the "2" axis

$$\sigma_{i\_H1}^2 \equiv \left(\frac{M[i]}{U[i]}\right) \sigma_{pr\_gnd\_x}^2[i] + \sigma_{tropo}^2[i] + \sigma_{pr\_air}^2[i] + \sigma_{iono}^2[i] \tag{4-14}$$

The computation of $\sigma_{i\_H1}$ depends on the active Approach Service Type. See section 2.3.11.5.2.4 of [RTCA, 2008].

$M[i]$ = number of ground subsystem reference receivers whose pseudorange measurement was used to determine the differential correction for the ith ranging source used in the position solution.

$U[i]$ = number of ground subsystem reference receivers whose pseudorange measurements were used to determine the differential correction for the ith ranging source used in the navigation solution, not counting the jth reference receiver.

$K_{md\_POS\_hrz} \equiv 5.3$ (unitless)

$B[i,j]$ = the B value (in meters) for the ith ranging source and j[th] reference receiver as indicated in the Type 1 Message

The ephemeris error position bound is given by

$$HPB_e = max(HPB_e[k]) \qquad (4\text{-}15)$$

where

$P_k$ = ephemeris decorrelation parameter for ranging source k broadcast in the Type 1 message

$x_{air}$ = distance (slant range) between the aircraft and the GBAS reference point (in meters)

$HPB_e[k]$ is the horizontal ephemeris error position bound for the kth GPS ranging source used in the position solution, where $HPB_e[k]$ is computed for all GPS ranging sources used in the position solution:

$$HPB_e[k] = |s_{hrz,k}|x_{air}P_k + K_{md\_e\_POS\_hrz}d_{major} \qquad (4\text{-}16)$$

$K_{md\_e\_POS\_hrz} = K_{md\_e\_POS}$ = the broadcast multiplier for computation of the ephemeris error position bound for the GBAS positioning service derived from the probability of missed detection given that there is an ephemeris error in a GPS satellite (unitless)

## 4.2.2 REAL-TIME $\Sigma_{\text{VIG}}$-INFLATION SIMULATION FOR PRECISION APPROACH

The simulation used to establish real-time inflation factors for $\sigma_{\text{vig}}$ to protect CAT-I precision approach is based on the methodology in [Lee, 2006] and is modified to fit the current CAT-I GBAS operational design. Subset geometries are generated for CAT I in the same manner as described in Section 4.2.1 (drill-down to four satellites). In addition, geometries whose inflated Vertical Protection Levels (VPLs) are above the CAT-I Vertical Alert Limit (VAL) of 10 meters are "screened out" (i.e., made unavailable for use in the simulation). The assumed distance from GBAS Ground Facility to user at the 200-ft CAT-I decision height is set to be 6 kilometers [Lee, 2006].

The worst-case ionospheric impact for precision approach must be evaluated over all independent pairs of satellites in each subset geometry. Ionosphere-induced range errors for CAT I are determined by closed-form equations based upon the parameters from the ionospheric anomaly threat model for CONUS, as shown in Subsection 4.2.1.1.

The broadcast multiplier (unitless) for computation of the ephemeris error position bound for Category I precision approach, $K_{md\_e\_CAT1}$, of 5.085, and the same $P_k$ of 0.00018 m/m, are used to get Ionosphere-induced-Error-in-Vertical (IEV), VPL, and required inflation factors for $\sigma_{\text{vig}}$ [Lee, 2006] as needed. Note that the multiplier (unitless) which determines the probability of missed detection, $K_{md}$, of zero is used in IEV because IEV only includes the impact of ionospheric anomalies. The applied ionospheric range errors are all positive as expressed before and are the magnitude of actual errors. To take care of these errors, three possible combinations of range errors of satellites $k_1$ and $k_2$ are considered as below.

These equations are analogous to the ones used for horizontal error (equations (4-5) through (4-7)).

$$IEV_{k1,k2,1} = |S_{vertical,k1}\, \varepsilon_{k1,positive} + S_{vertical,k2}\, \varepsilon_{k2,positive}| \qquad (4\text{-}17)$$

$$IEV_{k1,k2,2} = |S_{vertical,k1}\, \varepsilon_{k1,positive} + 0.5 S_{vertical,k2}\, \varepsilon_{k2,negative}| \qquad (4\text{-}18)$$

$$IEV_{k1,k2,3} = |0.5 S_{vertical,k1}\, \varepsilon_{k1,positive} + S_{vertical,k2}\, \varepsilon_{k2,negative}| \qquad (4\text{-}19)$$

where $S_{vertical}$ is the row of the weighted-least-squares projection matrix corresponding to the vertical position component [RTCA, 2008]. The largest of these three vertical errors is the worst-case IEV. Figure 4.4 shows the Maximum-Ionosphere-induced-Error-in-Vertical (MIEV) per epoch for an example simulation at Memphis (prior to sigma inflation). The lack of inflation is what causes MIEV to exceed the tolerable error limit in this figure for some epochs.

In order to ensure that VAL bounds MIEV for all usable "subset" geometries, real-time sigma inflation beyond the nominal sigma value of 6.4 mm/km is performed when needed using the pre-computed and stored values of IEV and VPL for CAT-I precision approach. This simulation procedure is based on Fig. 10 and Fig. 11 in [Lee, 2006]. A single epoch is considered as an example to illustrate the concept of $\sigma_{vig}$ inflation. If IEV for a particular subset geometry is above the tolerable error limit (28.78 m) derived from the Obstacle Clearance Surface (OCS) at the CAT-I decision height (DH) [Shively, 2008], $\sigma_{vig}$ is increased until the VPL for that geometry (based upon the inflated $\sigma_{vig}$) is above VAL; thus that problematic geometry will be screened out (made unavailable) by the VPL check at the aircraft. This sigma-inflation procedure is repeated until all subset geometries with IEV exceeding 28.78 m are made unusable, meaning that the "maximum IEV" (MIEV) of the remaining "usable" geometries is no greater than 28.78 m at the DH. The resulting value of $\sigma_{vig}$ per epoch, as shown in Figure 4.5, is fed into the airport surface movement simulation to compute inflated HPL for users not conducting CAT-I precision approaches.
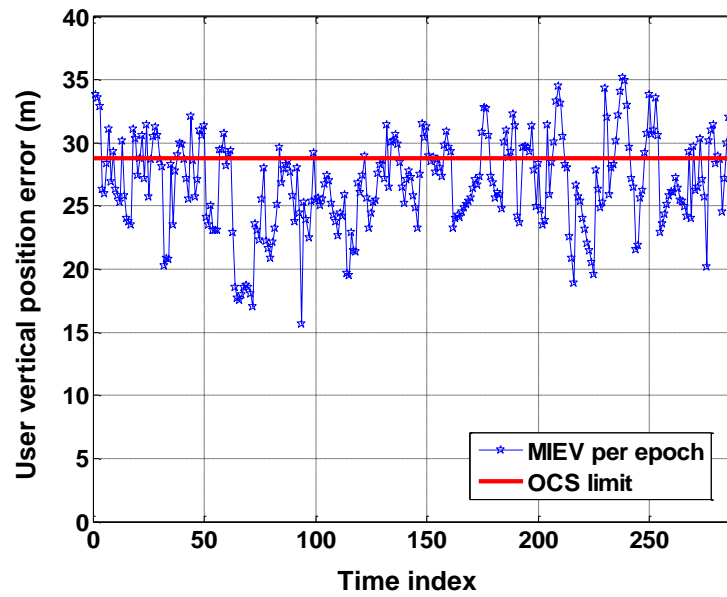
Figure 4.4 MIEV simulation results of all the subset geometries for precision approach at Memphis using RTCA 24-SV GPS constellation (prior to inflation).
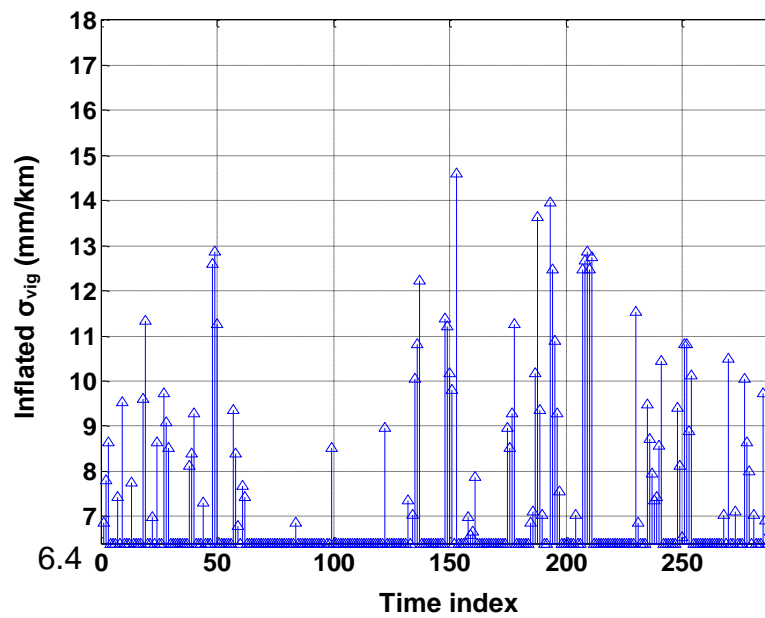


Figure 4.5 Real-time inflated $\sigma_{vig}$ for precision approach at Memphis.

# 4.3 GBAS GROUND FACILITY SIGMA INFLATION

Since airport surface movement is operated near GBAS Ground Facility and an aircraft moves with slow speed, anomalous ionospheric errors are smaller than the errors in other operations of DCPS. If airport surface movement is defined as a separate operation from DCPS, it might be supported by the existing GBAS Ground Facility geometry screening implemented to protect the CAT I precision-approach operation. Airport surface movement can take advantage of using the same $\sigma_{vig}$ values inflated for precision approach.

Since an aircraft in airport surface movement is on the ground, it suffers from higher multipath errors than while in flight, as additional signal reflections come from the ground, other aircraft or vehicles, and nearby buildings. In addition to real-time GBAS Ground Facility $\sigma_{vig}$ inflation, a larger value of $\sigma_{pr\_air}$ inflation is likely needed to bound these higher multipath errors during airport surface environment. In this chapter, the application of higher values of $\sigma_{pr\_air}$ takes the form of "inflation" of the existing $\sigma_{pr\_air}$ model by a constant multiplier. Since the degree of $\sigma_{pr\_air}$ inflation required is not yet known, several multiplier values are investigated.

## 4.3.1 IMPACT OF GBAS GROUND FACILITY SIGMA ($\Sigma_{VIG}$, $\Sigma_{PR\_AIR}$) INFLATION

For simulation of GBAS-guided surface movement in this chapter, all subset geometries down to four satellites are considered, and HPE expresses the worst-case ionospheric error only. As with the precision approach IEV, no nominal error contribution (including the projected nominal impact of multipath in the airport surface environment) is added to it.

Figure 4.6 shows the impact of GBAS Ground Facility $\sigma_{vig}$ inflation on HPL for a GBAS Ground Facility-to-user separation of 6 kilometers. While HPL in Figure 4.6(a) is

computed using a fixed, uninflated $\sigma_{vig}$ value of 6.4 millimeters per kilometer, HPL in Figure 4.6(b) is computed using the inflated $\sigma_{vig}$ values shown in Figure 4.5 (based on meeting CAT I precision approach requirements). Some geometries unprotected by HPL in Figure 4.6(a) and thus represented by red dots become protected geometries (HPL $\geq$ HPE) denoted by green dots in Figure 4.6(b).
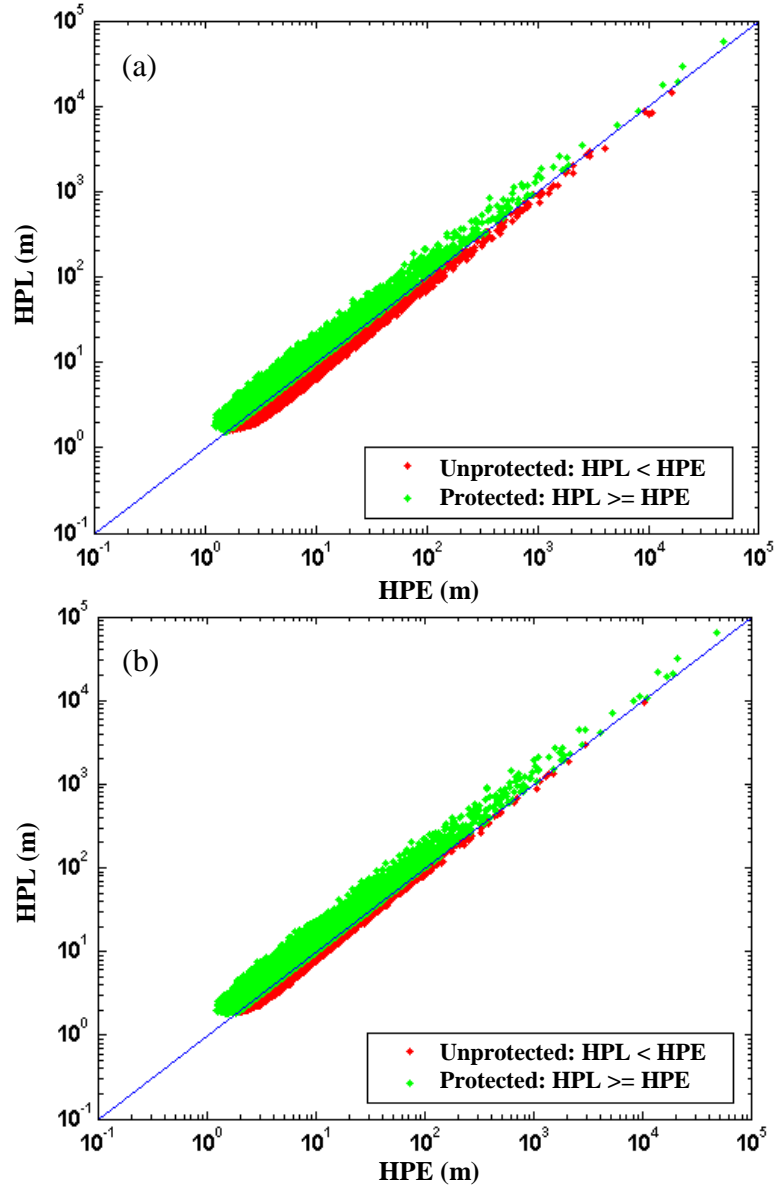


Figure 4.6. Impact of GBAS Ground Facility $\sigma_{vig}$ inflation on HPL: (a) no inflation of $\sigma_{vig}$ and $\sigma_{pr\_air}$; (b) inflation of $\sigma_{vig}$ and no inflation of $\sigma_{pr\_air}$.

The sensitivity of HPL to constant aircraft $\sigma_{pr\_air}$ inflation (to bound larger multipath errors) is demonstrated in the change from Figure 4.6(b) to Figure 4.7. HPL in Figure 4.7 is computed using a constant $\sigma_{pr\_air}$ value inflated by factor of two (in an attempt to cover surface multipath) in addition to the GBAS Ground Facility-inflated $\sigma_{vig}$ values. All geometries left unprotected in Figure 4.6(b) and thus represented by red dots are moved to the green-dot protected region in Figure 4.7.

To clarify which surface-movement scenarios are protected by HPL bounding, maximum values of the HPE-to-HPL ratio for different combinations of $\sigma_{vig}$ and $\sigma_{pr\_air}$ for GBAS Ground Facility-to-user separations of 0 to 6 kilometers are shown in Figure 4.8. The blue triangles represent the scenario of no inflation in either $\sigma_{vig}$ or $\sigma_{pr\_air}$. The green circles represent the scenario of inflated $\sigma_{vig}$ and no inflation of $\sigma_{pr\_air}$, the red triangles represent no inflation of $\sigma_{vig}$ and $\sigma_{pr\_air}$ inflated by a factor of two, and the cyan circles represent inflated $\sigma_{vig}$ and $\sigma_{pr\_air}$ inflated by a factor of two. Note that the HPE values for the scenario of inflated $\sigma_{vig}$ and $\sigma_{pr\_air}$ inflated by a factor of two, as shown by the cyan line, are bounded by their corresponding HPLs. In other words, the HPE-to-HPL ratio always exceeds 1.0. This indicates that the airport surface movement integrity requirements can be met (for any definition of MAE or HAL) by CAT I GBAS using the current approach to GBAS Ground Facility geometry screening and a doubling of $\sigma_{pr\_air}$. From now on, real-time GBAS Ground Facility $\sigma_{vig}$ inflation is used in every simulation unless specified since it is required in today's GBAS and, as expected, it makes the surface-movement integrity requirement easier to meet.
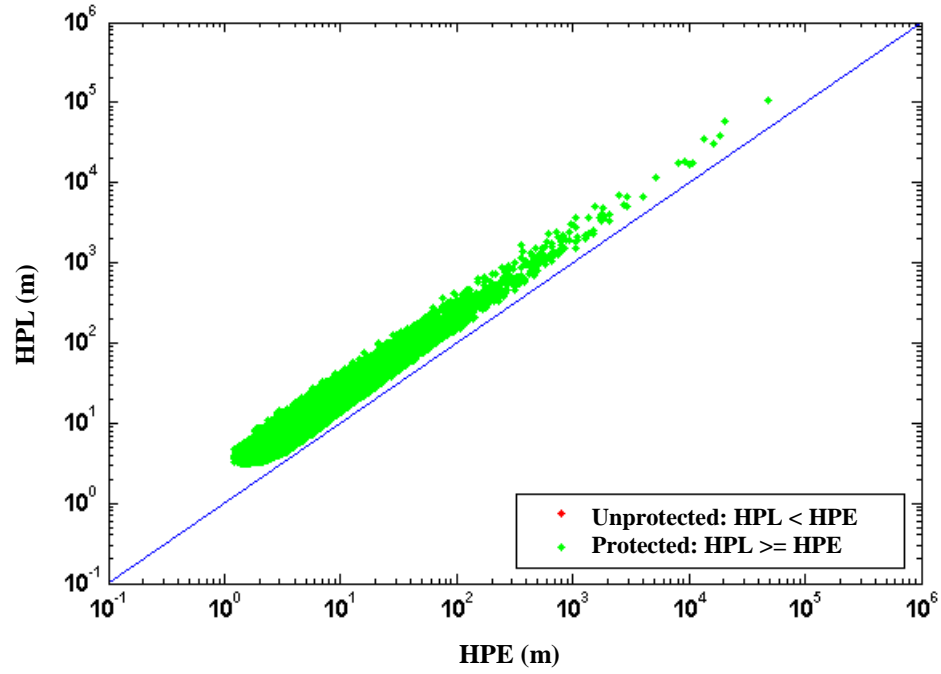
Figure 4.7. Impact of aircraft $\sigma_{pr\_air}$ inflation on HPL: inflated $\sigma_{vig}$ and 2 $\sigma_{pr\_air}$.
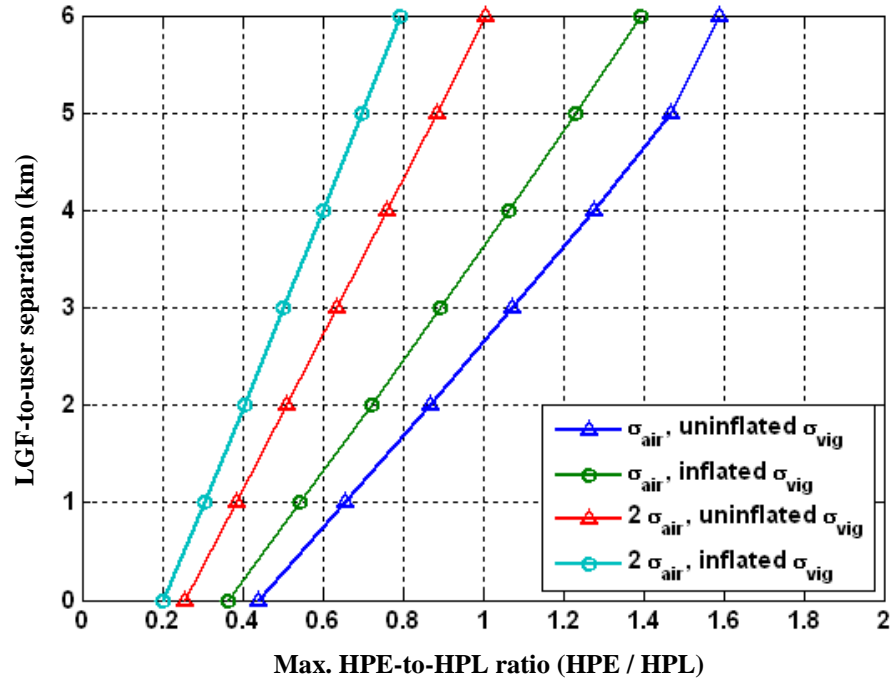


Figure 4.8. Inflation scenarios protected by HPL bounding.

## 4.3.2 AVAILABILITY COMPUTATION

Availability is calculated from two different types of geometry sets in this chapter. One is a set of all-in-view geometries only, and the other is a set of all-in-view geometries plus subset geometries with one satellite missing – these will be called "drill-down to one satellite out" geometries or "$N-1$ geometries" from now on. The latter geometry type is considered for the cases that one satellite is unhealthy or the signal from one satellite is lost because of other aircraft, vehicles, or nearby buildings. $N-1$ geometries are chosen for availability computation because this is the set of geometries that the aircraft actually experiences. Availability is obtained by counting how many geometries have HPLs less than or equal to MAE among the two geometry sets described above.

## 4.3.3 AVAILABILITY RESULTS

The comparison of availability for these two types of geometries is shown in

Figure 4.9 for a GBAS Ground Facility-to-user separation of 6 kilometers and the sigma-inflation scenario represented by the cyan (left-most) line in Figure 4.8. MAE for surface movement represents the same concept as VAL or HAL for precision approach and is evaluated for 3, 4, 5, 7.5, 10 meters, and higher with a 5-meter interval. The availability for all-in-view geometries only is 100% for an MAE of 7.5 meters or more and 94.44% for an MAE of 5 meters. On the other hand, the availability for "drill-down to one satellite out" or $N-1$ geometries is 97.76% for an MAE of 7.5 meters, 99.59% for 10 meters, and 100% for 25 meters or more. As expected, the availability for $N-1$ geometries is equal to or less than availability for all-in-view geometries. Therefore, the availability evaluations that follow in this chapter report availability for $N-1$ geometries unless mentioned specifically. Availability values for additional parameter combinations of various geometry types, inflation factors, and GBAS Ground Facility-to-user separations are available in Table C.3 of Appendix C.

Figure 4.10 shows the sensitivity of MAE and availability to constant aircraft $\sigma_{pr\_air}$ inflation for a GBAS Ground Facility-to-user separation of 6 kilometers. The $\sigma_{pr\_air}$ value for a particular satellite elevation angle is inflated by factor of 1.5, 2, 3, and 4, and these cases are represented by blue, cyan, yellow, and red bars, respectively. For a multiplier of 1.5, MAE can be reduced to 5 meters with 91.82% availability and 7.5 meters with 99.55% availability. It can be reduced to 7.5 meters with 97.76% availability for a multiplier of 2, 10 meters with 96.58% for a multiplier of 3, and 15 meters with 98.58% for a multiplier of 4. Again, additional results are in Table C.3 of Appendix C.
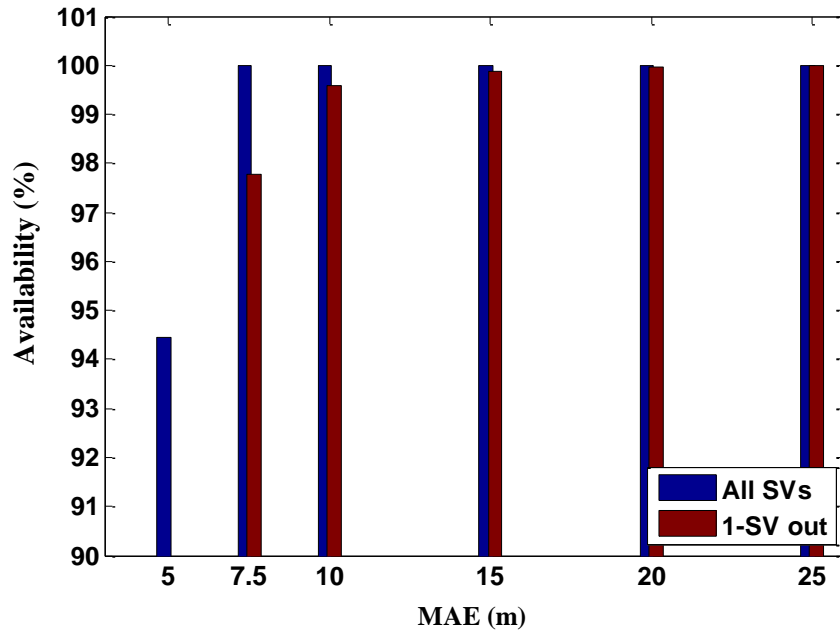


Figure 4.9. Availability for the scenario of inflated $\sigma_{vig}$ and 2 $\sigma_{pr\_air}$.
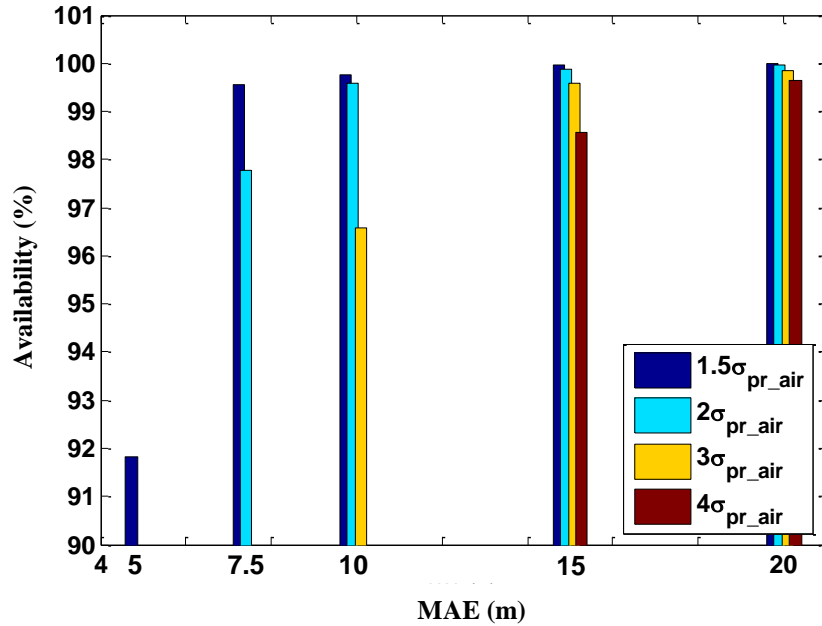
Figure 4.10. Sensitivity of MAE to aircraft $\sigma_{pr\_air}$ inflation and its availability (with inflated $\sigma_{vig}$).

# 4.4 ADDITIONAL AIRCRAFT GEOMETRY SCREENING

Figure 4.8 is revisited to consider the scenarios where the maximum value of HPE-to-HPL ratio exceeds 1.0. One example of these scenarios is the case where the aircraft $\sigma_{pr\_air}$ value is not increased when the aircraft is on the ground. The other example is where the combination of a higher $\sigma_{pr\_air}$ value to bound larger multipath errors and a version of HPE that includes nominal errors (in addition to the worst-case ionospheric error) results in the HPE-to-HPL ratio sitting in the region where the maximum ratio is over 1.0. For those scenarios, the additional aircraft geometry screening introduced in Appendix B is applied to protect integrity while lowering MAE to a usable level and maintaining a useful level of availability. Two types of aircraft geometry screening rules have been evaluated. The first

rule is limiting a "screening HAL" to less than the normal HAL or MAE that is dictated by safety concerns. The second rule is limiting the maximum absolute value of the range-to-horizontal position scalar, $|S_{horizontal}|$, where the matrix $S$ is derived from the weighted pseudoinverse of the user's GPS geometry matrix [RTCA, 2008]. In this section, the combination of GBAS Ground Facility $\sigma_{vig}$ inflation and no inflation of $\sigma_{pr\_air}$ is selected to demonstrate the capabilities of additional aircraft geometry screening.

### 4.4.1 DETERMINATION OF LIMITS

In order to show how aircraft geometry screening limits are determined, an example plot for the GBAS Ground Facility-to-user separation of 6 kilometers is shown in Figure 4.11(a). If MAE is set to be 10 meters, the significant geometries that might pose an anomalous ionospheric threat to surface movement are shown by red dots in Figure 4.11(a), and can be seen more closely in Figure 4.11(b). The required "screening HAL" is determined by the minimum HPL value among these significant geometries, and the maximum $|S_{horizontal}|$ is determined by the minimum value of $|S_{horizontal}|$ among them. Note that, where additional aircraft screening is needed, either the screening HAL or the maximum $|S_{horizontal}|$ determined in this manner is sufficient – there is no need to implement both limits at the same time.
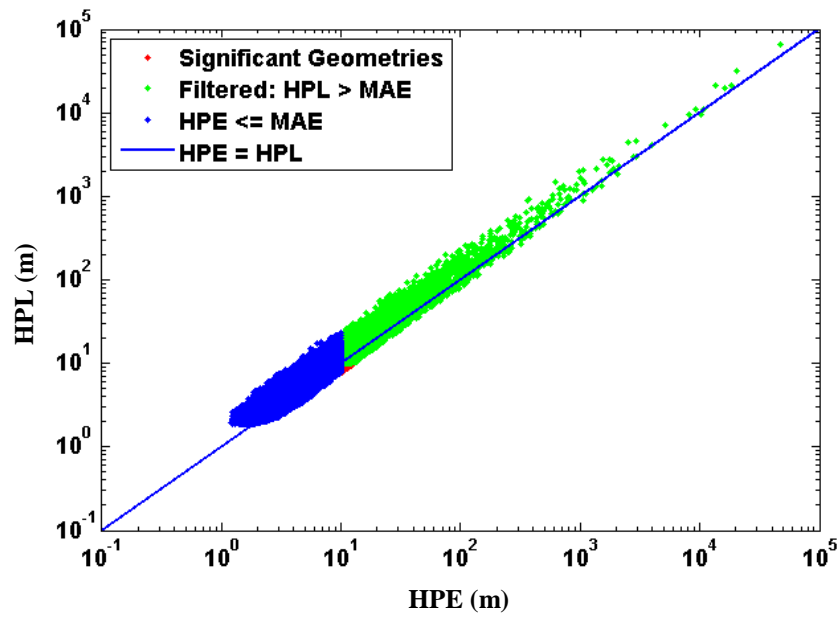
(a)
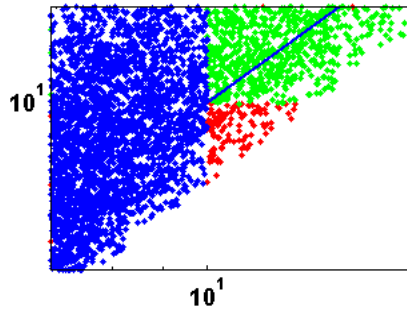


(b)

Figure 4.11. Example result of airport surface movement for 6-km separation: inflated $\sigma_{vig}$ and no inflation of $\sigma_{pr\_air}$.

## 4.4.2 AVAILABILITY COMPUTATION

Availability is determined by counting how many geometries satisfy (4-11) for the screening HAL limit or (4-12) for the maximum $|S_{horizontal}|$ limit.

$$\{HPL \leq MAE\} \cap \{HPL < \text{Screening HAL}\} \tag{4-11}$$

$$\{HPL \leq MAE\} \cap \{|S_{horizontal}| < \text{Max. } |S_{horizontal}|\} \tag{4-12}$$

## 4.4.3 AVAILABILITY RESULTS

Figure 4.12 shows availability as a function of MAE when a screening HAL is used for three GBAS Ground Facility-to-user separations of 4, 5, and 6 kilometers. For a separation of 4 kilometers, 96.17% availability is achieved for an MAE of 4 meters by using a screening HAL of 3.99 meters. In other words, the aircraft should screen out all geometries whose HPL is more than the screening HAL of 3.99 meters to support the actual ("safety") HAL of 4 meters with the required integrity. In this case, the screening HAL is only slightly less than the actual HAL; thus the additional geometry restriction is very minor. In the same manner, MAE is reduced to 5 meters with 96.01% availability using a screening HAL of 4.11 meters for a 5-kilometer separation and is reduced to 7.5 meters with 99.47% availability using a screening HAL of 5.69 meters for a 6-kilometer separation. Screening limits and availabilities for additional scenarios are provided in Table C.1 of Appendix C.

Availability with MAE when maximum $|S_{horizontal}|$ is used to screen aircraft geometries for the same three separations is shown in Figure 4.13. MAE can be reduced to 4 meters with 96.30% availability with a maximum $|S_{horizontal}|$ of 1.60 to protect integrity for the 4-kilometer separation. An availability of 94.59% is achieved for an MAE of 4 meters and a 5-kilometer separation by a maximum $|S_{horizontal}|$ of 1.35. Availability is 98.37% for an MAE of 5 meters and a separation of 6 kilometers using a maximum $|S_{horizontal}|$ of 1.47. Values for additional combinations are available in Table C.2 of Appendix C. Comparing Figure 4.13 to Figure 4.12 suggests that limiting maximum $|S_{horizontal}|$ provides slightly better availability than the screening-HAL alternative.

Figure 4.14, which gives availability for all-in-view geometries only, MAE is reduced to 3 meters with 96.53% availability by a maximum $|S_{horizontal}|$ of 1.20 for a 4-kilometer separation, with 94.44% availability by a maximum $|S_{horizontal}|$ of 1.01 for a 5-kilometer separation, and with 92.71% availability by a maximum $|S_{horizontal}|$ of 0.89 for a 6-kilometer separation. As expected, these three figures show better availability for larger MAE. As before, values for additional combinations of parameters are available in Table C.2 of Appendix C.
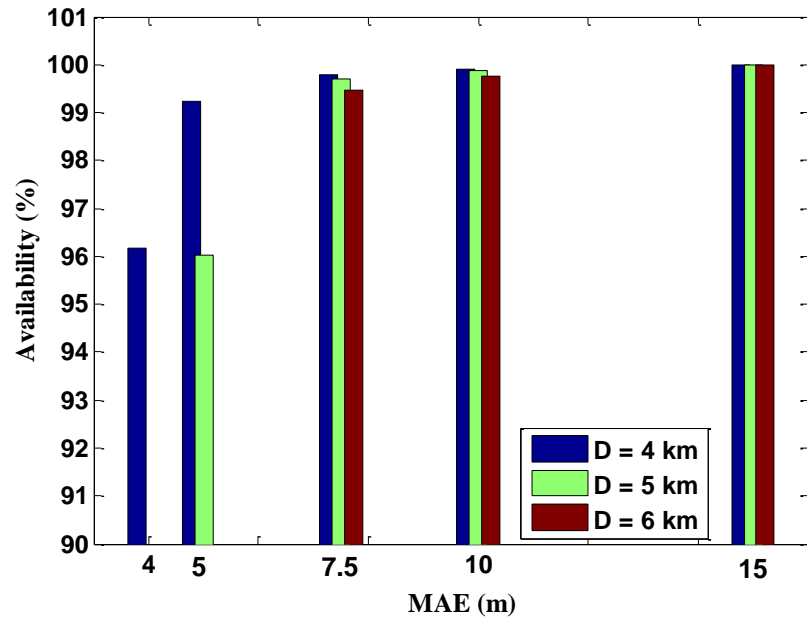


Figure 4.12. Additional aircraft geometry screening results using screening HAL: inflated $\sigma_{vig}$ and no inflation of $\sigma_{pr\_air}$.
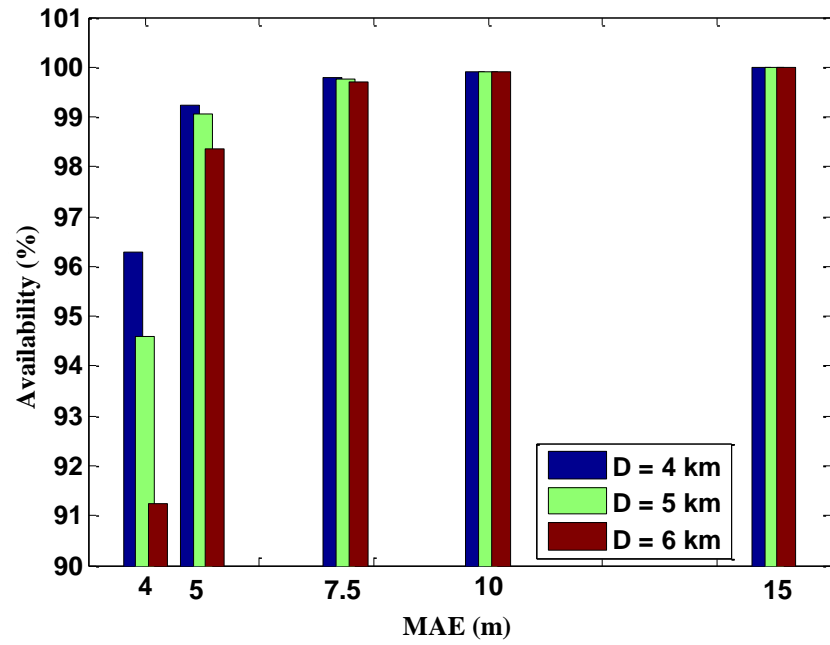
Figure 4.13. Additional aircraft geometry screening results using max. $|S_{horizontal}|$: inflated $\sigma_{vig}$ and no inflation of $\sigma_{pr\_air}$.
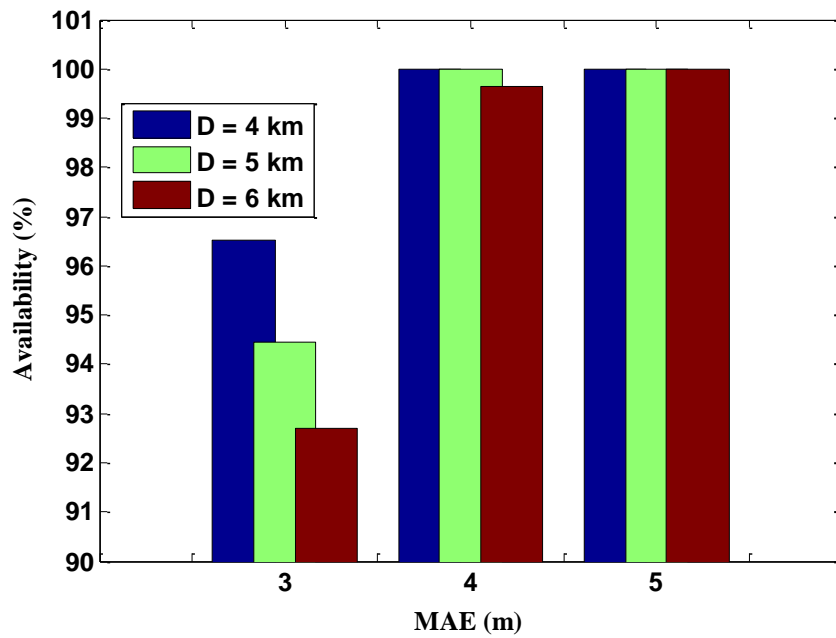


Figure 4.14. Additional aircraft geometry screening results for all-in-view geometries only using Max. $|S_{horizontal}|$: inflated $\sigma_{vig}$ and no inflation of $\sigma_{pr\_air}$.

# 4.5 SUMMARY

Four conclusions have been drawn from the airport surface movement integrity requirement analyses conducted in this chapter:

- If airport surface movement is defined as a separate operation from DCPS, it can be supported by the existing GBAS Ground Facility geometry screening and by inflating $\sigma_{pr\_air}$ by a factor of two or more with the current integrity requirements for worst-case ionospheric anomalies.

- MAE with GBAS Ground Facility geometry screening and $\sigma_{pr\_air}$ inflated by a factor of two can be reduced to 5 meters with 94.44% availability for all-in-view geometries and 7.5 meters with 97.96% availability for all $N-1$ geometries for a GBAS Ground Facility-to-user separation of 6 kilometers. Note that these results apply specifically to the Memphis GBAS installation, but similar availability should be obtainable elsewhere (simulations for other locations are beyond the scope of this dissertation).

- With the existing GBAS Ground Facility geometry screening and current aircraft $\sigma_{pr\_air}$, current airport surface movement integrity requirements cannot be met under worst-case anomalous ionospheric conditions in CONUS. Therefore, additional aircraft geometry screening, implemented by limiting either the "screening HAL" or the maximum $|S_{horizontal}|$ coefficient, is needed to fulfill the integrity requirements.

- MAE with GBAS Ground Facility geometry screening and the current $\sigma_{pr\_air}$ can be reduced to 5 meters using a maximum $|S_{horizontal}|$ of 1.47 with 98.37% availability and 7.5 meters using a screening HAL of 5.69 with 99.47% availability. These results apply to all $N-1$ satellite geometries and a 6-kilometer separation.

Taken together, these conclusions suggest that the approach described in this chapter can support airport surface movement with useful MAEs of less than 10 meters and worthwhile

availabilities of 95% or more. What makes this possible is removing airport surface movement from the domain of DCPS and defining it as an independent operation analogous to CAT I precision approach. While the separation of DCPS and surface movement is the most direct route to this objective, it may not be required if DCPS is enabled in a manner that does not limit availability based upon the worst-case ionospheric anomaly. One possibility, as proposed in [Murphy, 2010], is to use information external to GBAS to separate periods in which worst-case errors are possible from the vast majority of times when the ionosphere is known to behave nominally.

# Chapter 5

# SURFACE MOVEMENT: MULTIPATH

Chapter 4 confirmed the hypothesis that, if airport surface movement is defined as a separate operation, it could be supported by the existing GBAS Ground Facility geometry screening that mitigates the anomalous ionospheric threat for CAT I precision approach. It concluded that two or more times $\sigma_{pr\_air}$ allows us to meet the current integrity requirements and achieve a Maximum Acceptable Error (MAE) of 10 meters with more than 99% availability.

Note that this conclusion from Chapter 4 is derived under the assumption of no nominal error contribution to Horizontal Position Error (HPE) other than worst-case ionospheric errors. However, in the surface-movement environment, worst-case aircraft multipath might be a significant fraction of HPE. Limited data for airport surface movement exists at present, so examining multipath models for ground and obstruction-influenced specular reflection is the first step in exploring this further and is the subject of this chapter.

Because, for certain scenarios, GBAS Ground Facility geometry screening with the addition of $\sigma_{multipath}$ using Jahn's Multipath Model for an optimistic suburban environment is not sufficient by itself, the results in this chapter include additional aircraft geometry screening (as explained in Chapter 4 and detailed in Appendix B) to meet the requirements and lower the Maximum Acceptable Error (MAE). Since it is not clear what level of MAE corresponds to a given airport-surface operation, our goal is to minimize the achievable MAE (and thus Horizontal Alert Limit, or HAL) while maintaining useful availability.

## 5.1 MULTIPATH MODEL

Since an aircraft in airport surface movement is on the ground, it suffers from higher multipath errors than while in flight, as additional signal reflections come from the ground, other aircraft or vehicles, and nearby buildings. The multipath errors applied to generate Horizontal Position Errors (HPEs) in this chapter are based on Jahn's Multipath Model [Jahn, 1996] as used by the US/EU GNSS Working Group C (WG-C) [EU-US, 2010].

Jahn *et al*. [Jahn, 1996] illustrates the characteristics of satellite propagation channels for spread spectrum communications in detail. It gives a wideband channel model for land mobile satellite (LMS) services which characterizes the time-varying transmission channel between a satellite and a mobile user terminal. It is based on measurement campaigns at L-band. The parameters of the model are the results of fitting procedures to measured data. The parameters are shown in tables in [Jahn, 1996] for various environments and elevation angles. The implementation of Jahn's method in the urban and suburban environments for a ground user is shown in detail in [EU-US, 2010].

The approach for developing multipath models is briefly explained here. Jahn's method is used to generate the amplitudes, phases and delays of the direct and multipath signals for urban and suburban environments. The discriminator function for a non-coherent discriminator (e.g., dot-product) is employed to determine the zero crossings with and

without multipath [Hegarty, 2009]. Then, multipath error in meters is obtained by multiplying the difference of zero crossings with and without multipath in chips with the code chip width in meters [EU-US, 2010].

RMS multipath errors (in terms of 1-σ) are displayed in Figure 5.1. The red line in Figure 5.1 shows the urban multipath curve generated by Jahn's method for a BOC(1,1) signal. Several sources showed that the BOC(1,1) signal and current L1 signal produce similar multipath errors in urban and suburban environments. The data generated by Jahn's method using 2000 runs for the signal are used to obtain the fitted functions. The formula for an urban environment is taken from [EU-US, 2010] and is as follows:

$$\sigma(m) = \max(6.3784 - 3.5782 \cdot \tan^{-1}(0.1725(E(\text{deg}) - 29.075)), \varepsilon)$$

$$\varepsilon = 1 \times 10^{-4} \tag{5-1}$$

The formula of the fitted function for the suburban multipath environment is also brought from [EU-US, 2010] and is:

$$\sigma(m) = \max(0.55349 + 30.254 \cdot \exp((-0.23566E(\text{deg})), \varepsilon) \tag{5-2}$$

Note that these curves represent unsmoothed errors. In order to take advantage of the 100-second smoothing effect, it is usually decreased by a factor of 10 for time-uncorrelated errors. Since multipath is time-correlated, decreases by a factor of 3 for the conservative model (green and cyan curves in Figure 5.1) and a factor of 6 for the optimistic model (red curve in Figure 5.1) are used in this chapter. Curves of 1-σ multipath errors for the conservative urban environment (Urban-Con), the optimistic urban environment (Urban-Opt), and the conservative suburban environment (Suburban-Con) are shown in green, red, and cyan in Figure 5.1, respectively, as a function of elevation angle in degrees. The curve with the largest value (blue) is the value directly from (5-1) with no reductions due to smoothing. The dotted magenta curve in Figure 5.1 represents the curve of 1-σ multipath

errors from the airframe only (i.e., in flight), and it is shown here for comparison. This airframe-only curve in this plot already reflects 100 seconds of smoothing.
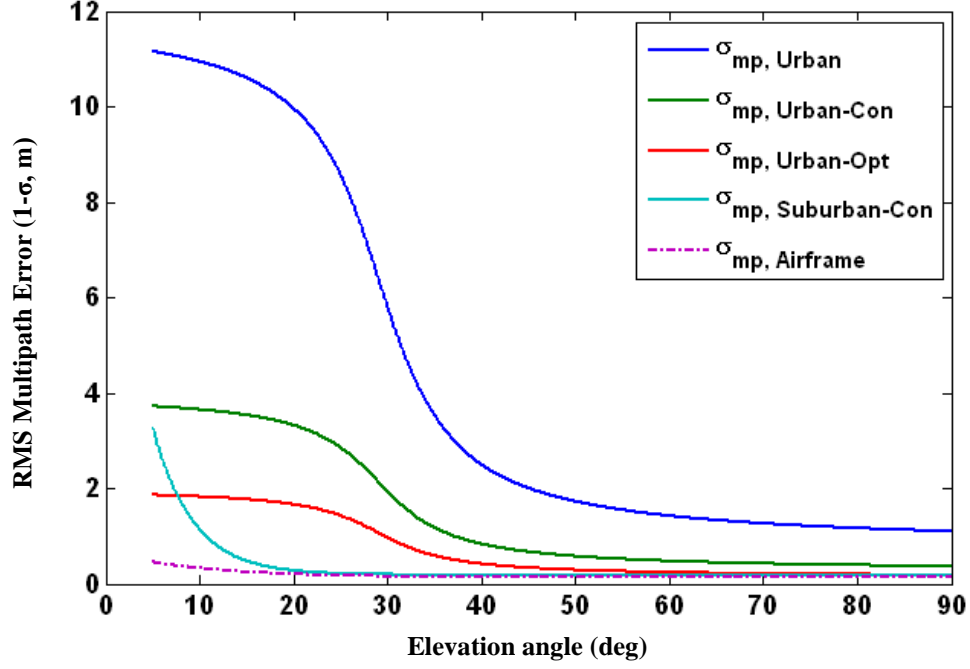


Figure 5.1. Multipath models generated by Jahn's method.

In this dissertation, three multipath models, Urban-Con, Urban-Opt, and Suburban-Con, are considered as possible sources of severe multipath errors for surface movement and are applied to satellites to generate worst-case HPEs.

## 5.2 SIMULATION PROCEDURE

The simulation procedure can be separated into two parts. One is the simulation of HPE and HPL for airport surface movement and the other is real-time $\sigma_{vig}$ inflation simulation for precision approach. The latter is described in Section 4.2.2, and the reader is referred to that section. The procedure to simulate HPE and HPL for airport surface movement has

a great amount of common ground with Section 4.2.1, and the differences will be described in this section.

The simulation procedure used to obtain HPEs and the corresponding HPLs for DCPS has been expanded from the methodology in previous chapters and is shown in Figure 5.2. One day of geometries with five-minute time updates and a five-degree visibility mask angle at Memphis International Airport (MEM) is used to generate all-in-view and down to all 1-satellite-out ($N$–1) if elevation angles of all satellites in those geometries are above 15 degrees, or down to all 2-satellite-out ($N$-2) subset geometries if the elevation angle of at least one satellite is below 15 degrees. This is based on the assumption that two satellites or more are unlikely to be lost at the same time if their elevation angles are above 15 degrees, and logically three or more satellites are also unlikely to be lost if their elevation angles are below 15 degrees, since an aircraft on the ground experiences slow maneuvering. This change in the drill-down rule from the previous chapter is made to relieve tightness of integrity analysis with more realistic geometry sets. A GBAS Ground Facility-to-user separation (distance from GBAS Ground Facility to user) of 6 kilometers is used for the simulation of GBAS airport surface movement.
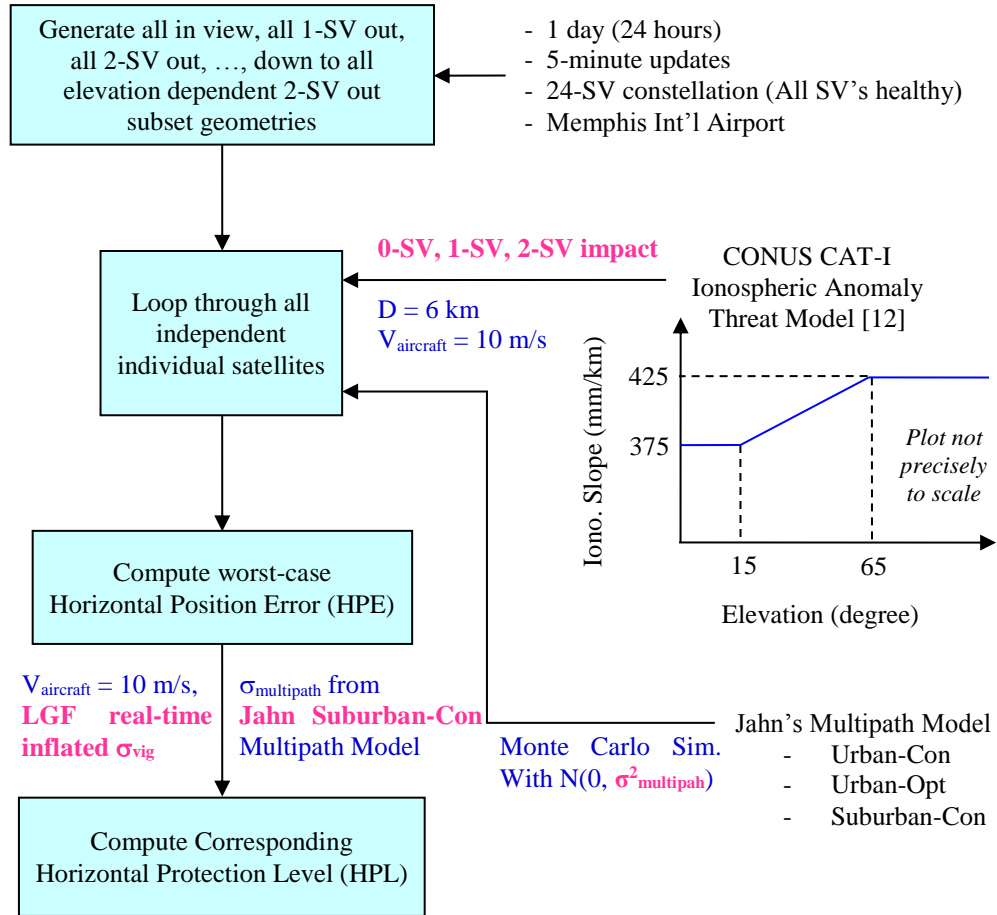
Figure 5.2. Airport surface movement simulation procedure to generate worst-case errors under ionospheric anomalies and ground multipath.

## 5.2.1 IONOSPHERIC RANGE ERROR

Worst-case GPS range errors from the anomalous ionospheric threat model for the Conterminous U.S. (CONUS) [Pullen, 2009] are applied to none of the satellites for zero-satellite (0-SV) ionospheric impact, all individual satellites in all allowed subset geometries, one satellite at a time, for one-satellite (1-SV) ionospheric impact model or to any pair of satellites (as done for precision approach) for the two-satellite (2-SV)

ionospheric impact model. The rest of the procedure to simulate ionospheric range error is the same as Section 4.2.1.1.

### 5.2.2 MULTIPATH ERROR

Random multipath errors are generated using Monte Carlo simulation with normal distributions with a mean of zero and variances of three multipath models, the Urban-Con, Urban-Opt, and Suburban-Con multipath models described in Section 5.1, and are applied to all satellites in all allowed subset geometries. 30 trials are sampled for Monte Carlo simulation, and this number of trials is chosen as a compromise between simplicity and the accuracy of surface-movement simulation.

### 5.2.3 HPL – STANDARD DEVIATIONS AND PARAMETERS

The procedure to obtain HPL is the same as in Section 4.2.1.2 except for the portions addressed in this section. In these simulations, the more conservative model (AAD A) is used for computing errors and uninflated HPL, while AAD B is used for computing inflated HPL at an aircraft. For both of these, the combination of Airframe Multipath Designator (AMD) A shown in Equation (2-35) in Section 2.2.3 as defined in [RTCA, 2004] [RTCA, 2008] and Jahn's Multipath Model in Section 5.1 and 5.2.2 is used for the aircraft $\sigma_{multipath}$ by adding two multipath $\sigma$'s together (former for aircraft multipath and latter for ground multipath) using Root of Sum of Squares (RSS).

## 5.3 INTEGRITY ANALYSIS AND AVAILABILITY COMPUTATION

Since GBAS airport surface movement is currently one of the operations of DCPS, the GBAS integrity requirements for surface movement in this dissertation are borrowed from the current GBAS requirements for DCPS integrity. They are again that position errors

should be bounded by the corresponding protection levels to the $10^{-7}$-per-hour probability level. In other words, HPEs must always be bounded by their HPLs in this context.

Given worst-case HPE and HPL per drill-down-to elevation dependent two-satellite-out subset geometry as a result of the simulation illustrated in Section 5.2, two scenarios of integrity analysis are shown. One is the case where the integrity requirements are met and therefore no additional geometry screening is needed, and the other is the case where they are not met and therefore need additional aircraft geometry screening. All drill-down-to elevation dependent two-satellite-out subset geometries are used for the integrity analysis since all possible geometries should be considered for integrity analysis by its definition. Availability is calculated from a set of all-in-view geometries plus subset geometries with one satellite missing (these will be called "drill-down to one satellite out" geometries or "$N$-1 geometries" from now on) because this is the set of geometries that the aircraft actually experiences.

## 5.3.1 NO ADDITIONAL GEOMETRY SCREENING

***Integrity Analysis***

Simulated HPEs from which an aircraft would suffer anomalous ionospheric residual errors and severe multipath errors, and the corresponding HPLs which it would calculate using real-time GBAS Ground Facility $\sigma_{vig}$ inflation and the Suburban-Con multipath model for $\sigma_{multipath}$, are shown in Figure 5.3. Note that HPE is unacceptably large for surface movement up to the order of 100 meters only because no advanced HAL-HPL check to screen out bad geometries is performed, since HAL is not specified in surface movement (or DCPS) yet.

Along the black line, HPE is the same as HPL. In the upper triangle above this black line, HPE is bounded by HPL, while HPE is not bounded by HPL in the triangle below it. The blue dots represent geometries with acceptable errors when the allowed MAE is 20 meters.

The green dots refer to geometries filtered by their HPLs, since the aircraft would screen out all the geometries whose HPL is greater than this MAE. Any red dots denote significant geometries that might pose an anomalous ionospheric or multipath threat to surface movement. Surface movement integrity cannot be met under anomalous ionosphere and severe multipath unless these red points are made unavailable by some other means proposed in the previous chapter and this chapter.

The scenario displayed in Figure 5.3 does not have any significant geometries (red dots). In other words, it meets the surface-movement integrity requirements for an MAE of 20 meters. Therefore, no additional geometry screening is required for this scenario.
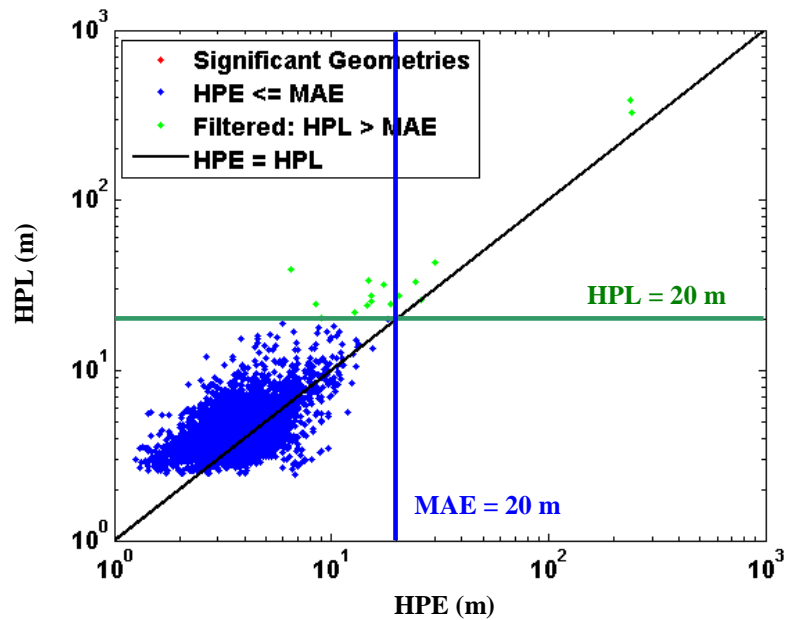


Figure 5.3. Example scenario in which the proposed GBAS surface-movement integrity requirements are met.

*Availability Calculation*

Availability is obtained by counting how many geometries have HPLs less than or equal to the screening limit. which is the same as MAE (20 m) in this scenario, among $N-1$ geometries. In Figure 5.4, the red dots above the red line are unavailable.
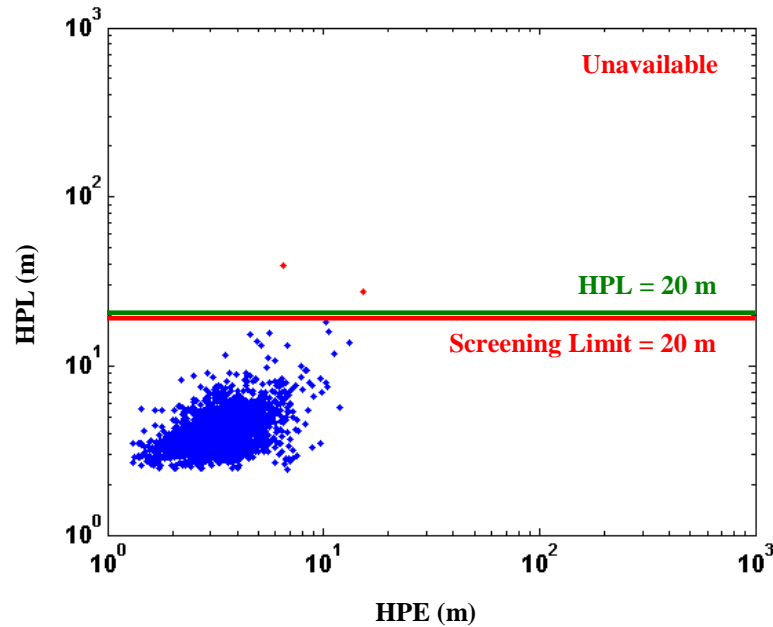


Figure 5.4. Example scenario in which the proposed GBAS surface-movement integrity requirements are met (availability determination is shown for $N$-1 geometries).

## 5.3.2 ADDITIONAL GEOMETRY SCREENING

*Integrity Analysis*

In this sub-section, an allowed MAE of 10 meters is selected to demonstrate the capabilities of additional aircraft geometry screening. The same HPEs and HPLs as in Figure 5.3 are shown in Figure 5.5. By reducing the allowed MAE from 20 to 10 meters, significant geometries appear as defined before – these are shown as red dots in Figure 5.5. Additional

aircraft geometry screening (as introduced in the previous chapter) is needed to make these points unavailable and thus protect integrity. This method introduces a "screening HAL" that is lower than the normal safety-zone HAL or MAE. The required "screening HAL" is determined by the minimum HPL value among these significant geometries, which is 5.73 meters for this scenario (see Figure 5.5). This lower limit on HPL ensures that, for this scenario, potentially threatening points are screened out by users.
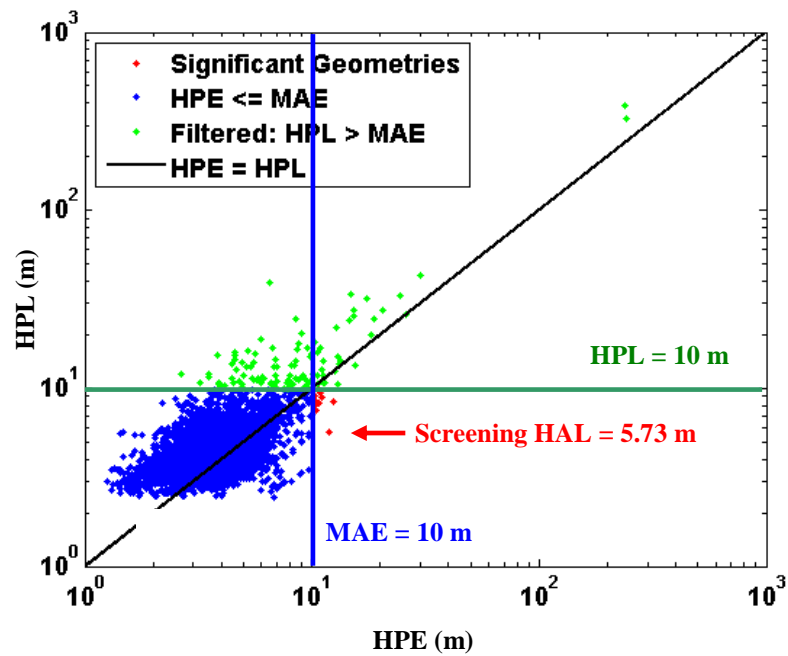


Figure 5.5. Example scenario in which the proposed GBAS surface movement integrity requirements are met by lowering the screening limit.

*Availability Calculation*

Availability is determined by counting how many geometries have HPLs less than or equal to the screening limit, which is the same as screening HAL (5.73 m) in this scenario, among $N-1$ geometries. In Figure 5.6, the red dots above the red line are unavailable.
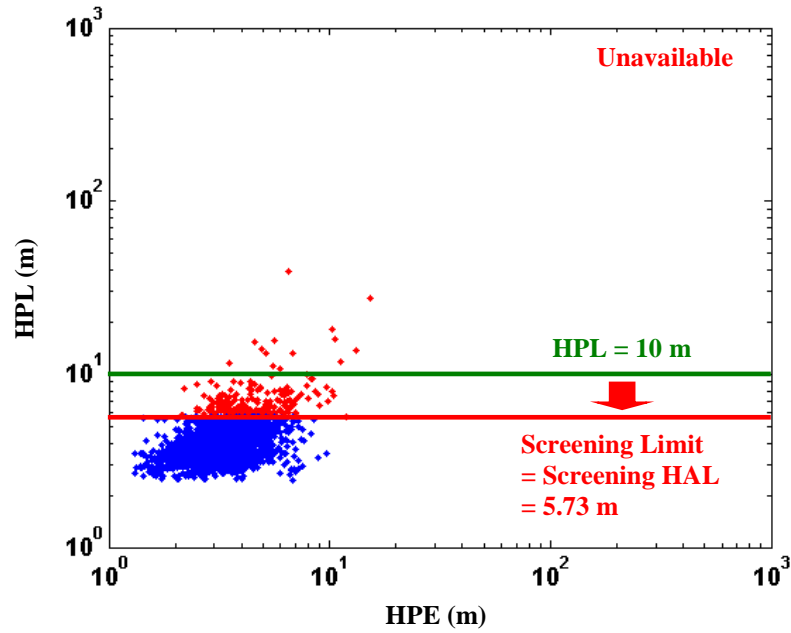
Figure 5.6. Example scenario in which the proposed GBAS surface-movement integrity requirements are met by lowering the screening limit (points counted for availability are shown).

# 5.4 RESULTS AND DISCUSSION

In this chapter, the feasibility of GBAS for airport surface movement is shown in terms of sensitivity of availability to the multipath model and the ionospheric threat impact model for several values of MAE. Results for an MAE of 30 meters are shown in Figure 5.7; for an MAE of 20 meters in Figure 5.8; and for an MAE of 10 meters in Figure 5.9. The multipath models considered are no multipath, suburban-conservative (Suburban-Con), urban-optimistic (Urban-Opt), and urban-conservative (Urban-Con), and they are shown on the vertical axis. The zero-satellites (0-SV, no ionosphere, meaning no ionospheric threat), one-satellite (1-SV), and two-satellite (2-SV) impact models of ionospheric threat are shown on the horizontal axis. The values in the figures represent availabilities as percentages, while the values in the parentheses refer to the required screening HAL limits

in meters at the aircraft. One can easily see in the figures that the screening limits and their associated availabilities decrease as we move to the right on the horizontal axis, up on the vertical axis, and the value of MAE decreases (i.e., moving from Figure 5.7 to Figure 5.8 and then Figure 5.9).

As shown in Figure 5.7, setting an MAE to 30 meters gives very high availabilities, more than 99% for all the combinations of multipath models and ionospheric threat impact models. Most of the multipath models provide more than 99.9% except for the Urban-Con model. For example, ionospheric range error impacting one satellite combined with Suburban-Con multipath provides 99.9% with no additional aircraft geometry screening, since the screening limit is 30 meters, which is the same as the MAE. A 30-meter MAE is actually not of great interest, since this MAE may not provide useful surveillance or guidance applications for airport surface movement. However, results for a 30-meter MAE are shown here for users who might be interested in this level of error.
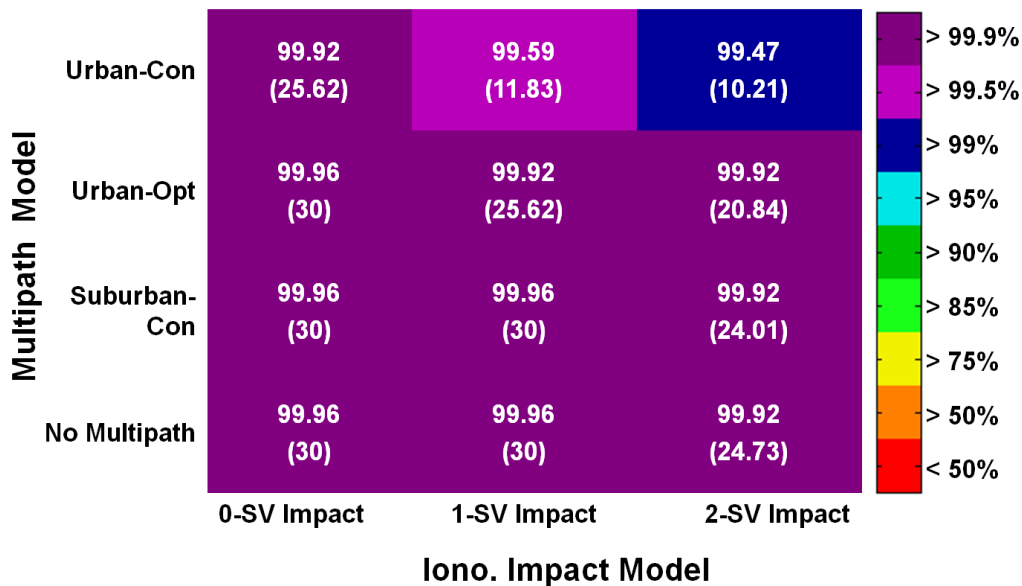


Figure 5.7. Sensitivity of availability to the multipath model and the ionospheric threat impact model for MAE = 30 m using 24-SV GPS constellation (Availability in %, Screening HAL in meters).
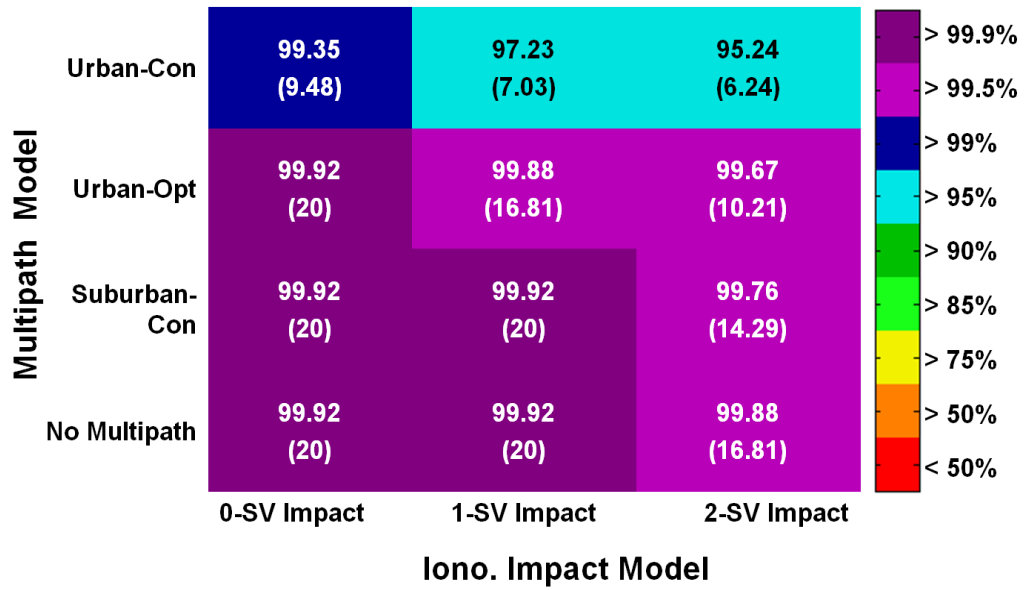
Figure 5.8. Sensitivity of availability to the multipath model and the ionospheric threat impact model for MAE = 20 m using 24-SV GPS constellation (Availability in %, Screening HAL in meters).
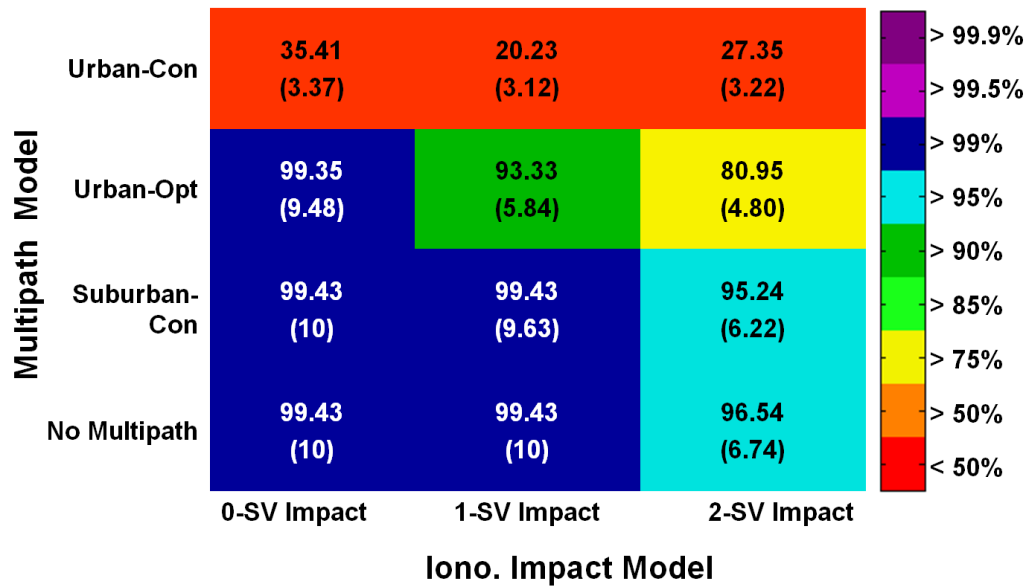


Figure 5.9. Sensitivity of availability to the multipath model and the ionospheric threat impact model for MAE = 10 m using 24-SV GPS constellation (Availability in %, Screening HAL in meters).

In Figure 5.8, results for an MAE of 20 meters are shown. Under the Urban-Con multipath threat, 95% airport surface movement availability is achievable. Lesser multipath errors provide 99% availability. The suitable model for most airport surface movement applications since most airport environment has small number of low buildings, Suburban-Con multipath, combined with the ionospheric impact to one satellite, gives 99.9% availability. No additional aircraft geometry screening is needed here. To see the effect of the number of satellites impacted by the ionospheric threat, the combination of 1-SV ionospheric impact and the Suburban-Con multipath model gives more than 99.9% availability for an MAE of 20 meters, while the combination of 2-SV impact of ionospheric threat and the Suburban-Con multipath model provides more than 99.5% availability for the same MAE. An MAE of 20 meters is of particular interest because this is the width of airport taxiways, and thus a 20-meter MAE might be of importance to surveillance applications.

An MAE of 10 meters is evaluated to examine the usefulness of GBAS-guided airport surface movement. The red boxes in Figure 5.9 indicate that the achievable availabilities are less than 50%. It is obvious that the proposed GBAS airport surface movement is not feasible for the airport environment with Urban-Con multipath. However, less-conservative multipath models may provide availabilities higher than 90-95%. The combination of 1-SV ionospheric impact and the Suburban-Con multipath model provides 99.4% availability using additional aircraft geometry screening with a "screening HAL" of 9.63 meters in order to achieve an MAE of 10 meters. As before, this screening HAL is different from and is less than the MAE.

# 5.5 SUMMARY

## 5.5.1 SUMMARY OF RESULTS

To encapsulate the results in this chapter, the smallest achievable MAEs with more than 99% surface movement availability for a 24-satellite GPS constellation at Memphis (with no satellite outages) are summarized in Table 5.1. The achievable MAEs with more than 95% are summarized in Table 5.2. Again, as mentioned in Section 5.3, availability is calculated from a set of drill-down to one satellite out" geometries ($N$-1 geometries). Note that all MAEs listed in Table 5.2 are less than 20 meters. This leads to the conclusion that the proposed GBAS airport surface movement is feasible for surveillance applications. Guidance applications most likely require MAEs of 10 meters or less, and these are also feasible if multipath models less extreme than Urban-Con are used.

Table 5.1. Summary of the smallest achievable MAEs with 99 % availability using 24-SV GPS constellation

| Multipath Model \ Iono. Impact Model | 0-SV Impact | 1-SV Impact | 2-SV Impact | |
|---|---|---|---|---|
| Urban-Con | 18 m | 23 m | 24.5 m | |
| Urban-Opt | 9 m | 14.5 m | 16.5 m | Surveillance (MAE < 20) |
| Suburban-Con | 8.5 m | 9 m | 13 m | Guidance (MAE < 10) |
| No Multipath | 8.5 m | 8.5 m | 12 m | |

Table 5.2. Summary of the smallest achievable MAEs with 95 % availability using 24-SV GPS constellation

| Iono. Impact Model / Multipath Model | 0-SV Impact | 1-SV Impact | 2-SV Impact |
|---|---|---|---|
| Urban-Con | 13.5 m | 16.5 m | 18 m |
| Urban-Opt | 7 m | 10.5 m | 12.5 m |
| Suburban-Con | 6.5 m | 7 m | 9.5 m |
| No Multipath | 6.5 m | 6.5 m | 9 m |

Surveillance (MAE < 20)

Guidance (MAE < 10)

## 5.5.2 CONCLUSIONS

This chapter has proposed removing GBAS airport surface movement from the domain of DCPS and making it a separate operation. If this is done, the existing CAT I GBAS can support high-availability airport surface movement for an MAE of 20 meters, even if worst-case ionosphere is combined with Urban-Con multipath. Under lesser multipath threats, meaning either that multipath is less severe or that surface movement is not allowed where Urban-Con multipath could occur, MAEs below 10 meters are achievable. Note that these results are based upon the approach used for CAT I in which only worst-case ionospheric and multipath errors (but no other errors) contribute to HPE. This assumption is reasonable as long as anomalous ionosphere or severe multipath continues to be the dominant threat.

# Chapter 6

# CONCLUSIONS

## 6.1 SUMMARY

This dissertation adapts GBAS integrity requirements to the new application of airport surface movement and analyzes the sensitivity of airport surface movement integrity to severe ionospheric and multipath conditions. This research demonstrates the feasibility of GBAS for airport surface movement as a function of threat model and Maximum Acceptable Error (MAE).

The approach described in this dissertation can support airport surface movement with useful MAEs of less than 10 meters and worthwhile availabilities of 95% or more. What makes this possible is removing airport surface movement from the domain of DCPS and defining it as an independent operation analogous to CAT I precision approach. If this is done, the existing CAT I GBAS can support high-availability airport surface movement for an MAE of 20 meters, even if worst-case ionosphere is combined with worst-case multipath. Under lesser multipath threats, meaning either that multipath is less severe or

that surface movement is not allowed where worst-case multipath could occur, MAEs below 10 meters are achievable.

## 6.2 BRIDGE TO THE FUTURE

Because multipath under surface-movement conditions is the key unknown in this study, actual data from a variety of airport surface conditions is needed and is the next important step in this research. Limited taxi-movement data is available from flight tests conducted by the FAA Technical Center and the Institute of Flight Guidance and Control at the Technical University of Braunschweig, Germany. Tests focused on the surface movement environment have been conducted at Munich airport by DLR in Oberpfaffenhofen, Germany [Asam, 2010]. The results of these tests will clarify which of the scenarios examined in this dissertation is most realistic for the future.

This research uses single-frequency GPS because current GBAS systems approved by the FAA only monitor and augment the GPS L1 C/A broadcast. GBAS targets the extremely high accuracy, availability, and integrity necessary for Category I, and eventually Category II and III precision approaches. The FAA GBAS program is currently conducting a research and development and prototyping effort to reduce the technical risk and validate new requirements associated with meeting the GBAS approach service type D (GAST-D) service, which will be capable of supporting approaches to Category III (CAT-III) minima [FAA, 2015]. Beyond GAST-D, the future of GBAS may include multiple frequencies and multiple constellations to further enhance service availability. Usage of multiple frequencies can reduce the risk of ionospheric anomalies and thus make it easier to meet the requirements of DCPS integrity. Multiple frequencies and multiple constellations may provide better accuracy, integrity, and availability for DCPS and surface movement. Research on DCPS performance in the context of future GBAS would be important future work.

# Appendix A

# DCPS INTEGRITY ANALYSIS

This appendix demonstrates that the requirement in current GBAS standards is hard to achieve under anomalous ionosphere and proposes potential requirement changes to improve DCPS availability. Horizontal Position Error (HPE) is calculated from the current ionosphere threat model and is applied to individual satellites in all subset geometries. Limited subset geometries and screening Horizontal Alert Limit (HAL) are considered as requirement changes for current LAAS Minimum Operational Performance Standards (MOPS) for DCPS. Limited subset geometries with drill down to $N$-2 satellites (or SV's) reduced the maximum unbounded HPE from 6 kilometers to 110 meters. The introduction of a "screening HAL" of 550 meters supports a maximum HPE of 300 meters.

## A.1 DCPS DEFINITION

The definition of DCPS is explained in Section 1.2.3. The primary service that GBAS provides is precision approach, and secondary services include terminal area operations, aircraft operations in terminal area airspace, and airport surface movement, i.e., aircraft movement on the ground of the airport, such as taxiing. The Differentially Corrected

Positioning Service (DCPS) is an extension of GBAS capability to support terminal area operations and airport surface movement. In other words, DCPS is everything not covered by precision approach.

An example of DCPS is Required Navigation Performance (RNP), a type of Performance-Based Navigation (PBN) that allows an aircraft to fly a specific path between two 3D-defined points in space. RNP uses the capability of modern aircraft to fly along tightly confined airspace corridors, as shown in Figure A.1.

It is preferable that GBAS provides usable guidance wherever the VDB can be received. Without supporting DCPS, other services than GBAS are required to get an aircraft to the beginning of a precision approach, which limits the benefit of GBAS. The desire is to be able to support the entire RNP approach procedure from the farthest extension of GBAS VDB coverage all the way down till the beginning of precision approach so that we only need GBAS (as shown in Figure A.2). Everything included in this gap can be thought of as "terminal area operations" that can be supported by certain error bounds in the horizontal direction. The nominal performance of GBAS is more than good enough to support this, but GBAS cannot currently provide this service because we do not have a complete GBAS integrity error bound for DCPS.
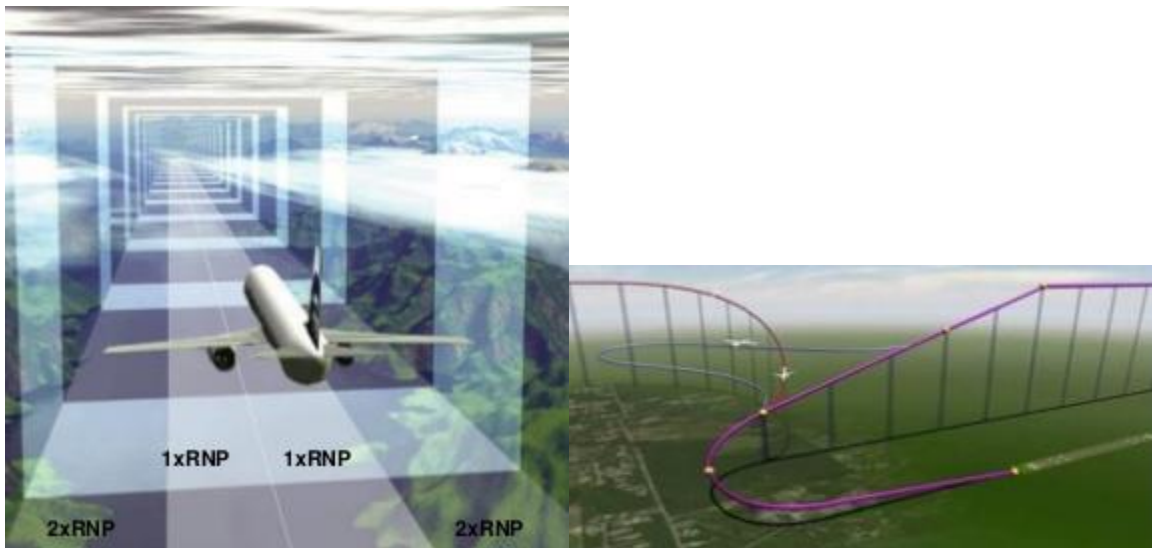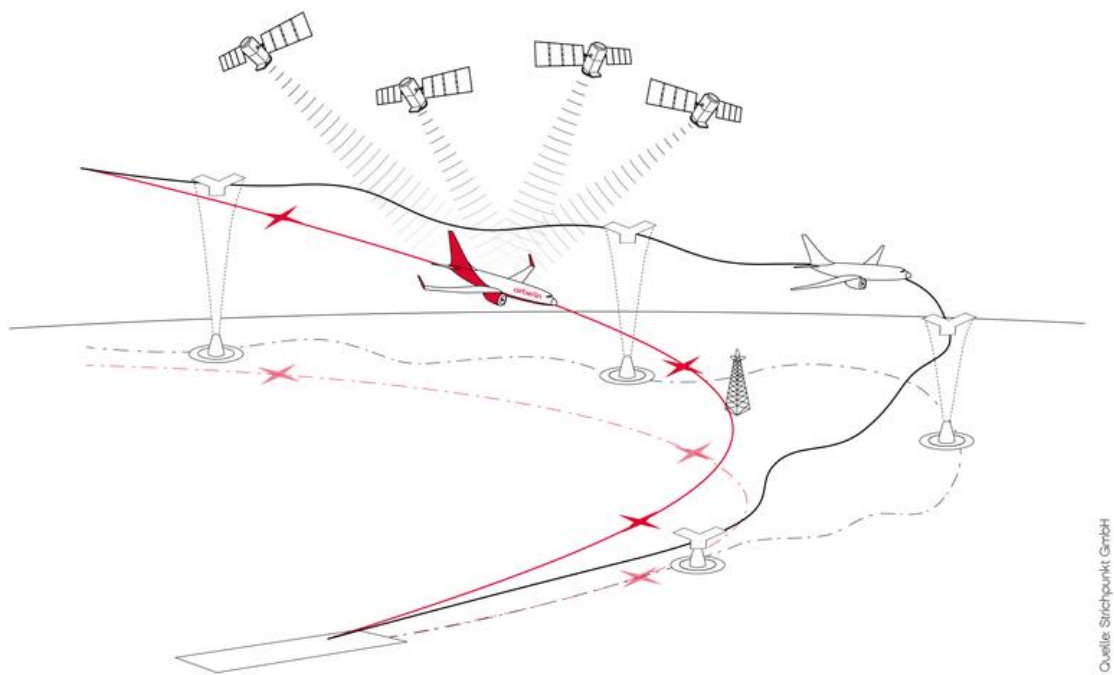
Figure A.1. Satellite-based RNP approach procedure [www.airberlingroup.com] [www.slideshare.net].
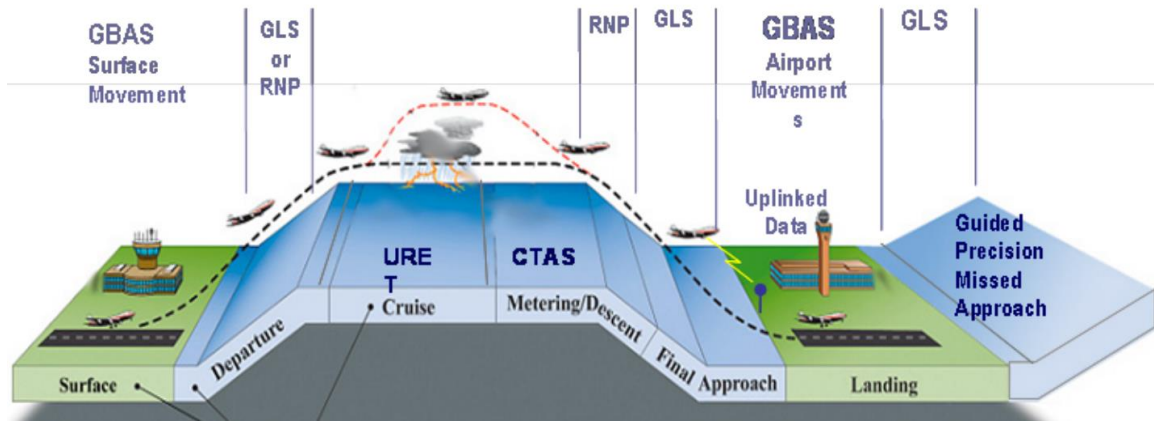
Figure A.2. Phase of flights and GBAS; GLS stands for GBAS Landing System [Boeing, 2009].

# A.2 DCPS LIMITATION

Ground geometry screening (as described in Section 3.4) works reasonably well for precision approach applications, where the Vertical Alert Limit (VAL) and Obstacle Clearance Surface (OCS) limits for precision approaches are well-defined, but it cannot be directly transported to the DCPS application because no single Horizontal Alert Limit (HAL) is defined for DCPS. This is because DCPS is intended to support a variety of terminal area operations with different values of HAL; thus no one HAL value can be used to define DCPS integrity. The comparison between precision approach and DCPS is summarized in Table A.1. Precision approach has a known operation, a known VAL (10 meters at the DH), and may also have constrained subset geometries. Therefore, the GBAS Ground Facility can predict what geometries would be hazardous and can take action to get rid of them. DCPS is intended to support many different operations with different HAL values. Therefore, the GBAS Ground Facility cannot predict what geometries would be hazardous for all DCPS applications. For this reason, the existing GBAS requirements call for the Horizontal Protection Level (HPL) to always exceed the maximum HPE, but the results in [Park, 2007] show that this is not possible in the face of the ionosphere anomalies

observed in October and November of 2003 unless the resulting HPL is inflated to be hundreds or thousands of meters.

Table A.1. Comparison between Precision approach and DCPS

| Precision Approach | DCPS |
|---|---|
| Known operation | Many different operations |
| Known VAL | Undefined HAL values |
| Constrained subset geometries | No constraints on subset geometries |

| Action to get rid of hazardous geometries | No action to take care of hazardous geometries |
|---|---|

Given that the existing DCPS integrity requirements cannot be met in the presence of the worst ionosphere anomalies observed in the past, this appendix examines several possible system modifications to make DCPS more useful. One approach examined requires changes to the LAAS MOPS [RTCA, 2008] – constraints are imposed on airborne geometry screening. The second approach investigated is to mandate screening the HAL value taken for all the terminal-area operations from RTCA DO-236B [RTCA, 2003]. This section considers the various modifications taken together and recommends a way forward to enhance the availability and utility of DCPS without affecting the safety of DCPS users.

# A.3 SIMULATION PROCEDURE

The DCPS simulation procedure is shown in Figure A.3. One day of geometries with five minute updates from Memphis airport is used to generate all in view, all $N$-1, all $N$-2, …,

down to all four-satellite subset geometries. Range errors from the ionosphere threat model are applied to all independent individual satellites in those subset geometries. A value of $\sigma_{vig}$ of 18.4 millimeters per kilometer, which is very large and is not far short of the maximum possible broadcast $\sigma_{vig}$ value of 25.5 millimeters per kilometer, is used. Then computed HPE and HPL are obtained, and only the worst HPE and corresponding HPL are saved. When we consider possible requirement changes, geometry screening with what is defined as a "screening HAL" (as distinct from the actual HAL that defines the limit of safe error) is applied so that only points whose HPL values are less than this screening HAL survive. Finally, maximum HPE with a specific screening HAL value is obtained.

DCPS simulation is applied to three scenarios specified in Table A.2. 5-km GBAS Ground Facility-to-user separation represents airport surface, and the altitude of zero meters and the aircraft speed of zero meters per second are used for the first scenario. 15-km GBAS Ground Facility-to-user separation represents the terminal area inside GBAS coverage, and 45-km GBAS Ground Facility-to-user separation represents the edge of GBAS coverage. The second and third scenarios use an altitude of 3000 meters and aircraft speed of 70 meters per second.
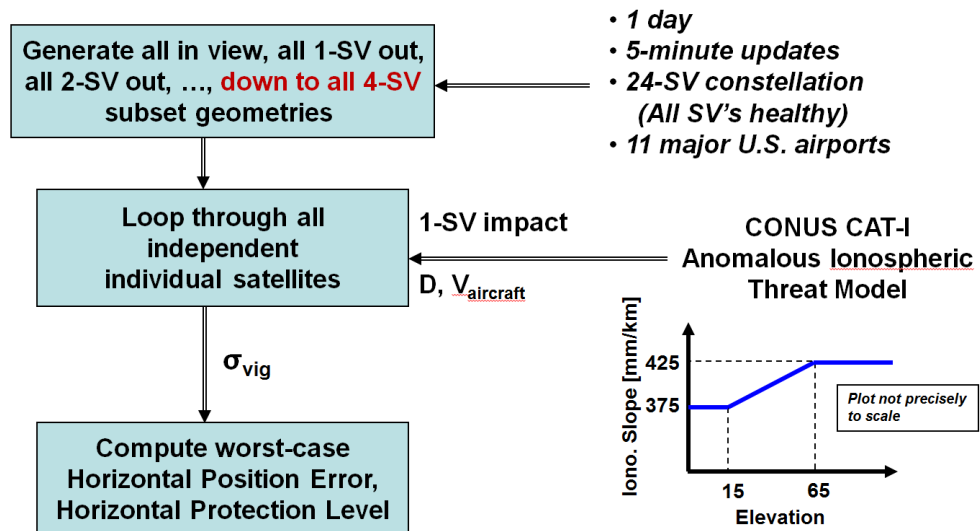


Figure A.3. DCPS Simulation procedure to obtain HPE and HPL.

Table A.2. DCPS Scenario

| Scenario No. | Description | $x$ (km) | Altitude (m)[a] |
|:---:|:---:|:---:|:---:|
| 1 | Airport Surface | 5 | 0 |
| 2 | Terminal Area, Inside GBAS Coverage | 15 | 3000 |
| 3 | At Edge of GBAS Coverage ($D_{max}$) | 45 | 3000 |

[a]Altitude makes little difference to DCPS error results.

# A.4 IONOSPHERIC ANOMALY IMPACT ON ONE SV

## A.4.1 EFFECT OF GEOMETRY ON HPE

Figure A.4 shows an HPE versus HPE-to-HPL ratio plot of ionosphere anomaly impact on one satellite with "drill down" to four SV geometries (meaning that all satellite subsets down to the minimum of four satellites are considered) for the 45-km GBAS Ground Facility-to-user separation case. HPE-to-HPL ratios below one indicate that their HPE values are always less than their HPL values, and so they are protected by their HPL values. The point in the magenta circle indicates the maximum HPE, which is approximately 267 kilometers. This large error is caused by a very poor geometry, which is shown in Figure A.5. This geometry has only the minimum number of four satellites. The $S_{horizontal}$ values of the four satellites in Figure A.5 are shown in Table A.3. Here, the $S$ matrix is the pseudo-inverse of the $G$ matrix, and it produces position error by being multiplied by range errors of satellites in geometry. The $S_{horizontal}$ value is the horizontal component of the $S$ matrix. The $S_{horizontal}$ values in Table A.3 are big enough to produce this large HPE. The satellite in

the red circle in Figure A.5 and Table A.3 indicates impact by ionosphere anomaly. The worst HPE is calculated when satellite No. 3 is chosen to be impacted in this geometry because the $S_{horizontal}$ value of this satellite is the largest.

The corresponding all-in-view geometry that gives the maximum HPE mentioned in the previous paragraph and its $S_{horizontal}$ values are shown in Figure A.6 and Table A.4, respectively. It has three more satellites in the green oval at high elevation, for a total of seven satellites, and they are distributed well in elevation and azimuth. An ionospheric impact on satellite No. 6 produces the worst HPE in this all-in-view geometry because its elevation is so high, above 65 degrees, that its range error calculated from the ionosphere anomaly threat model is the largest. Although its $S_{horizontal}$ value is the lowest among the satellites in this geometry, the effect of the range error is bigger than the effect of the $S_{horizontal}$ value. The HPE corresponding to this all-in-view geometry is approximately 10 meters, which is a point in the green circle in Figure A.4.



Figure A.4. HPE versus HPE-to-HPL ratio plot of ionosphere anomaly impact on one SV with drill down to four SVs for 45-km separation case.
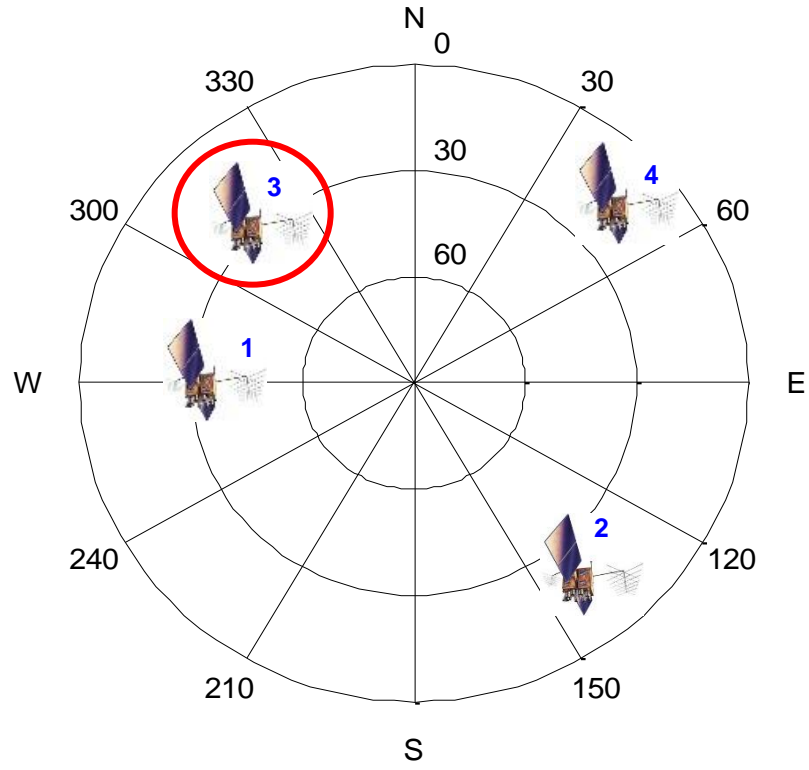
Figure A.5. Sky plot of corresponding geometry giving maximum HPE of ionosphere anomaly impact on one SV with drill down to four SVs for 45-km separation case.

Table A.3. $S_{horizontal}$ values of satellites in Figure A.5

| SV No. | $S_{horizontal}$ |
|--------|------------------|
| 1      | 13548            |
| 2      | 5525             |
| 3      | 15496            |
| 4      | 7473             |
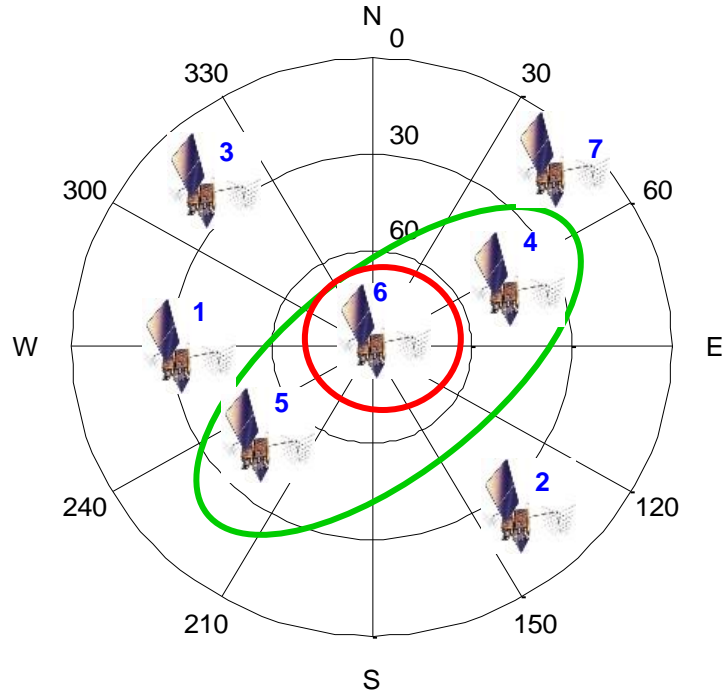
Figure A.6. Sky plot of all-in-view geometry corresponding to the maximum HPE (magenta circle in Figure A.4) of ionosphere anomaly impact on one SV with drill down to four SVs for 45-km separation case.

Table A.4. $S_{horizontal}$ values of satellites in Figure A.6

| SV No. | $S_{horizontal}$ |
|--------|------------------|
| 1 | 0.3446 |
| 2 | 0.6415 |
| 3 | 0.3812 |
| 4 | 0.3733 |
| 5 | 0.3463 |
| 6 | 0.1625 |
| 7 | 0.3633 |

## A.4.2 EFFECT OF GBAS GROUND FACILITY-TO-USER SEPARATION ON DCPS

HPE versus HPE-to-HPL plots of the ionosphere anomaly impact on one SV with drill down to four satellites for the 15-km GBAS Ground Facility-to-user separation case and for the 5-km GBAS Ground Facility-to-user separation case are shown in blue in Figure A.7 and in green in Figure A.8, respectively. The red points in Figure A.7 and Figure A.8 represent the 45-km GBAS Ground Facility-to-user separation case and are the same as in Figure A.4. The maximum HPE is approximately 90 kilometers for the 15-km GBAS Ground Facility-to-user separation case and 30 kilometers for the 5-km GBAS Ground Facility-to-user separation case. These two separation cases do not have any points whose HPE-to-HPL ratios exceed one, which means their HPE values are always less than their HPL values, while the 45-km GBAS Ground Facility-to-user separation case has some cases, shown in the gray box, whose HPE-to-HPL ratios exceed one. In other words, the points in blue and green are protected by their HPL values, whereas some points in red are not protected by their HPL values. The maximum unbounded HPE for the 45-km GBAS Ground Facility-to-user separation case is approximately 6 kilometers, which is more hazardous than its maximum HPE of 267 kilometers since it is not bounded by its HPL. From the 15-km GBAS Ground Facility-to-user separation case to the 45-km GBAS Ground Facility-to- user separation case, there is a monotonic increase of the HPE-to-HPL ratio toward its value of one. At a GBAS Ground Facility-to-user separation of about 21.5 km, we start to have points in the gray box. The reason the 5-km GBAS Ground Facility-to-user separation case is not a component of the monotonic increase is because different parameters are used for this case. The aircraft speed of zero meters per second and the altitude of zero meters are used for the 5-km GBAS Ground Facility-to-user separation case, while aircraft speeds of 70 meters per seconds and altitude of 3000 meters are used for other separations. Zero aircraft speed produces better results because of the velocity term in equation (2-38).

As explained here, 5-km and 15-km GBAS Ground Facility-to-user separation cases do not harm DCPS users, whereas some cases in 45-km GBAS Ground Facility-to-user separation could cause harm. The red points in the gray box are candidates for mitigation by altering requirements in the current LAAS MOPS for DCPS.



Figure A.7. HPE versus HPE-to-HPL ratio plot of ionosphere anomaly impact on one SV with drill down to four SVs for 45-km (red) and 15-km separation case (blue).

Figure A.8. HPE versus HPE-to-HPL ratio plot of ionosphere anomaly impact on one SV with drill down to four SVs for 45-km (red), 15-km (blue), and 5-km separation case (green).

# A.5 CHANGES TO IMPROVE DCPS AVAILABILITY

## A.5.1 POTENTIAL REQUIREMENTS CHANGES

Three potential requirement changes to existing LAAS MOPS for DCPS are considered here. The first change considered in this appendix is limiting the extent of subset geometries. It restricts DCPS users to specific subsets that can be protected. The current MOPS for DCPS allows all geometries with four or more satellites. Limited subset geometries allow, for example, all zero-, one- and two-satellite-out combinations, which is called drill down to $N$-2 satellites. The second change considered here is applying the screening HAL, which specifies a uniform maximum HPL for all DCPS users. Since HAL

values are not defined in the current LAAS MOPS for DCPS, DCPS users can determine their own HAL values according to their operations, e.g., 25 meters for airport surface movement. The screening HAL can provide a bound to DCPS users when they choose their own HAL values for their own operations. Supported operations with smaller HAL values would not be affected. The third change to be considered is airborne Code-Carrier Divergence (CCD) monitoring, which is now required for GBAS approach service type D (GAST-D) precision approaches in the current LAAS MOPS (DO-253C) [RTCA, 2008]. The third change is not considered in this work.

## A.5.2 LIMITED SUBSET GEOMETRIES

The effect of various limited subset geometries on HPE is examined for the ionosphere anomaly impact on the one-SV-impact and 45-km GBAS Ground Facility-to-user separation case. HPE versus HPE-to-HPL ratio plots with drill down to $N$-3 satellites, drill down to $N$-2 satellites, and drill down to $N$-1 satellites are shown in magenta in Figure A.9, in blue in Figure A.10, and in green in Figure A.11, respectively. The plot with drill down to four satellites is shown in red, and it is the same as the plot in Figure A.4. The maximum unbounded HPE, the largest HPE whose HPE-to-HPL ratio exceeds one, for drill down to four satellites is approximately 6 kilometers. The maximum unbounded HPE with drill down to $N$-3 satellites is 6 kilometers, the same as one with drill down to four satellites. Limited subset geometries with drill down to $N$-3 satellites do not mitigate the maximum unbounded HPE. The maximum unbounded HPE with drill down to $N$-2 satellites is approximately 110 meters, which is much smaller than 6 kilometers and should be acceptable for terminal area operations. The maximum unbounded HPE with drill down to $N$-1 satellites is approximately 70 meters, which is the smallest among four limited subset geometries proposed. However, limited subset geometries with drill down to $N$-1 satellites are not realistic when aircraft maneuvering in terminal area airspace (including banking) are considered. Therefore, drill down to $N$-2 satellites is considered as the proper limited subset geometry for DCPS to lower the maximum unbounded HPE.
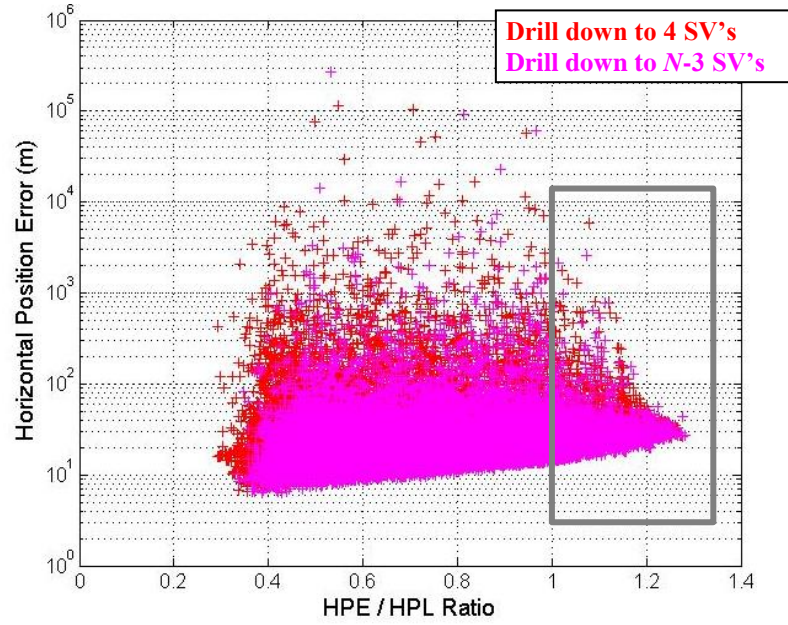
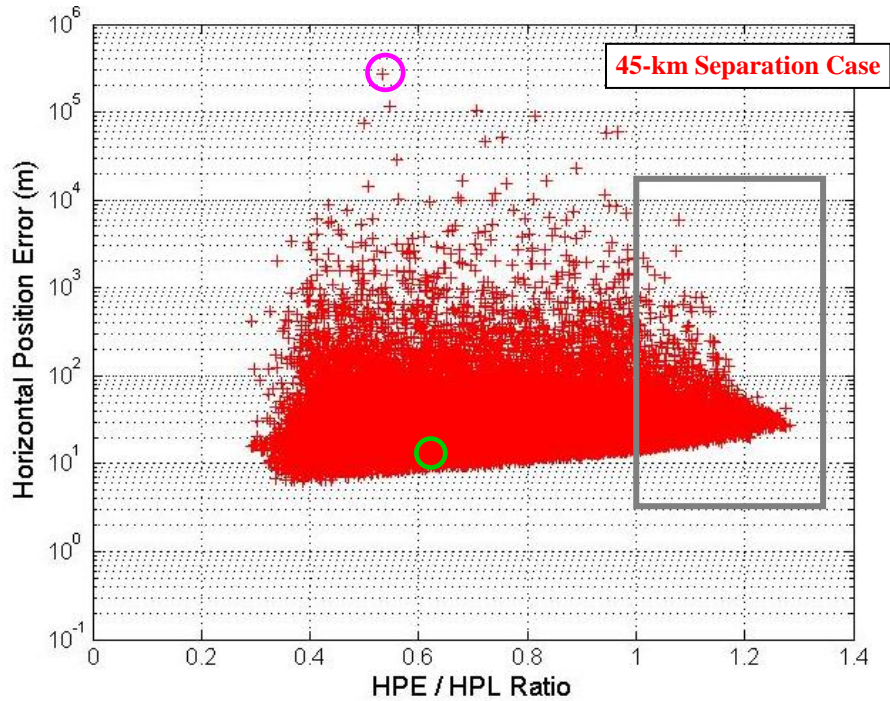Figure A.9. HPE versus HPE-to-HPL ratio plot of ionosphere anomaly impact on one SV with drill down to four SVs (red), and drill down to *N*-3 SVs (magenta) for 45-km separation case.
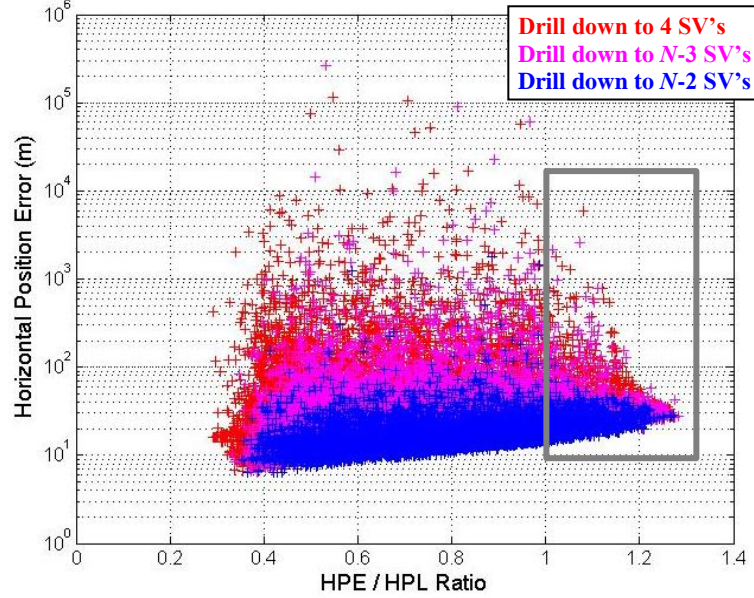


Figure A.10. HPE versus HPE-to-HPL ratio plot of ionosphere anomaly impact on one SV with drill down to four SVs (red), drill down to *N*-3 SVs (magenta), and drill down to *N*-2 SVs (blue) for 45-km separation case.
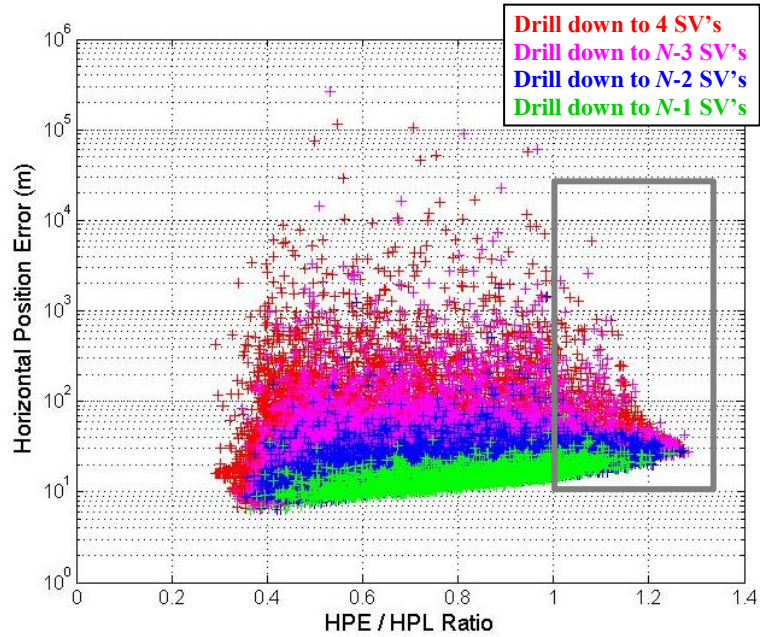
Figure A.11. HPE versus HPE-to-HPL ratio plot of ionosphere anomaly impact on one SV with drill down to four SVs (red), drill down to *N*-3 SVs (magenta), drill down to *N*-2 SVs (blue), and drill down to *N*-1 SVs (green) for 45-km separation case.

## A.5.3 SCREENING HAL

Figure A.12 and Figure A.13 show HPE versus HPL plots of the ionosphere anomaly impact on one SV with drill down to four satellites and drill down to *N*-2 satellites for the 45-km GBAS Ground Facility-to-user separation case, respectively. Drill down to four satellites is shown in red in these figures. If the maximum HPE that we allow for any DCPS application is assumed to be 300 meters, the screening HAL should be 250 meters as shown in Figure A.12. Drill down to *N*-2 satellites is shown in blue in Figure A.13, and the screening HAL should be 550 meters to allow the same 300 meters of maximum HPE as shown in Figure A.13. Here, it is confirmed that restricting subset geometries to no fewer than *N*-2 satellites allows DCPS users more flexible screening HAL values.
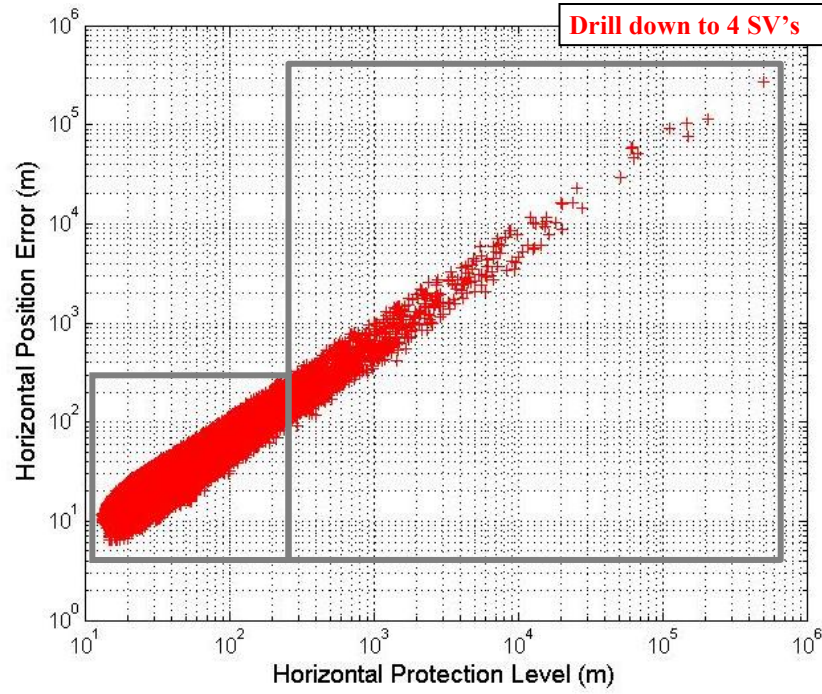
Figure A.12. HPE versus HPL plot of ionosphere anomaly impact on one SV with drill down to four SVs for 45-km separation case.
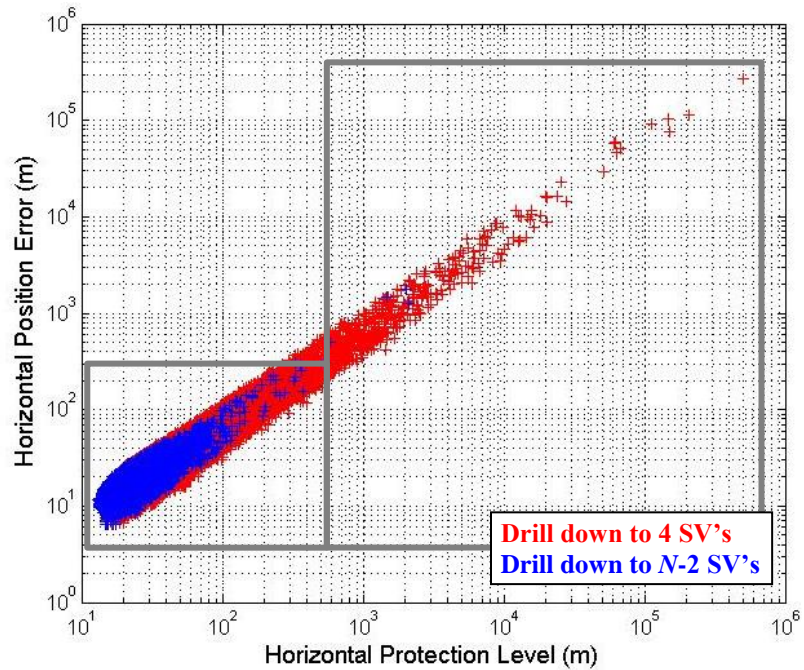


Figure A.13. HPE versus HPL plot of ionosphere anomaly impact on one SV with drill down to four SVs (red), and drill down to *N*-2 SVs (blue) for 45-km separation case.

# A.6 IONOSPHERIC ANOMALY IMPACT ON TWO SVs

The result of ionosphere anomaly impact on two satellites with drill down to four satellites for the 5-km GBAS Ground Facility-to-user separation case is shown in red in Figure A.14 and Figure A.15. The maximum unbounded HPE in the gray box is approximately 10 kilometers. When this result is compared to the result of the impact on one SV for the same case of limited geometries and GBAS Ground Facility-to-user separation in green in Figure A.15, it can be seen that ionosphere anomaly impact on one more satellite can pose a threat to DCPS users by producing much larger position error. Restricting subset geometries and applying a screening HAL would not help here. It shows that having the worst-case ionosphere impact to any pair of satellites (as was done for precision approach) cannot be supported by the changes to DCPS proposed in this dissertation.
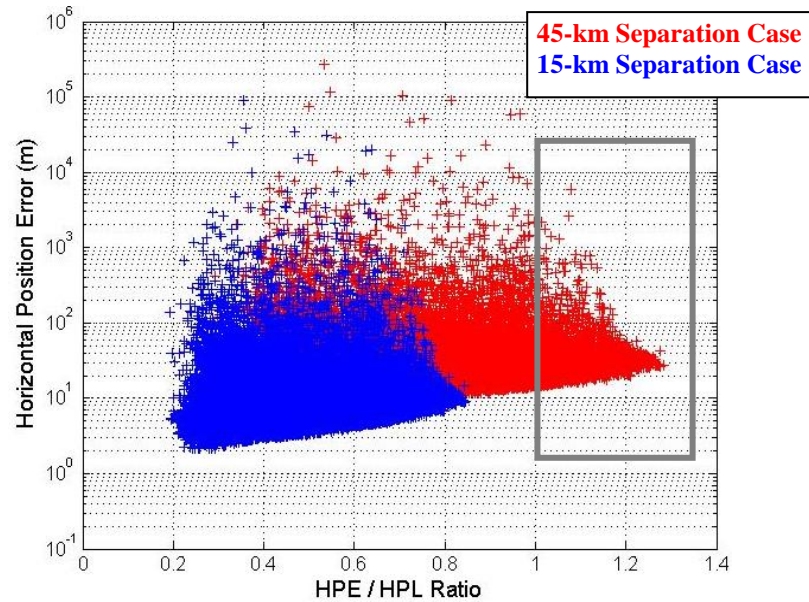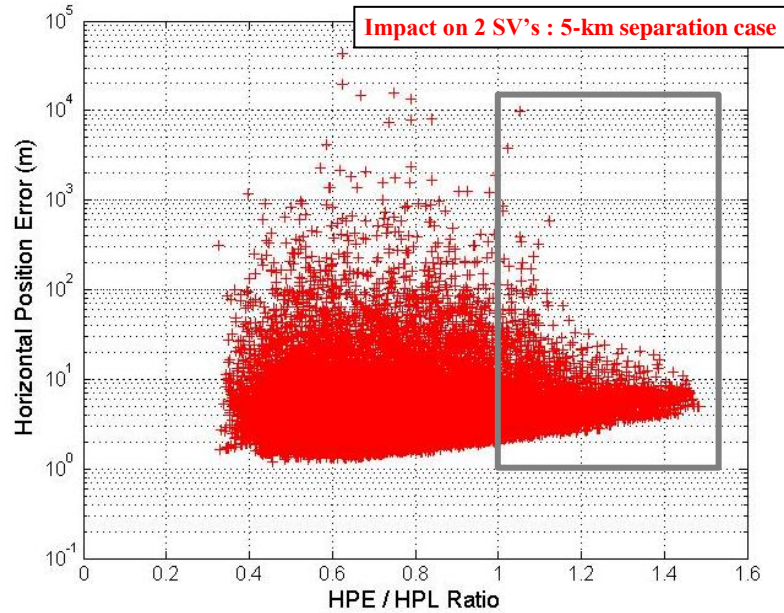


Figure A.14. HPE versus HPE-to-HPL ratio plot of ionosphere anomaly impact on two SVs with drill down to four SVs for 5-km separation case.

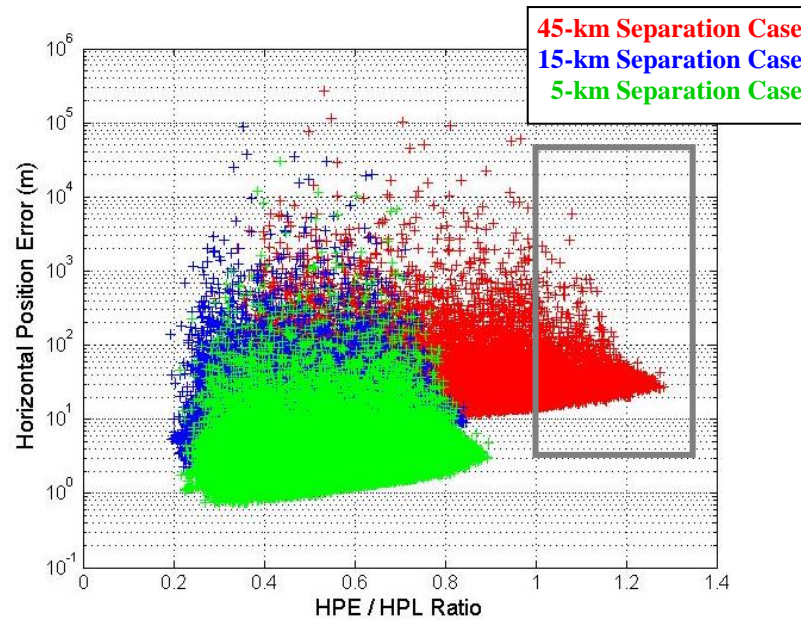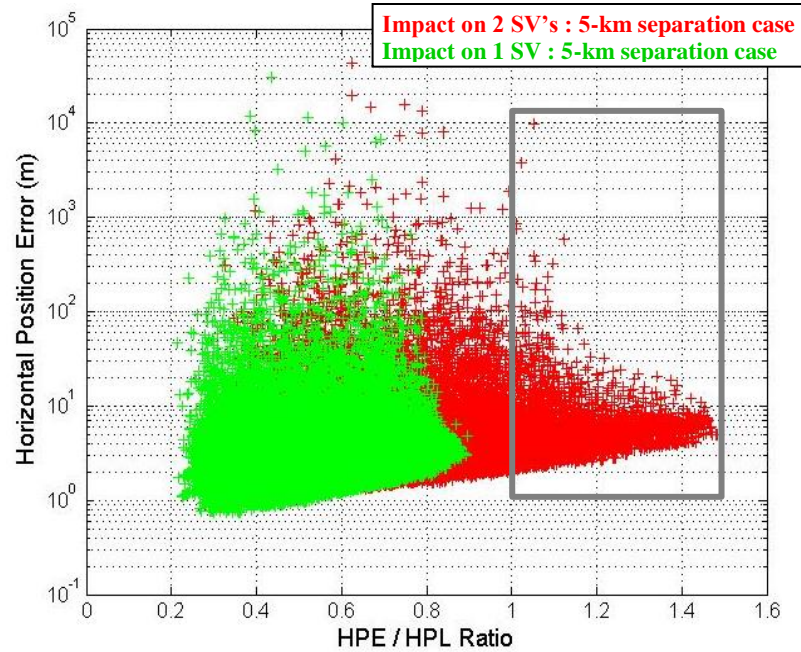Figure A.15. HPE versus HPE-to-HPL ratio plot of ionosphere anomaly impact on two SVs (red) and one SV (green) with drill down to four SVs for 5-km separation case.

# A.7 SUMMARY

DCPS will improve efficiency in terminal area operations and airport surface movement. This appendix shows the challenge to DCPS integrity posed by anomalous ionosphere. For one-satellite impact and 45-km GBAS Ground Facility-to-user separation case, the maximum unbounded HPE is 6 kilometers, and for two-satellite impact and 5-km GBAS Ground Facility-to-user separation case, the maximum unbounded HPE is 10 kilometers. One way to solve the difficulty explored in this appendix for the ionosphere anomaly impact on one satellite includes restricting airborne subset geometries to no smaller than two satellites unused out of the *N* provided by the ground system ("*N-2*"). In the one-satellite-impact case, this decreases the maximum unbounded HPE from 6 kilometers to 110 meters. This method also includes potential geometry screening using a screening HAL. For example, a screening HAL of 550 meters allows a maximum HPE of 300 meters

for the 45-km GBAS Ground Facility-to-user separation case with the limited subset of geometries drilled down to $N$-2 satellites (in the one-satellite-impact case).

# Appendix B

# ENABLING DCPS: DESIGN AND REQUIREMENT ALTERNATIVES

Appendix A demonstrated that the existing DCPS integrity requirements cannot be met by CAT I GBAS without changes to both the definition of DCPS integrity [FAA, 2002] [RCTA, 2004] and the airborne receiver requirements [RTCA, 2008]. This appendix goes beyond the previous appendix in identifying the changes that are required and recommending specific sets of alternatives. To support these decisions, this appendix defines specific quality metrics for DCPS analysis. One of these is the "Maximum Unprotected Error," or "MUE," which represents the largest error that is not guaranteed to be bounded by the Horizontal Protection Level (HPL) to the $10^{-7}$-per-hour probability level needed for DCPS integrity. This metric quantifies the level of error that DCPS users are allowed to have without violating a revised integrity requirement. The other metric is the projected availability of DCPS for the RTCA-standard 24-satellite constellation [RTCA,

2004] with all satellites healthy. In this appendix, "availability" represents not only the percentage of available geometries over time but also over all valid subset geometries (including the all-in-view geometry).

Because the results of Appendix A showed that having the worst-case ionosphere impact to any pair of satellites (as was done for precision approach) cannot be supported for DCPS, the DCPS error simulations carried out in this appendix limit the worst-case ionosphere impact to individual satellites. This represents one important but necessary change in the ionospheric anomaly threat model as applied to DCPS. Even with this change, the MUE is unacceptably high (roughly 6 kilometers at Memphis) with an effective ionospheric gradient sigma ($\sigma_{vig}$) of 24.1 millimeters per kilometer if no changes to the avionics requirements are made. MUE is even larger (about 350 kilometers) with the nominal $\sigma_{vig}$ of 4 millimeters per kilometer (see Appendix A for more details).

Therefore, this appendix examines various combinations of additional aircraft geometry screening and integrity monitoring. The objective is to minimize MUE so as to maximize the utility of DCPS while maintaining useful availability of the DCPS service. Two types of airborne geometry screening rules have been evaluated individually and in combination. The first rule limits airborne subset geometries by numbers of satellites used, and the second rule limits the maximum absolute value of the range-to-horizontal-position scalar, $|S_{horizontal}|$. In addition, RAIM is evaluated to obtain an additional reduction of MUE. Tables with results for the many alternatives tested are shown.

# B.1  AIRBORNE GEOMETRY SCREENING RULES

Two types of airborne geometry screening rules have been evaluated individually and in combination. These rules limit valid airborne geometries to (a) no more than $M$ satellites

fewer than the $N$ satellites approved by the GBAS Ground Facility, where $M \leq 2$ (this is helpful, since drill-down to three satellites out ($M = 3$) has the same MUE as including all usable subset geometries (down to four satellites), as demonstrated in Appendix A); and (b) specifying a maximum absolute value of the range-to-position scalar, $|S_{horizontal}|$, that is derived from the weighted pseudoinverse of the user's GPS geometry matrix [RCTA, 2008]. The limited subset geometry rule based on (a) was evaluated in Appendix A. The second screening rule alone based on (b) and in combination with the limited subset geometry rule is evaluated in this appendix. In addition, RAIM using the method in [Walter, 1995] is evaluated to obtain additional reduction of the MUE, although the additional benefit turns out to be relatively small.

# B.2 SIMULATION PROCEDURE

## B.2.1 DCPS SIMULATION OF HPE AND HPL

The simulation procedure used to analyze DCPS design and requirement alternatives has been expanded from the methodology in Appendix A and is shown in Figure B.1. One day of geometries with a five-degree mask angle and five-minute time updates from 11 major U.S. airports (including Memphis) is used to generate all-in-view, all one-satellite-out, all two-satellites-out, etc., down to all four-satellite subset geometries, where $N$ represents the number of visible satellites in the geometry (which are all assumed to be approved for use by the GBAS Ground Facility). The maximum supported distance from GBAS Ground Facility to user, defined as $D_{max}$ and included in the information broadcast by the VDB [RTCA, 2008], is nominally set to be 45 kilometers, although shorter maximum separations have also been evaluated.

Worst-case GPS range errors from the ionospheric anomaly threat model for the Conterminous U.S. (CONUS) [Pullen, 2009] are applied to all individual satellites in all allowed subset geometries, one satellite at a time. Anomalous ionospheric range errors

applied to individual satellites are proportional to the distance from GBAS Ground Facility to user with the addition of a bias due to an assumed aircraft velocity of 70 meters per second in the direction of the GBAS Ground Facility. This value is used because it is also used for CAT I precision approach, although the actual value for DCPS could be quite different. The nominal ionospheric gradient parameter, $\sigma_{vig}$, varies due to GBAS Ground Facility geometry screening to protect CAT I precision approach. Here, the nominal (uninflated) $\sigma_{vig}$ of 4 millimeters per kilometer is conservatively used for all screening rules and integrity monitoring. The computed Horizontal Position Error (HPE) and HPL are obtained, and the largest HPE and corresponding HPL are stored for each subset geometry.
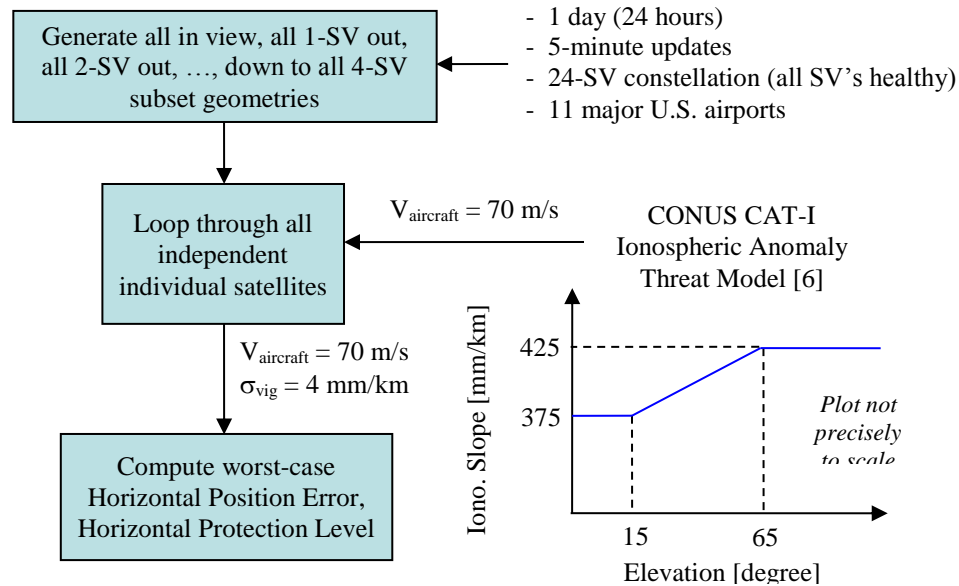
Figure B.1. DCPS Simulation procedure to obtain HPE and HPL.

Eleven (11) major U.S. airports are used to generate GPS satellite geometries: Memphis (MEM), Dulles (IAD), Atlanta (ATL), Chicago O'Hare (ORD), Los Angeles (LAX), Seattle-Tacoma (SEA), New York/John F. Kennedy (JFK), Minneapolis/St. Paul (MSP),

Dallas/Fort Worth (DFW), Salt Lake City (SLC), and Anchorage (ANC). These airports are shown in Figure B.2 and are well distributed throughout the U.S.
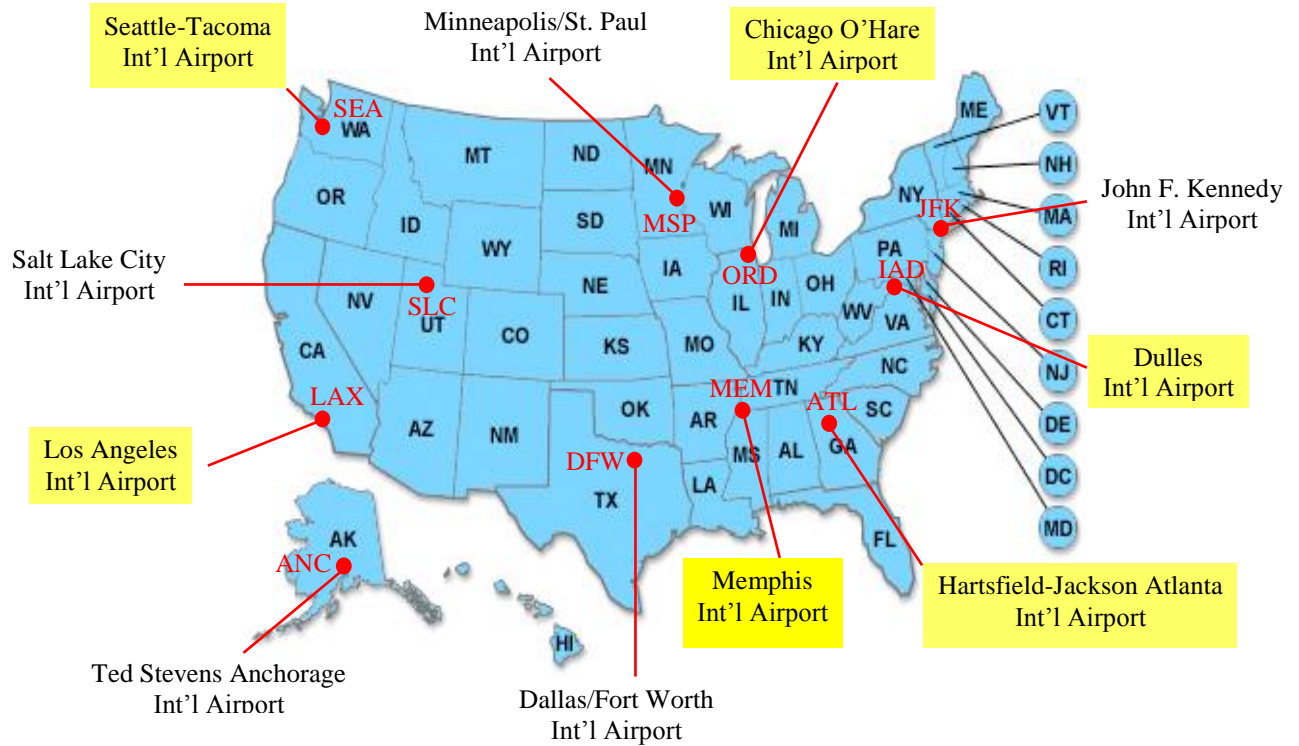


Figure B.2. Memphis international airport and ten other major U.S. airports on map of U.S. [USmap].

## B.2.2 GEOMETRY SCREENING SIMULATION

HPE and HPL calculated by the procedure shown in Figure B.1 are fed to the geometry screening simulation as inputs. Drill-down to four-satellite subset geometries is used for geometry screening based on the maximum $|S_{horizontal}|$ limitation rule only, and drill-down to $M$-satellite-out subset geometries is used for geometry screening based on combinations of the maximum $|S_{horizontal}|$ limitation and limited subset geometries, where $M$ is less than or equal to two. The geometries whose HPE is not bounded by their HPL (in other words,

the HPE-to-HPL ratio exceeds 1.0) are investigated to determine the maximum $|S_{horizontal}|$ needed to protect a certain MUE. Some geometries whose $|S_{horizontal}|$ is greater than the determined maximum $|S_{horizontal}|$ are screened out, and the surviving geometries contribute to DCPS availability. For the combinations of airborne geometry screening rules that include RAIM, the maximum $|S_{horizontal}|$ for geometries with five or more satellites is determined from the geometries that pass RAIM integrity monitoring for a certain MUE. Since RAIM cannot be used with only four satellites, the maximum $|S_{horizontal}|$ value from the combination of the other geometry screening rules is used for four-satellite geometries. RAIM thresholds are chosen to be values with a $10^{-4}$ probability of false alarm and are listed in Table 1 of [Walter, 1995]. A margin of 10% is applied to (i.e., subtracted from) the lowest value of maximum $|S_{horizontal}|$ from the several airports simulated to get one maximum $|S_{horizontal}|$ that should cover all airports.

# B.3 RESULTS AND DISCUSSION

This section presents the results of an example operation. The aircraft in question is making use of DCPS for terminal-area navigation while in the early stages of approach toward a GBAS-equipped airport and is able to receive the VDB while still 45 kilometers away. The aircraft is moving directly toward the airport with a horizontal velocity of 70 meters per second.

As noted in the introduction to this appendix, the MUE with no new screening (i.e., as per the current Minimum Operational Performance Standards (MOPS) avionics requirements) is approximately 6 kilometers at Memphis when an inflated (and near-maximum) value of 24.1 millimeters per kilometer is used for $\sigma_{vig}$ and the aircraft velocity in the direction of the GBAS Ground Facility is approximately zero.

In this appendix, using the nominal $\sigma_{vig}$ of 4 millimeters per kilometer, the MUE with no new screening (i.e., drill-down to four-satellite subset geometries) and with an assumed

aircraft velocity of 70 meters per second in the direction of the GBAS Ground Facility is approximately 350 kilometers at Memphis. The primary reason for this large increase in MUE is that the much lower value of nominal $\sigma_{vig}$ (compared to the maximum inflated value) greatly reduces HPL, while the worst-case error for each subset geometry remains unchanged.

Figure B.3 shows a plot of HPE versus the HPE-to-HPL ratio for various limited subset geometries. Note that all of the horizontal errors on the *y*-axis are significantly larger than the corresponding protection levels. Applying an *N*–2 airborne geometry screening rule, where *M* is 2 (meaning that the all-in-view, all 1-satellite-out, and all 2-satellites-out subset geometries (only) are considered in the simulation) reduces the MUE to approximately 2.4 kilometers with 99.9% DCPS availability. The MUE is reduced to 89 meters for the *M* = 1 constraint, and to 30 meters when the airborne geometry screening rule limits subset geometries to only all-in-view geometries. In these cases, MUE is the same as "maximum error", as all of these errors are unbounded.
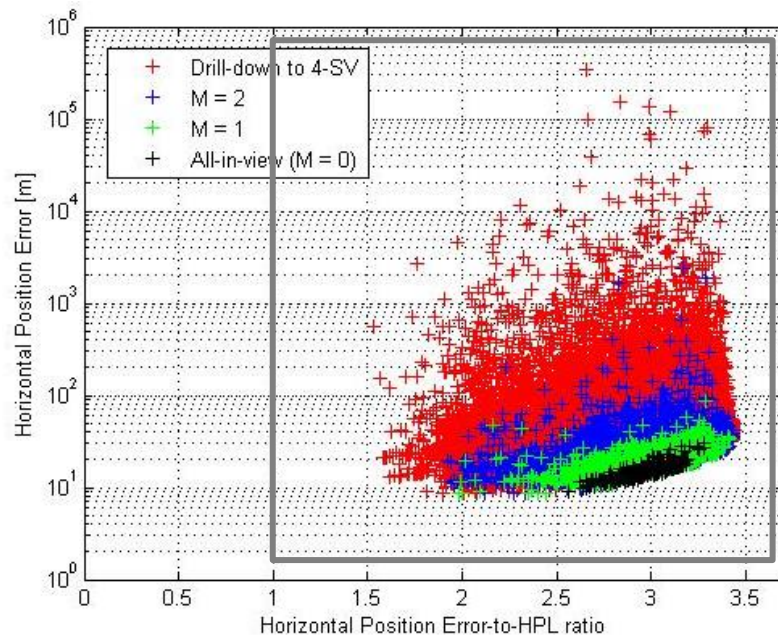


Figure B.3. HPE vs. HPE-to-HPL ratio for various limited subset geometries ($\sigma_{vig}$ = 4 mm/km).

## B.3.1 AIRBORNE GEOMETRY SCREENING BASED ON MAXIMUM $|S_{HORIZONTAL}|$ RULE ONLY

First, airborne geometry screening based on limiting the maximum $|S_{horizontal}|$ only is performed. Because the results from 11 U.S. major airports are similar in terms of availability and maximum $|S_{horizontal}|$, the results from Memphis only are shown in this section. The values of maximum $|S_{horizontal}|$ are determined using the drill-down to four-satellite subset geometries from Memphis only (with $\sigma_{vig} = 4$ mm/km). It gives an MUE of 150 meters with approximately 95% DCPS availability for a maximum $|S_{horizontal}|$ of approximately 6.0. Table B.1 lists several examples of maximum $|S_{horizontal}|$ and DCPS availability results for MUE values from 150 meters down to 10 meters. As expected, smaller MUE can be achieved with tighter bounds on $|S_{horizontal}|$ and a resulting loss in availability.

Table B.1. Max. $|S_{horizontal}|$, MUE, and DCPS availability at Memphis based on maximum $|S_{horizontal}|$ only

| Max. $|S_{horizontal}|$ | MUE (m) | DCPS Availability (%) |
|---|---|---|
| 6.01 | 150 | 95.31 |
| 5.63 | 140 | 94.99 |
| 5.19 | 130 | 94.53 |
| 4.80 | 120 | 94.01 |
| 4.44 | 110 | 93.40 |
| 4.00 | 100 | 92.50 |
| 3.59 | 90 | 91.27 |
| 3.20 | 80 | 89.83 |
| 2.79 | 70 | 87.78 |
| 2.39 | 60 | 84.52 |
| 2.00 | 50 | 78.64 |
| 1.60 | 40 | 68.41 |
| 1.20 | 30 | 51.20 |
| 0.82 | 20 | 22.24 |
| 0.42 | 10 | 0.052 |

The relationship between maximum $|S_{horizontal}|$ and MUE is shown in Figure B.4. Reducing the limit on maximum $|S_{horizontal}|$ reduces MUE almost linearly, and this limit can be reduced to the vicinity of 3.2, giving a MUE of approximately 80 meters while maintaining an availability of approximately 90 percent. Recall that "availability" in this context includes all subset geometries down to four-satellite cases. If availability were instead computed presuming that the aircraft always applied the all-in-view geometry, as is normally done for other applications, the availability would be much higher.
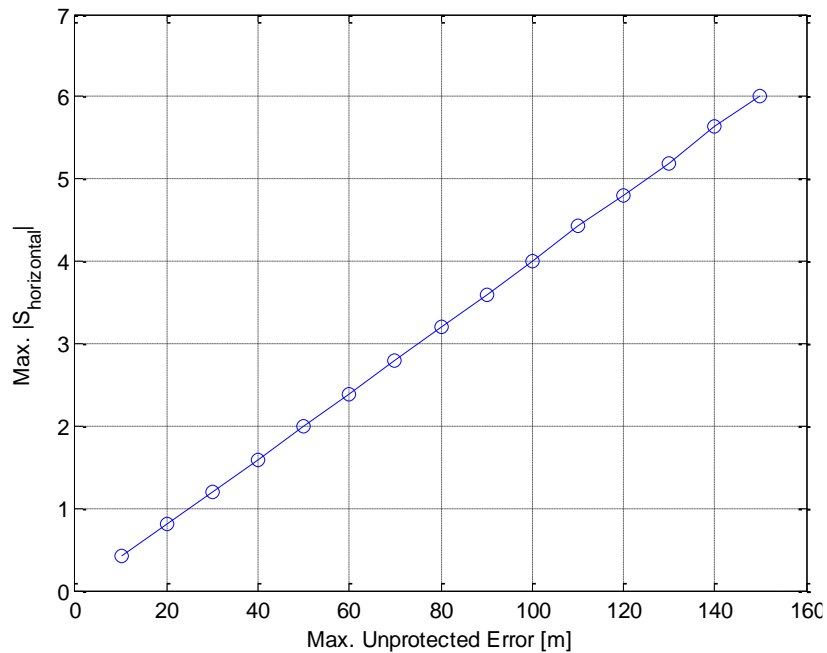


Figure B.4. Linearity of maximum $|S_{horizontal}|$ and MUE: Drill-down to four-satellite subset geometries at Memphis.

Note that an MUE of approximately 90 meters, which is supported with 99.9% DCPS availability by applying the limited subset geometry rule ($M = 1$) alone, can be achieved with approximately 91.3% DCPS availability by applying the maximum $|S_{horizontal}|$ rule alone (with a maximum $|S_{horizontal}|$ of 3.59). It makes sense to combine these two screening approaches in an attempt to lower MUE further while maintaining acceptable availability

without unduly constraining aircraft subset geometries. The results of this combined approach are shown in the next section.

## B.3.2 COMBINATIONS OF AIRBORNE GEOMETRY SCREENING RULES

Three versions of the limited subset geometry rule are considered for combination with the maximum $|S_{horizontal}|$ rule. These options limit subset geometries to the all-in-view geometry only, to all-in-view plus all one-satellite-out subsets, and all-in-view, all one-satellite-out, plus all two-satellites-out subsets, respectively. All subset geometries must have at least four satellites. For this section, the six airports highlighted in yellow in Figure B.2 are evaluated. It should be noted again that the nominal $\sigma_{vig}$ of 4 mm/km is used to evaluate these combinations. When the nominal or minimum value of $\sigma_{vig}$ is broadcast, many more (sometimes most or all) subset geometries have HPE exceeding HPL. Therefore, as with precision approach [Pullen, 2009], the primary impact of geometry screening is to lower the maximum HPE for all available subset geometries below MUE. Thus, even though HPE remains unbounded by HPL, these geometries will be acceptable under the proposed revised definition of DCPS integrity.

The maximum $|S_{horizontal}|$ values at these six airports for MUE values from 100 meters to 10 meters are listed in Table B.2 for the maximum $|S_{horizontal}|$ rule combined with a constraint on subset geometries of $M = 2$, meaning that only subset geometries with two or fewer satellites missing from the all-in-view geometry are allowed.

Note that the maximum $|S_{horizontal}|$ over the six airports, with 10% margin subtracted to cover airports not simulated here, is given in the far-right-hand column and is used to screen out unprotected geometries for all six airports.

Table B.2. Max. $|S_{horizontal}|$ when combined with $N$-2 subset geometry limitation at six major U.S. airports

| MUE (m) | MEM | IAD | ATL | ORD | LAX | SEA | 10% Margin |
|---------|-----|-----|-----|-----|-----|-----|------------|
| 100 | 4.13 | 4.20 | 4.10 | 4.05 | 4.07 | 4.06 | 3.65 |
| 90 | 3.68 | 3.67 | 3.69 | 3.74 | 3.62 | 3.67 | 3.26 |
| 80 | 3.41 | 3.28 | 3.26 | 3.26 | 3.25 | 3.21 | 2.89 |
| 70 | 2.81 | 2.82 | 2.89 | 2.81 | 2.84 | 2.83 | 2.53 |
| 60 | 2.42 | 2.42 | 2.40 | 2.40 | 2.42 | 2.43 | 2.16 |
| 50 | 2.00 | 2.00 | 2.01 | 2.01 | 2.01 | 2.02 | 1.80 |
| 40 | 1.60 | 1.60 | 1.61 | 1.60 | 1.60 | 1.61 | 1.44 |
| 30 | 1.20 | 1.20 | 1.20 | 1.20 | 1.20 | 1.20 | 1.08 |
| 20 | 0.80 | 0.80 | 0.80 | 0.80 | 0.80 | 0.80 | 0.72 |
| 10 | 0.41 | 0.41 | 0.42 | 0.43 | 0.42 | 0.42 | 0.37 |

The resulting availability for all three combinations of the maximum $|S_{horizontal}|$ rule and subset geometry constraints ($M = 0$, 1, and 2) are shown in Table B.3, Table B.4, and Table B.5, respectively. It is noted that DCPS availability at the six different airports is quite similar. When the $M = 0$ constraint is applied, an MUE of 25 meters is achieved with approximately 95% availability. For $M = 1$, the MUE can be reduced to 35 meters with availability greater than 95%. Unfortunately, because typical aircraft maneuvers may occasionally cause tracking of one satellite to be lost, and other causes may remove a second satellite from use, the $M = 2$ constraint is by far the most robust of these options for practical use. As Table B.5 shows, an MUE of 50 meters can be supported with 95% or better availability in this case.

Table B.3. DCPS availability (%) for Max. $|S_{horizontal}|$ with $M = 0$ subset geometry constraint

| MUE (m) | MEM | IAD | ATL | ORD | LAX | SEA |
|---------|-------|-------|-------|-------|-------|-------|
| 100 | 100 | 100 | 100 | 100 | 100 | 100 |
| 90 | 100 | 100 | 100 | 100 | 100 | 100 |
| 80 | 100 | 100 | 100 | 100 | 100 | 100 |
| 70 | 100 | 100 | 100 | 100 | 100 | 100 |
| 60 | 100 | 100 | 100 | 100 | 100 | 100 |
| 50 | 100 | 100 | 100 | 100 | 100 | 100 |
| 40 | 100 | 100 | 100 | 100 | 100 | 100 |
| 30 | 98.61 | 98.96 | 98.61 | 99.65 | 100 | 98.61 |
| 25 | 96.18 | 93.06 | 94.79 | 95.83 | 94.10 | 94.10 |
| 20 | 74.65 | 70.83 | 73.26 | 78.47 | 77.43 | 79.17 |
| 10 | 0.35 | 0.00 | 0.00 | 0.00 | 0.69 | 0.00 |

Table B.4. DCPS availability (%) for Max. $|S_{horizontal}|$ with $M = 1$ subset geometry constraint

| MUE (m) | MEM | IAD | ATL | ORD | LAX | SEA |
|---------|-------|-------|-------|-------|-------|-------|
| 100 | 100 | 100 | 100 | 100 | 100 | 100 |
| 90 | 100 | 100 | 100 | 100 | 100 | 100 |
| 80 | 99.96 | 100 | 100 | 100 | 100 | 100 |
| 70 | 99.96 | 100 | 100 | 99.92 | 100 | 100 |
| 60 | 99.92 | 100 | 99.96 | 99.88 | 99.92 | 100 |
| 50 | 99.59 | 99.80 | 99.63 | 99.60 | 99.68 | 99.76 |
| 40 | 98.90 | 98.37 | 98.70 | 98.13 | 98.88 | 98.12 |
| 35 | 96.38 | 94.99 | 95.86 | 96.67 | 97.47 | 95.59 |
| 30 | 90.15 | 89.16 | 89.40 | 91.48 | 91.44 | 90.02 |
| 20 | 46.15 | 44.58 | 43.77 | 47.77 | 55.72 | 52.52 |
| 10 | 0.00 | 0.00 | 0.00 | 0.00 | 0.00 | 0.00 |

Table B.5. DCPS availability (%) for Max. $|S_{horizontal}|$ with $M = 2$ subset geometry constraint

| MUE (m) | MEM | IAD | ATL | ORD | LAX | SEA |
|---------|-------|-------|-------|-------|-------|-------|
| 100 | 99.35 | 99.22 | 99.21 | 99.38 | 99.12 | 99.43 |
| 90 | 99.20 | 99.02 | 99.07 | 99.18 | 98.95 | 99.22 |
| 80 | 98.98 | 98.74 | 98.78 | 99.00 | 98.70 | 98.85 |
| 70 | 98.46 | 98.22 | 98.45 | 98.63 | 98.20 | 98.51 |
| 60 | 97.54 | 97.12 | 97.51 | 97.63 | 97.39 | 97.82 |
| 50 | 95.64 | 95.16 | 95.47 | 95.53 | 95.83 | 96.01 |
| 40 | 90.55 | 88.70 | 90.07 | 89.65 | 91.88 | 90.73 |
| 30 | 73.51 | 71.35 | 72.76 | 73.80 | 77.82 | 75.34 |
| 20 | 28.38 | 27.58 | 27.13 | 27.20 | 36.34 | 32.21 |
| 10 | 0.00 | 0.00 | 0.00 | 0.00 | 0.00 | 0.00 |

## B.3.3 RAIM WITH COMBINATIONS OF AIRBORNE GEOMETRY SCREENING RESULTS

RAIM is evaluated in addition to the geometry screening rules shown above because it may already be present in many aircraft that will make use of GBAS DCPS. The addition of RAIM monitoring of large anomalous ionosphere-induced ranging errors helps relax the maximum $|S_{horizontal}|$ so that better availability can be obtained for the same MUE. The simulation procedure to obtain the maximum $|S_{horizontal}|$ values is different from the previous section because RAIM is added, as described in Section B.2, while the other algorithms remain the same.

Maximum $|S_{horizontal}|$ values for geometries with five or more satellites for the combination of the maximum $|S_{horizontal}|$ rule and the drill-down to two-satellites-out ($M = 2$) rule with RAIM are listed in Table B.6. Here, some maximum $|S_{horizontal}|$ values are infinite ($\infty$) because no $|S_{horizontal}|$ constraint is needed. This occurs when no horizontal errors exist that exceed HPL or when all such cases are detected by RAIM. RAIM can be used only when the number of satellites in the geometry is at least five. Therefore, maximum $|S_{horizontal}|$ values determined from combinations of the geometry screening rules without RAIM (derived in the previous section) are used for four-satellite geometries.

Table B.6. Max. $|S_{horizontal}|$ with RAIM when $N \geq 5$, $M = 2$ at six major U.S. airports

| MUE (m) | MEM | IAD | ATL | ORD | LAX | SEA | 10% Margin |
|---------|-----|-----|-----|-----|-----|-----|------------|
| 100 | 4.13 | 4.79 | 4.32 | 4.44 | $\infty$ | 4.10 | 3.69 |
| 90 | 3.89 | 3.84 | 4.32 | 4.44 | $\infty$ | 4.10 | 3.46 |
| 80 | 3.67 | 3.71 | 4.32 | 3.26 | 3.25 | 4.10 | 2.92 |
| 70 | 3.58 | 3.00 | 3.27 | 2.85 | 3.25 | 2.97 | 2.57 |
| 60 | 2.60 | 2.53 | 2.63 | 2.63 | 2.42 | 2.47 | 2.18 |
| 50 | 2.05 | 2.07 | 2.01 | 2.07 | 2.02 | 2.09 | 1.81 |
| 40 | 1.61 | 1.60 | 1.65 | 1.66 | 1.64 | 1.62 | 1.44 |
| 30 | 1.23 | 1.23 | 1.21 | 1.22 | 1.21 | 1.21 | 1.09 |
| 20 | 0.83 | 0.83 | 0.85 | 0.80 | 0.83 | 0.88 | 0.72 |
| 10 | 0.58 | 0.56 | 0.63 | 0.59 | 0.70 | 0.59 | 0.50 |

In the same manner as the previous section, DCPS availabilities at six airports when RAIM is added to combinations of maximum $|S_{horizontal}|$ and limited subset geometries with $M = 0$, 1, and 2 are shown in Table B.7, Table B.8, and Table B.9, respectively. Maintaining approximately 95% availability allows MUE to be reduced to below 10 meters for $M = 0$ (see below), 35 meters for $M = 1$, and 50 meters for $M = 2$. Note that the only significant improvement from the results in Section 4.2 is for $M = 0$ (i.e., use of only the all-in-view geometry). In this case, Table B.7 shows that 100% availability is achieved even for an MUE of 10 meters. This is because all errors generated using all-in-view geometries are either bounded by HPL or do not pass RAIM. Therefore, in this unique case, even an MUE of zero meters allows 100 percent DCPS availability, which is another way of saying that the existing DCPS integrity requirement (in which HPL always bounds HPE) can be met for this scenario.

Table B.7. DCPS availability (%) for RAIM with Max. $|S_{horizontal}|$ and $M = 0$ subset geometry constraint

| MUE (m) | MEM | IAD | ATL | ORD | LAX | SEA |
|---------|-----|-----|-----|-----|-----|-----|
| 100 | 100 | 100 | 100 | 100 | 100 | 100 |
| 90 | 100 | 100 | 100 | 100 | 100 | 100 |
| 80 | 100 | 100 | 100 | 100 | 100 | 100 |
| 70 | 100 | 100 | 100 | 100 | 100 | 100 |
| 60 | 100 | 100 | 100 | 100 | 100 | 100 |
| 50 | 100 | 100 | 100 | 100 | 100 | 100 |
| 40 | 100 | 100 | 100 | 100 | 100 | 100 |
| 30 | 100 | 100 | 100 | 100 | 100 | 100 |
| 20 | 100 | 100 | 100 | 100 | 100 | 100 |
| 10 | 100 | 100 | 100 | 100 | 100 | 100 |

Table B.8. DCPS availability (%) for RAIM with Max. $|S_{horizontal}|$ and $M = 1$ subset geometry constraint

| MUE (m) | MEM | IAD | ATL | ORD | LAX | SEA |
|---|---|---|---|---|---|---|
| 100 | 100 | 100 | 100 | 100 | 100 | 100 |
| 90 | 100 | 100 | 100 | 100 | 100 | 100 |
| 80 | 99.96 | 100 | 100 | 100 | 100 | 100 |
| 70 | 99.96 | 100 | 100 | 100 | 100 | 100 |
| 60 | 99.96 | 100 | 100 | 100 | 100 | 100 |
| 50 | 99.59 | 99.80 | 99.63 | 99.59 | 99.68 | 99.76 |
| 40 | 98.94 | 98.86 | 99.07 | 98.58 | 99.00 | 98.56 |
| 35 | 96.83 | 95.84 | 96.47 | 97.08 | 97.91 | 96.27 |
| 30 | 90.56 | 89.57 | 89.97 | 91.84 | 91.88 | 90.55 |
| 20 | 59.87 | 57.21 | 58.22 | 60.35 | 66.01 | 64.62 |
| 10 | 14.69 | 14.02 | 14.33 | 13.43 | 23.42 | 18.47 |

Table B.9. DCPS availability (%) for RAIM with Max. $|S_{horizontal}|$ and M = 2 subset geometry constraint

| MUE (m) | MEM | IAD | ATL | ORD | LAX | SEA |
|---|---|---|---|---|---|---|
| 100 | 99.37 | 99.22 | 99.24 | 99.38 | 99.12 | 99.44 |
| 90 | 99.25 | 99.01 | 99.12 | 99.28 | 99.01 | 99.29 |
| 80 | 99.00 | 98.77 | 98.80 | 99.01 | 98.74 | 98.85 |
| 70 | 98.51 | 98.26 | 98.46 | 98.68 | 98.23 | 98.56 |
| 60 | 97.58 | 97.22 | 97.57 | 97.68 | 97.43 | 97.88 |
| 50 | 95.70 | 95.21 | 95.55 | 95.63 | 95.88 | 96.19 |
| 40 | 90.68 | 88.83 | 90.16 | 89.76 | 91.96 | 90.80 |
| 30 | 74.12 | 72.19 | 73.52 | 74.68 | 78.45 | 76.06 |
| 20 | 28.54 | 27.83 | 27.25 | 27.37 | 36.58 | 32.38 |
| 10 | 1.58 | 1.67 | 1.11 | 0.82 | 3.18 | 1.93 |

In order to better visualize the improvement in DCPS availability that can be achieved by adding RAIM, the availability for combinations of the screening rules alone and with RAIM are compared in Figure B.5 for $M = 0$, in Figure B.6 for $M = 1$, and in Figure B.7 for $M = 2$. Overall, RAIM appears to be helpful in reducing MUE for the same availability when MUE is less than 30 meters and when subset geometries are limited to fewer satellites missing.
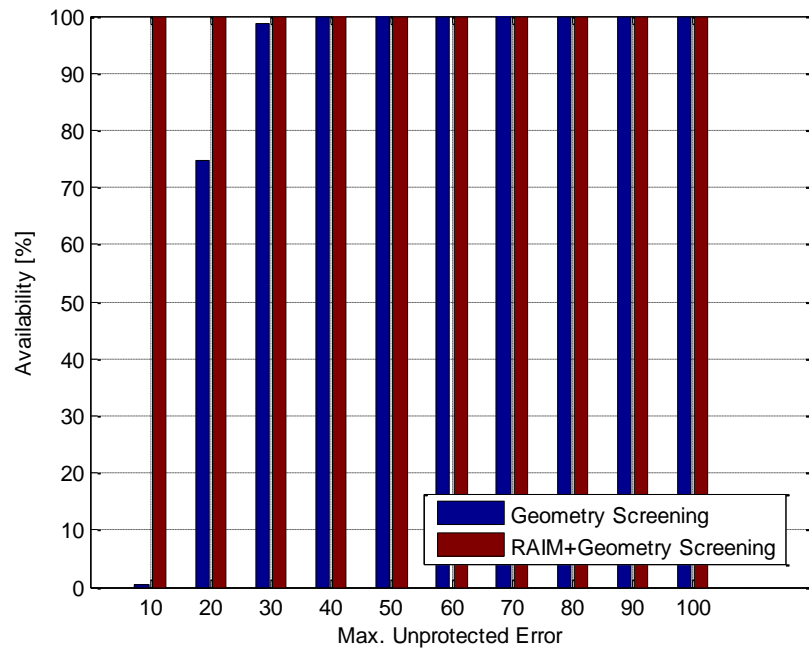


Figure B.5. Comparison of DCPS availability between airborne geometry screening alone and with RAIM: Memphis; $M = 0$.
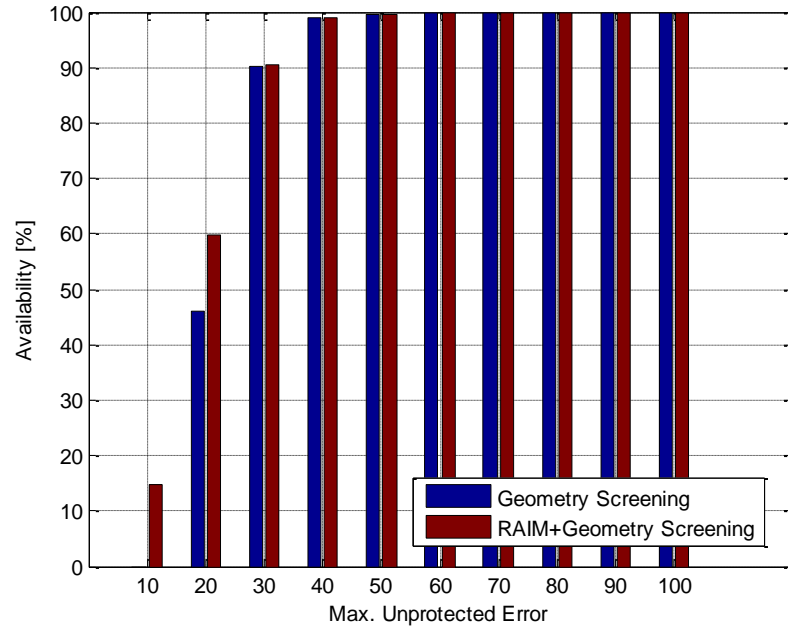
Figure B.6. Comparison of DCPS availability between airborne geometry screening alone and with RAIM: Memphis; $M = 1$.
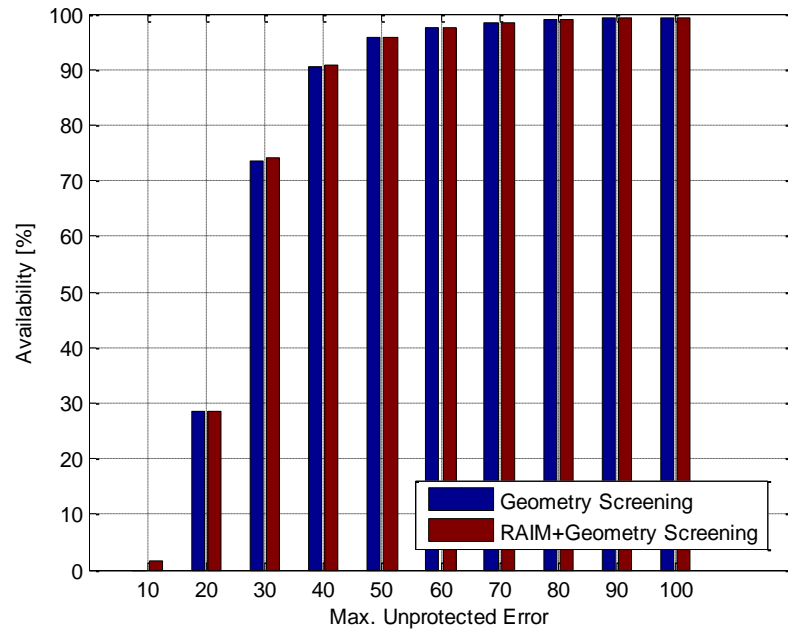


Figure B.7. Comparison of DCPS availability between airborne geometry screening alone and with RAIM: Memphis; $M = 2$.

# B.4  SUMMARY

## B.4.1 SUMMARY OF RESULTS

To encapsulate the results in this appendix, the smallest achievable MUEs with more than 95% DCPS availability with a 24-satellite GPS constellation at Memphis, categorized by airborne geometry screening rules and the presence of RAIM, are summarized in Table B.10.

Table B.10. Summary of MUE with 95 % availability: 24-SV GPS Constellation at Memphis; $D_{max} = 45$ km; $\sigma_{vig} = 4$ mm/km; one SV impacted by CONUS ionosphere threat model

| Airborne Implementation | | MUE | Availability (24 Healthy SV's) |
|---|---|---|---|
| No new screening | | ~ 350 km | > 99.9 % |
| Screening based on 2-satellites-out ($M = 2$) rule only | | 2.4 km | > 99.9 % |
| Screening based on max. $|S_{horizontal}|$ only | | 140 m (max. $|S_{horizontal}| = 5.6$) | 95.0 % |
| Combinations of $M$ satellite out and max. $|S_{horizontal}|$ | $M = 0$ | 25 m | 96.2 % |
| | $M = 1$ | 35 m | 96.4 % |
| | $M = 2$ | 50 m | 95.6 % |
| RAIM with screening | $M = 0$ | 0 m | > 99.9 % |
| | $M = 1$ | 35 m | 96.8 % |
| | $M = 2$ | 50 m | 95.7 % |

## B.4.2 CONCLUSIONS

Six key conclusions have been drawn from the DCPS analyses conducted in this appendix:

(1) Changes to both the DCPS integrity requirements definition and the requirements on GBAS avionics are needed to make DCPS usable.

(2) A change to the impact component of the CONUS GBAS ionospheric anomaly threat model, from two-satellite to one-satellite impact, is necessary when this threat model is applied to DCPS.

(3) Once a non-zero value of MUE is allowed by the DCPS integrity requirement, the use of multiple screening rules and, optionally, the use of RAIM for DCPS makes it possible to achieve an MUE for DCPS of about 50 meters (for $D_{max}$ = 45 km) with approximately 95% availability. Further significant reductions do not appear to be possible unless the maximum-gradient bound in the ionospheric anomaly threat model is reduced significantly. However, defining availability more conventionally, in terms of the all-in-view geometries only, would result in significantly lower MUE values at 95% availability.

(4) Because performance differences among the most-helpful options are relatively small, there does not appear to be one clearly "best" choice of additional airborne screening and monitoring. Therefore, the optimal selection depends highly on the specific flight and ground operations to be supported by DCPS and the constraints imposed by existing GBAS airborne equipment.

(5) Because of (3), some future applications of GBAS that planned to use DCPS but would require MUE values of 10 meters or below, such as airport surface movement, may not be supported by DCPS with the CAT I GBAS architecture.

(6) The single-frequency CAT-III GBAS architecture now under development (see [RTCA, 2004] [Lee, 2006]) will improve DCPS performance by introducing airborne

ionospheric gradient monitoring in addition to airborne geometry screening. However, the additional requirement changes identified in this appendix will still be necessary.

Conclusion (5) suggests one important further change to the GBAS avionics requirements. The current LAAS MOPS forbids use of the GBAS Position/Velocity/Timing (PVT) outputs if DCPS is not enabled by the GBAS Ground Facility [RTCA, 2008]. As this appendix points out, even if DCPS is enabled, it will not support all applications that can make use of the PVT outputs. Therefore, the PVT outputs should be "de-linked" from DCPS so that they can be used independently. PVT applications that cannot be supported by DCPS should be defined as separate applications of GBAS in the same manner as precision approach. We suspect that, if airport surface movement is defined as a separate operation, it can probably be supported by the existing GBAS Ground Facility geometry screening that mitigates the ionosphere-anomaly threat for CAT I precision approach. Confirming this hypothesis requires a more-intensive study of the requirements on airport surface movement and is the subject of Chapter 4.

# Appendix C

# SURFACE MOVEMENT AVAILABILITY AND SENSITIVITY

Table C.1. Availability with additional geometry screening: no sigma inflation

| MAE (m) | GGF[b]-to-User Separation (km) | Rule 1: Screening HAL | | | Rule 2: Maximum $|S_{horizontal}|$ | | |
|---|---|---|---|---|---|---|---|
| | | Screening HAL (m) | Availability for all-in-view geometries (%) | Availability for N-1 geometries (%) | Max. $|S_{horizontal}|$ | Availability for all-in-view geometries (%) | Availability for N-1 geometries (%) |
| 3 | 1 | N/A[a] | 100 | 95.08 | N/A | 100 | 95.08 |
| | 2 | N/A | 100 | 94.75 | N/A | 100 | 94.75 |
| | 3 | 2.85 | 100 | 91.09 | 1.43 | 100 | 94.38 |
| | 4 | 2.48 | 96.18 | 79.57 | 1.18 | 99.65 | 91.45 |
| | 5 | 2.23 | 91.32 | 64.31 | 1.01 | 97.22 | 85.92 |

| MAE (m) | GGF[b]-to-User Separation (km) | Rule 1: Screening HAL | | | Rule 2: Maximum $|S_{horizontal}|$ | | |
|---|---|---|---|---|---|---|---|
| | | *Screening HAL (m)* | *Availability for all-in-view geometries (%)* | *Availability for N-1 geometries (%)* | *Max. $|S_{horizontal}|$* | *Availability for all-in-view geometries (%)* | *Availability for N-1 geometries (%)* |
| | 6 | 2.02 | 76.39 | 38.26 | 0.89 | 94.79 | 76.68 |
| 4 | 1 | N/A | 100 | 99.10 | N/A | 100 | 99.10 |
| | 2 | N/A | 100 | 99.06 | N/A | 100 | 99.06 |
| | 3 | 3.88 | 100 | 98.82 | 1.89 | 100 | 98.94 |
| | 4 | 3.25 | 100 | 96.30 | 1.57 | 100 | 98.66 |
| | 5 | 2.78 | 100 | 87.63 | 1.35 | 100 | 97.48 |
| | 6 | 2.59 | 96.53 | 80.50 | 1.18 | 99.65 | 94.02 |
| 5 | 1 | N/A | 100 | 99.67 | N/A | 100 | 99.67 |
| | 2 | N/A | 100 | 99.64 | N/A | 100 | 99.63 |
| | 3 | 4.98 | 100 | 99.64 | 2.37 | 100 | 99.63 |
| | 4 | 4.10 | 100 | 99.06 | 1.96 | 100 | 99.59 |
| | 5 | 3.42 | 100 | 97.03 | 1.68 | 100 | 99.43 |
| | 6 | 3.20 | 100 | 94.99 | 1.47 | 100 | 98.94 |
| 7.5 | 1 | N/A | 100 | 99.88 | N/A | 100 | 99.88 |
| | 2 | N/A | 100 | 99.88 | N/A | 100 | 99.88 |
| | 3 | N/A | 100 | 99.88 | N/A | 100 | 99.88 |
| | 4 | 6.10 | 100 | 99.84 | 2.95 | 100 | 99.88 |
| | 5 | 5.53 | 100 | 99.72 | 2.53 | 100 | 99.88 |
| | 6 | 4.83 | 100 | 99.59 | 2.21 | 100 | 99.80 |
| 10 | 1 | N/A | 100 | 99.96 | N/A | 100 | 99.96 |
| | 2 | N/A | 100 | 99.96 | N/A | 100 | 99.96 |
| | 3 | N/A | 100 | 99.96 | N/A | 100 | 99.96 |
| | 4 | 8.66 | 100 | 99.92 | 3.92 | 100 | 99.96 |
| | 5 | 7.49 | 100 | 99.88 | 3.36 | 100 | 99.92 |
| | 6 | 6.48 | 100 | 99.84 | 2.95 | 100 | 99.92 |
| 15 | 1 | N/A | 100 | 100 | N/A | 100 | 100 |
| | 2 | N/A | 100 | 100 | N/A | 100 | 100 |
| | 3 | N/A | 100 | 100 | N/A | 100 | 100 |
| | 4 | 13.46 | 100 | 100 | 5.89 | 100 | 100 |
| | 5 | 11.23 | 100 | 100 | 5.06 | 100 | 100 |

| MAE (m) | GGF[b]-to-User Separation (km) | Rule 1: Screening HAL | | | Rule 2: Maximum $\|S_{horizontal}\|$ | | |
|---|---|---|---|---|---|---|---|
| | | *Screening HAL (m)* | *Availability for all-in-view geometries (%)* | *Availability for N-1 geometries (%)* | *Max. $\|S_{horizontal}\|$* | *Availability for all-in-view geometries (%)* | *Availability for N-1 geometries (%)* |
| | 6 | 10.26 | 100 | 99.96 | 4.43 | 100 | 100 |
| 20 | 1 | N/A | 100 | 100 | N/A | 100 | 100 |
| | 2 | N/A | 100 | 100 | N/A | 100 | 100 |
| | 3 | N/A | 100 | 100 | N/A | 100 | 100 |
| | 4 | 17.55 | 100 | 100 | 7.89 | 100 | 100 |
| | 5 | 15.77 | 100 | 100 | 6.77 | 100 | 100 |
| | 6 | 13.83 | 100 | 100 | 5.89 | 100 | 100 |

a. "N/A" means no additional geometry restriction. b. GGF = GBAS Ground Facility.

Table C.2. Availability with additional geometry screening: inflated $\sigma_{vig}$ and no inflation of aircraft $\sigma_{pr\_air}$

| MAE (m) | GGF-to-User Separation (km) | Rule 1: Screening HAL | | | Rule 2: Maximum $|S_{horizontal}|$ | | |
|---|---|---|---|---|---|---|---|
| | | *Screening HAL (m)* | *Availability for all-in-view geometries (%)* | *Availability for N-1 geometries (%)* | *Max. $|S_{horizontal}|$* | *Availability for all-in-view geometries (%)* | *Availability for N-1 geometries (%)* |
| 3 | 1 | N/A[a] | 98.26 | 85.51 | N/A | 98.26 | 85.51 |
| | 2 | N/A | 97.92 | 84.17 | N/A | 97.92 | 84.17 |
| | 3 | N/A | 96.53 | 81.93 | N/A | 96.53 | 81.93 |
| | 4 | 2.95 | 96.53 | 78.47 | 1.20 | 96.53 | 79.81 |
| | 5 | 2.60 | 83.33 | 56.90 | 1.01 | 94.44 | 75.91 |
| | 6 | 2.34 | 55.56 | 29.87 | 0.89 | 92.71 | 68.42 |
| 4 | 1 | N/A | 100 | 97.68 | N/A | 100 | 97.68 |
| | 2 | N/A | 100 | 97.44 | N/A | 100 | 97.44 |
| | 3 | N/A | 100 | 96.95 | N/A | 100 | 96.95 |
| | 4 | 3.99 | 100 | 96.17 | 1.60 | 100 | 96.30 |
| | 5 | 3.38 | 97.57 | 86.32 | 1.35 | 100 | 94.59 |
| | 6 | 3.01 | 94.10 | 73.18 | 1.18 | 99.65 | 91.25 |
| 5 | 1 | N/A | 100 | 99.55 | N/A | 100 | 99.55 |
| | 2 | N/A | 100 | 99.51 | N/A | 100 | 99.51 |
| | 3 | N/A | 100 | 99.43 | N/A | 100 | 99.43 |
| | 4 | N/A | 100 | 99.23 | 2.14 | 100 | 99.23 |
| | 5 | 4.11 | 100 | 96.01 | 1.69 | 100 | 99.06 |

| MAE (m) | GGF-to-User Separation (km) | Rule 1: Screening HAL | | | Rule 2: Maximum $\|S_{horizontal}\|$ | | |
| | | *Screening HAL (m)* | *Availability for all-in-view geometries (%)* | *Availability for N-1 geometries (%)* | *Max. $\|S_{horizontal}\|$* | *Availability for all-in-view geometries (%)* | *Availability for N-1 geometries (%)* |
|---|---|---|---|---|---|---|---|
| | 6 | 3.72 | 99.31 | 89.62 | 1.47 | 100 | 98.37 |
| 7.5 | 1 | N/A | 100 | 99.84 | N/A | 100 | 99.84 |
| | 2 | N/A | 100 | 99.84 | N/A | 100 | 99.84 |
| | 3 | N/A | 100 | 99.84 | N/A | 100 | 99.84 |
| | 4 | N/A | 100 | 99.80 | N/A | 100 | 99.80 |
| | 5 | 6.73 | 100 | 99.72 | 2.53 | 100 | 99.76 |
| | 6 | 5.69 | 100 | 99.47 | 2.21 | 100 | 99.72 |
| 10 | 1 | N/A | 100 | 99.96 | N/A | 100 | 99.96 |
| | 2 | N/A | 100 | 99.96 | N/A | 100 | 99.96 |
| | 3 | N/A | 100 | 99.96 | N/A | 100 | 99.96 |
| | 4 | N/A | 100 | 99.92 | N/A | 100 | 99.92 |
| | 5 | 8.96 | 100 | 99.88 | 3.38 | 100 | 99.92 |
| | 6 | 7.71 | 100 | 99.76 | 2.95 | 100 | 99.92 |
| 15 | 1 | N/A | 100 | 100 | N/A | 100 | 100 |
| | 2 | N/A | 100 | 100 | N/A | 100 | 100 |
| | 3 | N/A | 100 | 100 | N/A | 100 | 100 |
| | 4 | N/A | 100 | 100 | N/A | 100 | 100 |
| | 5 | 13.64 | 100 | 100 | 5.14 | 100 | 100 |
| | 6 | 12.14 | 100 | 100 | 4.43 | 100 | 100 |
| 20 | 1 | N/A | 100 | 100 | N/A | 100 | 100 |
| | 2 | N/A | 100 | 100 | N/A | 100 | 100 |
| | 3 | N/A | 100 | 100 | N/A | 100 | 100 |
| | 4 | N/A | 100 | 100 | N/A | 100 | 100 |

| MAE (m) | GGF-to-User Separation (km) | Rule 1: Screening HAL | | | Rule 2: Maximum $|S_{horizontal}|$ | | |
|---|---|---|---|---|---|---|---|
| | | *Screening HAL (m)* | *Availability for all-in-view geometries (%)* | *Availability for N-1 geometries (%)* | *Max. $|S_{horizontal}|$* | *Availability for all-in-view geometries (%)* | *Availability for N-1 geometries (%)* |
| | 5 | 18.78 | 100 | 100 | 6.78 | 100 | 100 |
| | 6 | 16.79 | 100 | 100 | 5.89 | 100 | 100 |

a. "N/A" means no additional geometry restriction.

Table C.3. Sensitivity of availability to aircraft $\sigma_{pr\_air}$ inflation: inflated $\sigma_{vig}$

| MAE (m) | GGF-to-User Separation (km) | Availability (%) | | | | | | | |
|---|---|---|---|---|---|---|---|---|---|
| | | 1.5 $\sigma_{pr\_air}$ | | 2 $\sigma_{pr\_air}$ | | 3 $\sigma_{pr\_air}$ | | 4 $\sigma_{pr\_air}$ | |
| | | All-in-view geom.[b] | N-1 geom. | All-in-view geom. | N-1 geom. | All-in-view geom. | N-1 geom. | All-in-view geom. | N-1 geom. |
| 4 | 1 | 97.22 | 82.34 | 84.33 | [a] | | | | |
| | 2 | 97.22 | 81.93 | 80.56 | | | | | |
| | 3 | 96.53 | 80.55 | 77.08 | | | | | |
| | 4 | 96.18 | 79.20 | 73.26 | | | | | |
| | 5 | 95.83 | 77.57 | 69.10 | | | | | |
| | 6 | 94.44 | 75.86 | 64.58 | | | | | |
| 5 | 1 | 100 | 95.73 | 96.18 | 79.65 | | | | |
| | 2 | 100 | 95.60 | 95.49 | 79.08 | | | | |
| | 3 | 100 | 95.08 | 95.14 | 78.35 | | | | |
| | 4 | 100 | 94.30 | 95.14 | 77.33 | | | | |
| | 5 | 100 | 93.28 | 95.14 | 76.56 | | | | |
| | 6 | 100 | 91.82 | 94.44 | 75.42 | | | | |
| 7.5 | 1 | 100 | 99.59 | 100 | 98.37 | 96.88 | 81.64 | 72.57 | |
| | 2 | 100 | 99.59 | 100 | 98.33 | 96.88 | 81.60 | 72.22 | |
| | 3 | 100 | 99.59 | 100 | 98.33 | 96.88 | 81.36 | 71.88 | |
| | 4 | 100 | 99.59 | 100 | 98.13 | 96.53 | 81.03 | 70.83 | |
| | 5 | 100 | 99.55 | 100 | 98.09 | 96.53 | 80.71 | 69.79 | |
| | 6 | 100 | 99.55 | 100 | 97.76 | 96.18 | 80.10 | 67.71 | |
| 10 | 1 | 100 | 99.84 | 100 | 99.59 | 100 | 96.99 | 97.57 | 82.38 |
| | 2 | 100 | 99.84 | 100 | 99.59 | 100 | 96.91 | 97.22 | 82.25 |
| | 3 | 100 | 99.84 | 100 | 99.59 | 100 | 96.78 | 97.22 | 82.09 |
| | 4 | 100 | 99.80 | 100 | 99.59 | 100 | 96.74 | 97.22 | 81.85 |
| | 5 | 100 | 99.80 | 100 | 99.59 | 100 | 96.66 | 97.22 | 81.77 |
| | 6 | 100 | 99.76 | 100 | 99.59 | 100 | 96.58 | 96.88 | 81.60 |
| 15 | 1 | 100 | 99.96 | 100 | 99.88 | 100 | 99.63 | 100 | 98.70 |
| | 2 | 100 | 99.96 | 100 | 99.88 | 100 | 99.63 | 100 | 98.70 |
| | 3 | 100 | 99.96 | 100 | 99.88 | 100 | 99.63 | 100 | 98.70 |
| | 4 | 100 | 99.96 | 100 | 99.88 | 100 | 99.63 | 100 | 98.62 |
| | 5 | 100 | 99.96 | 100 | 99.88 | 100 | 99.59 | 100 | 98.58 |
| | 6 | 100 | 99.96 | 100 | 99.88 | 100 | 99.59 | 100 | 98.58 |
| 20 | 1 ~ 6 | 100 | 100 | 100 | 99.96 | 100 | 99.84 | 100 | 99.64 |
| 25 | 1 ~ 6 | 100 | 100 | 100 | 100 | 100 | 99.88 | 100 | 99.84 |
| 30 | 1 ~ 6 | 100 | 100 | 100 | 100 | 100 | 99.96 | 100 | 99.88 |

a. Availability for the empty cell is less than 50 %.; b. Geometries

# BIBLIOGRAPHY

[AP, 2013] AP, "London's Heathrow Airport cancels 260 flights, blames snow and low visibility," January 20, 2013, Retrieved from *Fox News*: www.foxnews.com/world/2013/01/20/london-heathrow-airport-cancels-260-flights-blames-snow-and-low-visibility/.

[Asam, 2010] M. Asam, "Detektion und Analyse von Mehrwegeausbreitung bei GNSS-Signalen," Semesterarbeit, Technische Universität München, Lehrstuhl für Flugsystemdynamik, November 2010 (in German).

[BBC, 2013] BBC, "Heathrow Airport: Snow stops one in 10 flights," January 21, 2013, Retrieved from *BBC News*: www.bbc.co.uk/news/uk-england-london-21116116.

[Boeing, 2009] Boeing, "Ground-Based Augmentation System and GBAS Landing System", US-India Aviation Cooperation Program, 2009, Retrieved from website: us-indiaacp.com/downloads/seminars/gbas/GBAS-Boeing.pdf.

[Brenner, 1998] M. Brenner, R. Reuter, and B. Schipper, "GPS Landing System Multipath Evaluation Techniques and Results," *ION GPS-98*, September 1998.

[Chen, 2010] A. Chen, A. Chabory, A. Escher, C. Macabiau. "Hybrid Deterministic-Satatistical GPS Multipath Simulator for Airport Navigation," CECom 2010, 20th

International Conference on Applied Electromagnetics and Communications, September 2010.

[DID, 2005] "The GPS constellation: Now and future," *Defense Industry Daily*, August 24, 2005.

[Datta-Barua, 2002] S. Datta-Barua, T. Walter, S. Pullen, M. Luo, J. Blanch, and P. Enge, "Using WAAS Ionospheric Data to Estimate LAAS Short Baseline Gradients," *Proceedings of ION National Technical Meeting 2002*, Anaheim, CA, January 28–30, 2002.

[Griffiths, 2013] S. Griffiths, "Heathrow reduces flights by 10% amid criticism," January 21, 2013, Retrieved from *TTG Digital*: www.ttgdigital.com/news/heathrow-reduces-flights-by-10-amid-criticism/4686416.article.

[Ene, 2005] A. Ene, D. Qiu, M. Luo, S. Pullen, and P. Enge, "A Comprehensive Ionosphere Storm Data Analysis Method to Support LAAS Threat Model Development," *Proceedings of ION National Technical Meeting 2005*, San Diego, CA, January 15-20, 2005, pp. 110-130.

[Enge, 1999] P. Enge, "Local Area Augmentation of GPS for the Precision Approach of Aircraft," *IEEE*, Vol. 87, No. 8, January 1999.

[EU-US, 2010] EU-US Cooperation on Satellite Navigation (Working Group C), "Combined Performances for Open GPS/Galileo Receivers," Final Version, July 19, 2010.

[FAA, 2002] *Specification: Category I Local Area Augmentation System Ground Facility*, Washington, D.C., Federal Aviation Administration, FAA-E-2937A, April 17, 2002.

[FAA, 2015] Federal Aviation Administration (FAA) *Navigation Programs - Ground Based Augmentation System (GBAS)*, Retrieved from www.faa.gov/about/office_org/headquarters_offices/ato/service_units/techops/navservices/gnss/laas/.

[FlyGLS, 2016] *GBAS Approach & Landing Systems: The Future of Precision Approach*, Retrieved from www.flygls.net.

[Gao, 2008] Gao, G. X., "Toward Navigation Based on 120 Satellites: Analyzing The New Signals," *Ph.D. Dissertation*, Electrical Engineering, Stanford University, 2008.

[Hegarty, 2009] C. Hegarty, "Derivation of the Discrimination Function with and without Multipath for the Non-Coherent Dot-Product Discriminator," MITRE White Paper, November 20, 2009.

[ICAO, 2006] *Standards and Recommended Practices: Annex 10 – Aeronautical Telecommunications*. Vol. I (Radio Navigation Aids). Montreal Canada, International Civil Aviation Organization (ICAO), 6th Edition, July 2006.

[Jahn, 1996] A. Jahn, H. Bischl, G. Heib, "Channel Characterization for Spread Spectrum Satellite Communication," *IEEE 4th International Symposium on Spectrum Techniques and Applications Proceedings*, Volume 3, September 22-25, 1996, pp. 1221-1226.

[Klobuchar, 1995] J. Klobuchar, P. Doherty, and M. Bakry El-Arini, "Potential Ionospheric Limitations to GPS Wide-Area Augmentation system (WAAS)," *Navigation*, 42(2), 353-370, 1995.

[Klobuchar, 1996] J. Klobuchar, "Ionospheric Effects on GPS," *Global Positioning System: Theory and Applications*, Vol. I, Edited by B. Parkinson and J. Spilker, AIAA Publication, 1996.

[Konno, 2007] H. Konno, "Design of an Aircraft Landing System Using Dual-Frequency GNSS," *Ph.D. Dissertation*, Aeronautics and Astronautics, Stanford University, 2007.

[Lee, Apr 2006] J. Lee, S. Pullen, *et al.*, "Assessment of Nominal Ionosphere Spatial Decorrelation for LAAS," *Proceedings of the IEEE/ION Position Location and Navigation Symposium 2006*, San Diego, CA, April, 2006.

[Lee, 2006] J. Lee, M. Luo, S. Pullen, Y.S. Park, M. Brenner, and P. Enge, "Position-Domain Geometry Screening to Maximize LAAS Availability in the Presence of Ionosphere Anomalies," *Proceedings of ION GNSS 2006*, Fort Worth, TX, September 26-29, 2006, pp. 393-408.

[Lee, 2007] J. Lee, S. Pullen, S. Datta-Barua, and P. Enge, "Assessment of Ionosphere Spatial Decorrelation for Global Positioning System-Based Aircraft Landing Systems," *AIAA Aircraft J.*, 44(5), 1662-1660, 2007.

[Luo, 2003] M. Luo, S. Pullen, J. Dennis, H. Konno, G. Xie, T. Walter, S. Datta-Barua, T. Dehel, and Per Enge "LAAS Ionosphere Spatial Gradient Threat Model and Impact of LGF and Airborne Monitoring," *Proceedings of ION GPS 2003*, Portland, OR., September 9-12, 2003, pp 2255-2274.

[Luo, Jan 2004] M. Luo, S. Pullen, T. Walter, and P. Enge, "Ionosphere Spatial Gradient Threat for LAAS: Mitigation and Tolerable Threat Space", *Proceedings of ION 2004 Annual Meeting*, San Diego, CA, January 26-28, 2004.

[Luo, Sep 2004] M. Luo, s. Pullen, A. Ene, D. Qiu, T. Walter, and P. Enge, "Ionosphere Threat to LAAS: Updated Model, User Impact, and Mitigations," *Proceedings of ION GNSS 2004*, Long Beach, CA., September 21-24, 2004, pp. 2771-2785.

[Luo, 2005] M. Luo, S. Pullen, s. Datta-Barua, G. Zhang, T. Walter, and and P. Enge, "LAAS Study of Slow-Moving Ionosphere Anomalies and Their Potential

Impacts," *Proceedings of ION GNSS 2005*, Long Beach, CA, September 13-16, 2005, pp. 2337-2349.

[McGraw, 2000] G. McGraw, T. Murphy, M. Brenner, and S. Pullen, "Development of the LAAS Accuracy Models," *Proceedings of ION GPS 2000*, Salt Lake City, UT, September 19-22, 2000.

[Misra, 2006] P. Misra, and P, Enge, "Global Positioning System: Signals, Measurements, and Performance," 2nd Edition, Ganga-Jamuna, 2006.

[Mitelman, 2004] A. Mitelman, "Signal Quality Monitoring for GPS Augmentation Systems," *Ph.D. Dissertation*, Electrical Engineering, Stanford University, 2004.

[Montloin, 2012] L. Montloin, L. Azoulai, A. Chen, A. Martineau, C. Milner, *et al.*, "GNSS multipath error model for airport surface operations," ION GNSS 2012, 25th International Technical Meeting of The Satellite Division of the Institute of Navigation, Sep 2012, Nashville, United States. pp 210-228, 2012.

[Murphy, 2005] T. Murphy and M. Harris, "More Results from the Investigation of Airborne Multipath Errors," *Proceedings of ION GNSS 2005*, Long Beach, CA, September 13-16, 2005.

[Murphy, 2010] T. Murphy, M. Harris, and Y.S. Park, S. Pullen, "GBAS Differentially corrected Positioning Service Ionospheric Anomaly Errors Evaluated in an Operational Context," *Proceedings of ION ITM 2010*, San Diego, CA, January 25-27, 2010.

[Park, 2007] Y. S. Park, G. Zhang, S. Pullen, J. Lee, and P. Enge, "Data-Replay Analysis of LAAS Safety during Ionosphere Storms," *Proceedings of ION GNSS 2007*, Fort Worth, TX, September 25-28, 2007.

[Pervan, 1996] B. Pervan, "Navigation Integrity for Aircraft Precision Landing Using the Global Positioning System," *Ph.D. Dissertation*, Aeronautics and Astronautics, Stanford University, 1996.

[Pervan, 2005] B. Pervan and L. Gratton, "Orbit Ephemeris Monitors for Local Area Differential GPS," *IEEE Transactions on Aerospace and Electronic Systems*, Vol. 41, No. 2, April, 2005.

[Phelts, 2000] E. Phelts, D. Akos, and P. Enge, "Robust Signal Quality Monitoring and Detection of Evil Waveforms," *Proceedings of ION GPS 2000*, Salt Lake City, UT, September 19-22, 2000.

[Pullen, 2001] S. Pullen, J. Lee, *et al.*, "Ephemeris Protection Level Equations and Monitor Algorithms for GBAS," *Proceedings of ION GPS 2001*, Salt Lake City, UT, September 11-14, 2001.

[Pullen, Sep 2002] S. Pullen, M. Luo, *et al.*, "LAAS Ground Facility Design Improvements to Meet Proposed Requirements for Category II/III Operations," *Proceedings of ION GPS Meeting 2002*, Portland, OR, September 24-27, 2002.

[Pullen, 2002] S. Pullen, T. Walter, and P. Enge, "System Overview, Recent Developments, and Future Outlook for WAAS and LAAS," presented at *Tokyo University of Mercantile Marine GPS Symposium*, Tokyo, Japan, November 11-13, 2002.

[Pullen, 2009] S. Pullen, Y.S. Park, and P. Enge, "Impact and Mitigation of Ionospheric Anomalies on Ground Based Augmentation of GNSS," Published in the AGU Electronic Journal, *Radio Science*, Vol. 44, RSOA21, 2009.

[Ramakrishnan, 2008] S. Ramakrishnan, J. Lee, S. Pullen, and P. Enge, "Targeted Ephemeris Decorrelation Parameter Inflation for Improved LAAS Availability

during Severe Ionosphere Anomalies", *Proceedings of ION 2008 National Technical Meeting*, San Diego, CA, January 28-30, 2008.

[Rife, 2004] J. Rife, T. Walter, J. Blanch, "Overbounding SBAS and GBAS Error Distributions with Excess-Mass Functions," presented at *The 2004 International Symposium of GNSS/GPS*, Sydney, 2004

[Rife, 2006] J. Rife and E. Phelts, "Formulation of a Time-Varying Maximum Allowable Error for Ground-Based Augmentation Systems," *Proceedings of ION National Technical Meeting 2006*, Monterey, CA, January 18-20, 2006.

[RTCA, 1998] *RTCA Report on the Role of the Global Navigation Satellite System (GNSS) in Supporting Airport Surface Operations*, RTCA Special Committee 159 – Prepared by Working Group 4B – Final Draft – DO247 – November 6, 1998.

[RTCA, 2003] *Minimum Aviation System Performance Standards: Required Navigation Performance for Area Navigation*, Washington, D.C., RTCA SC-181, DO-236B, October 28, 2003.

[RTCA, 2004] *Minimum Aviation System Performance Standards for the Local Area Augmentation System (LAAS)*, Washington, D.C., RTCA SC-159, WG-4, DO-245A, December 9, 2004.

[RTCA, 2008] *Minimum Operational Performance Standards for GPS Local Area Augmentation System Airborne Equipment*, Washington, D.C., RTCA SC-159, WG-4, DO-253C, December 16, 2008.

[Shively, 1999] C. Shively, "Derivation of Acceptable Error Lists for Satellite Signal Faults in LAAS," *Proceedings of ION-GPS 1999*, Nashville, TN, September, 1999.

[Shively, 2008] C. Shively, "Safety Concepts for Mitigation of Ionospheric Anomaly Errors in GBAS," *Proceedings of ION NTM 2008*, San Diego, CA, January 28-30, 2008.

[Simili, 2006] D.V. Simili, B. Pervan, "Code-Carrier Divergence Monitoring for the GPS Local Area Augmentation System, *Proceedings of IEEE/ION PLANS 2006*, San Diego, CA, April 25-27, 2006.

[Spilker, 1996a] J. Spilker, "GPS Signal Structure and Theoretical Performance," *Global Positioning System: Theory and Applications*, Vol. I, edited by B. Parkinson and J. Spilker, AIAA Publication, 1996.

[Spilker, 1996b] J. Spilker, "GPS Navigation Data," *Global Positioning System: Theory and Applications*, Vol. I, Edited by B. Parkinson and J. Spilker, AIAA Publication, 1996.

[USmap] U.S map, Retrieved from www.allusairports.com.

[Walter, 1995] T. Walter and P. Enge, "Weighted RAIM for Precision Approach," *Proceedings of ION GPS-95*, Palm Springs, CA, September 12-15, 1995.

[Walter, 2000] T. Walter, et al., "Robust detection of ionospheric irregularities, *Proceedings of ION GPS 2000*, Salt Lake City, Utah, September1-22, 2000.

[Wikipedia, 2016] Wikipedia, "Instrument Approach," August 20, 2016, Retrieved from *Wikipedia*: https://en.wikipedia.org/wiki/ Instrument_approach.

[Xie, 2001] G. Xie, S. Pullen, et al., "Integrity Design and Updated Test Results for the Stanford LAAS Integrity Monitor Testbed," *Proceedings of ION National Technical Meeting 2001*, Albuquerque, NM, June 11-13, 2001.

[Zaugg, 2002] T. Zaugg, "A New Evaluation of Maximum Allowable Errors and Missed Detection Probabilities for LAAS Ranging Source Monitors," *Proceedings of The ION 58$^{th}$ Annual Meeting*, Albuquerque, NM, June 24-26, 2002.